

REFERENCE ONLY

# Evolution and Dynamics of Plasma Generated from Solid Targets by Strong Laser Fields

Ph. D thesis  
**RIJU C ISSAC**

International School of Photonics  
Cochin University of Science & Technology  
Cochin 682 022, INDIA  
September 1998


International School of Photonics  
Cochin University of Science & Technology  
Cochin 682 022, INDIA

Dr. C P Girjavallabhan  
Professor & Director



Phone: +91-484-532848  
Fax : +91-484-543295  
Email : photonix@md2.vsnl.net.in  
Date : September 28, 1998

Certified that the thesis entitled ***Evolution and dynamics of plasma generated from solid targets by strong laser fields*** is the report of the original work carried out by Mr. Riju C Issac at the Laser laboratory of the International School of Photonics, Cochin University of Science & Technology, Cochin 682 022 under my guidance and supervision.

  
Prof. C P Girjavallabhan  
(Supervising Guide)

## PREFACE

The interaction of light with matter is a subject of considerable theoretical as well as practical importance. The availability of extremely high power laser beams has opened up new and exciting possibilities in the field of research. In addition to inducing several nonlinear optical effects, such laser beams can generate plasma from solid targets and in certain specific cases, they can even trigger nuclear reactions. Thus laser induced phenomena have acquired a great deal of attention from scientists working in a variety of areas like optics, materials science, plasma physics and nuclear fusion. The present thesis deals with an experimental study of plasma generated by strong laser pulses from a number of solid targets. This work summarizes the results of the measurements carried out by the author during the past four years in the laser laboratory of the International School of Photonics and it also highlights a number of novel findings which have resulted from the above measurements.

Interaction of light with matter is a fairly complex phenomenon and different processes dominate at different power levels. The mechanisms of light absorption by the materials vary widely depending on their optical, structural and thermal properties. High power laser beam interaction with solid targets induces transient heating and it lead to generation of plasma in the vicinity of the absorbing surface. The temperature of the lattice instantaneously rises well above the melting point and the material rapidly evaporates from the condensed phase. This phenomenon is known as laser ablation which has several practical applications. Since the interaction of the laser beam with the target as well as with the plasma are highly nonlinear, pulsed laser ablation invokes considerable interest for basic research related to the interaction mechanisms and plasma dynamics. In addition to the basic interests, pulsed laser ablation is primarily employed for the deposition of several materials in thin film form on suitable substrates. Pulsed laser deposition is far superior to the conventional deposition techniques such as vacuum evaporation and sputtering since pulsed laser deposition can be done even in reactive gas environments which is an essential condition for the deposition of high quality oxide films. The quality of the deposited films can be controlled by adjusting the pulse repetition rate, laser energy, ambient pressure, laser wavelength etc. A number of species are present within the ablated plume such as atoms, ions, molecules, clusters and free electrons. A detailed study of the components of such plasma itself is a subject of considerable interest. During the course of the thesis work, we have made a number of attempts to characterize the plasma in terms of the

various phenomena taking place within the plume. The results are organized in eight chapters, the contents of which are briefly outlined below.

**Chapter I** gives a brief introduction to laser produced plasmas. The relevant aspects of laser interaction with solids and the various phenomena taking place inside the plasma are briefly reviewed in order to have an outlook into the recent advancements in the subject.

The authenticity of experimental research very much rely on the methods of experimentation and the accuracy and sensitivity of the measuring devices. **Chapter II** gives the description of the various experiments that have been conducted in connection with the studies presented in this thesis. A multipurpose plasma chamber has been designed and fabricated as a part of the present studies. The fundamental output of a Q-switched Nd:YAG laser is focussed on to the target kept inside a plasma chamber maintained at appropriate ambient pressure to produce plasma. The plasma formed in the vicinity of the target is highly transient which rapidly expands to the surroundings creating a large density gradient in front of the target. The luminous plasma thus formed is studied using spectroscopic techniques, Langmuir probes and by using Michelson interferometry. The chapter also describes the specifications and measuring capabilities of various instruments used for the experiments.

Metals are a class of materials with well known electrical, optical and thermal properties. There are a large number of free electrons at the metal surface and the interaction of the laser primarily occurs with the free electron cloud. The absorbed energy is quickly transferred to the lattice within a few picoseconds which results in the formation of the plasma in the vicinity of the focal region and its rapid expansion. The dynamics of the expanding atoms and ions were studied either by employing spectroscopic techniques or with Langmuir probes. A collection of slower atomic species emerge at reduced pressure below  $4 \times 10^{-3}$  mbar and these species have a greater velocity spread. The space resolved measurements on ions show that there exists a sharp boundary at a definite distance from the target where the temporal profile splits in to fast and slower components. **Chapter III** is devoted to the study of the dynamics of the atomic and ionic species in the laser produced plasma from metallic silver targets.

The temporal profiles also reflect the various interaction mechanisms and temperature at the focal spot as well as in the plasma. Temporal profiles of various constituents (eg. electrons, ions, neutrals, ambient gas molecules etc.) are totally different from each other. For example, the temporal profile of the electrons show a peculiar twin

peak distribution. The peak which appears very early in time is narrow with full width at half maximum almost the same as that of the laser pulse itself. This initial prompt electron pulse is energetic enough to collisionally excite and ionize the ambient atoms and molecules present inside the plasma chamber. The second peak is broader and extends over to several microseconds. Those electrons with broad TOF distribution come along with the laser plasma. Hence the prompt electrons corresponding to the first peak in the electron temporal profile can be utilized for the collisional excitation and ionization of various molecules and atoms. These findings have been included in **Chapter IV** where the temporal profiles of various species inside the plasma were analyzed at different distances away from the target surface.

Pulsed laser deposition has been widely used for the preparation of good quality thin films of materials. The most essential requirement of thin film deposition is its spatial uniformity. Thus the precise knowledge about the angular distribution of the ablative products is required for the optimization of thin film deposition conditions. Also, the quality of thin films depends critically on the distance from the target and the focal spot dimensions. **Chapter V** gives the description of angular distribution of ablative products.

Apart from silver target, plasma from another very important multicomponent material *viz.* high temperature superconducting  $\text{YBa}_2\text{Cu}_3\text{O}_7$  has also been studied in air at atmospheric pressure. Even though there are recent reports that stoichiometric thin films of  $\text{YBa}_2\text{Cu}_3\text{O}_7$  were prepared at atmospheric pressure, our major aim was to study the basic mechanisms of plasma formation and its evolution. In order to attain this goal, we have carried out spectroscopic measurements at the core of the laser generated plasma from  $\text{YBa}_2\text{Cu}_3\text{O}_7$ . Ions inside the plasma can be produced either by direct multiphoton absorption of the laser light by the atomic and molecular species or through collisions among the constituents. It has been found that the laser generated plasma from  $\text{YBa}_2\text{Cu}_3\text{O}_7$  collectively diffuses away from the target surface at very high laser intensities. This collective drift is similar to the ambipolar diffusion in other types of laboratory plasmas. We propose here that this sudden drift apparently occurs as a result of the formation of a charged double layer at the plasma boundary. **Chapter VI** essentially illustrates details of various ionization mechanisms and the formation of charged double layers at the plasma boundary.

It is found that during initial phase of the plasma with small time delays, the emission spectrum is dominated by plasma blackbody continuum radiation and as time elapses, the emission lines of atoms and ions develop in the spectrum. The important

aspect worth mentioning is that the blackbody continuum at smaller time delays is almost identical for different target materials. Line averaged electron densities were deduced from interferometric measurements at various laser intensities. **Chapter VII** deals with the time resolved spectral measurements in a laser produced  $\text{YBa}_2\text{Cu}_3\text{O}_7$  plasma. The laser intensity dependent emission line profiles of the resonance transition from the singly ionized barium at 455.4 nm have also been investigated. It has been found that the line has a profile which is strongly self-reversed and at very high laser intensities, a new peak is developed at the center of the self-reversed resonance line which is explained as due the anisotropic resonance scattering of the radiation.

**Chapter VIII** summarizes the results described in the thesis and their implications on the dynamics of laser produced plasma.

**Some of the important results obtained were published in the following articles:**

**(a) In Journals**

1. *Anomalous profile of self-reversed resonance line from  $\text{Ba}^+$  in a laser produced plasma from  $\text{YBa}_2\text{Cu}_3\text{O}_7$* , Riju C Issac, S S Harilal, C V Bindhu, Geetha K Varier, V P N Nampoori and C P G Vallabhan, *Spectrochimica Acta B* **52** (1997) 1791
2. *Investigations on nanosecond laser produced plasma in air from the multicomponent material  $\text{YBa}_2\text{Cu}_3\text{O}_7$* , Geetha K Varier, Riju C Issac, S S Harilal, C V Bindhu, V P N Nampoori and C P G Vallabhan, *Spectrochimica Acta B* **52** (1997) 657
3. *Dynamics of laser produced silver plasma under film deposition conditions studied by optical emission spectroscopy*, Riju C Issac, K Vasudevan Pillai, S S Harilal, Geetha K Varier, C V Bindhu, Pramod Gopinath, P Radhakrishnan, V P N Nampoori and C P G Vallabhan, *Appl. Surf. Sci.* **125** (1998) 227
4. *Twin peak distribution of electron emission profile and impact ionization of ambient molecules during laser ablation of silver target*, Riju C Issac, Pramod Gopinath, Geetha K Varier, V P N Nampoori and CPG Vallabhan, *Appl. Phys. Lett.* **73** (1998) 163
5. *Collective diffusion of laser produced plasma from the multicomponent  $\text{YBa}_2\text{Cu}_3\text{O}_7$  target in air*, Riju C Issac, Geetha K Varier, S S Harilal, V P N Nampoori and C P G Vallabhan *Appl. Phys. B*, in press, (1998)

6. *Prompt electron emission and collisional ionization of ambient gas during laser ablation of silver target*, Riju C Issac, Geetha K Varier, Pramod Gopinath, S S Harilal, V P N Nampoore and C P G Vallabhan, *Appl. Phys. A*, in press, (1998)
7. *Ionic temporal profiles from a laser produced silver plasma at the plasma ambient boundary in low pressure nitrogen gas*, Riju C Issac, Geetha K Varier, Pramod Gopinath, V P N Nampoore and C P G Vallabhan, *J. Appl. Phys.* (communicated)

**(b) Papers published in conference proceedings**

- 1 *Laser induced plasma from graphite : Time dependence of vibrational temperature*  
S S Harilal, Riju C Issac, C V Bindhu, G K Varier, V P N Nampoore & C P G Vallabhan *Proc. of National Laser Sym.* (IRDE Dehradun) p.265 (1995)
- 2 *Temporal and spatial evolution of laser ablated carbon clusters from graphite plasma*, S S Harilal, Riju C Issac, C V Bindhu, Geetha K Varier, V P N Nampoore & C P G Vallabhan *Proc. International Conf. on Spectroscopy : Perspectives & Frontiers (INCONS)* (BARC Bombay) p.146 (1996)
- 3 *Electron density determination of laser induced plasma from PMMA using phase shift spectroscopy*, Geetha K Varier, S S Harilal, C V Bindhu, Riju C Issac, V P N Nampoore & C P G Vallabhan *Proc. of National Laser Sym.* (BARC Bombay) 10 (1996)
- 4 *Time resolved studies of C<sub>2</sub> emission spectrum in the laser induced plasma from graphite* Riju C Issac, S S Harilal, C V Bindhu, Geetha K Varier, V P N Nampoore & C P G Vallabhan *Proc. of National Laser Sym.* (BARC Bombay) H13 (1996)
- 5 *Diffusion characteristics of laser produced plasma from a solid target in air at atmospheric pressure*, Riju C Issac, S S Harilal, Geetha K Varier, C V Bindhu, V P N Nampoore & C P G Vallabhan, *Proc. APSYM -96*, Dept. of Electronics, CUSAT p.163
- 6 *Diagnostics of laser produced plasma from silver under film deposition conditions*  
Riju C Issac, S S Harilal, Geetha K Varier, C V Bindhu, V P N Nampoore & C P G Vallabhan, *Proc. National Laser Symposium*, CAT Indore (1997) p. 272
- 7 *Self reversal and anomalous line profile of the 4554 Å Ba resonance line in the laser produced plasma of YBa<sub>2</sub>Cu<sub>3</sub>O<sub>7</sub> in air*, S S Harilal, Riju C Issac, C V Bindhu, G K Varier, V P N Nampoore & C P G Vallabhan, *Proc. National Laser Symposium*, CAT Indore (1997) p.283

- 8 *Molecular excitations by prompt electron impact during laser beam interactions with silver target*, **Riju C Issac**, Pramod Gopinath, S S Harilal, Geetha K Varier, Binoy Paul, V P N Nampoore and C P G Vallabhan, *Proceedings of the National Laser Symposium*, Physical Research Laboratory, Ahmedabad during December 10-12, 1997.
- 9 *Analysis of ionic emission profiles during laser beam interaction with silver studied using Langmuir probe* **Riju C Issac**, P Radhakrishnan, V P N Nampoore and C P G Vallabhan *Proceedings of the National Laser Symposium*, Physical Research Laboratory, Ahmedabad during December 10-12, 1997.
- 10 *Temporal variations of electron density and temperature in a laser produced plasma from silicon carbide*, Pramod Gopinath, **Riju C Issac**, Geetha K Varier, C V Bindhu, S S Harilal, V P N Nampoore and C P G Vallabhan *Proceedings of the National Laser Symposium*, Physical Research Laboratory, Ahmedabad during December 10-12, 1997.
- 11 *Prompt electron emission and impact ionization of ambient gas molecules during laser metal interaction*, **Riju C Issac**, Pramod Gopinath, S S Harilal, Geetha K Varier, C V Bindhu, V P N Nampoore and C P G Vallabhan *Proceedings of the PLASMA-'97*, Institute for Plasma Research, Gandhinagar, Gujarat, during December 2-5, 1997



# CONTENTS

## Chapter One

### Laser produced plasmas

#### Abstract

1.1 Laser absorption in solids .....	3
1.1.1 Interactions in femtosecond time scales.....	5
1.1.2 Interactions in picosecond time scales .....	7
1.1.3 Interactions in nanosecond time scales .....	8
1.2 Mechanisms of laser ablation.....	8
1.2.1 Phase explosion.....	9
1.2.2 Normal vaporization.....	11
1.2.3 Normal boiling .....	12
1.2.4 Sub-surface heating model.....	12
1.3 Effect of collisions on time of flight profiles.....	12
1.4 Some useful ablation parameters.....	16
1.5 Plasma shielding of laser light .....	17
1.6 Charged double layers in laser plasmas.....	20
1.7 Effect of ambient gas.....	24
1.8 Spectroscopic diagnostics of laser plasmas .....	26
1.8.1 Stark broadening of spectral lines.....	26
1.8.2 Determination of electron temperature using emission spectroscopy .....	29
1.8.2.1 Local thermodynamic equilibrium	
1.8.2.2 Corona equilibrium	
1.8.3 $T_e$ from relative line intensity measurements .....	32
1.9 Plasma diagnostics using Langmuir probes.....	34
1.10 Summary.....	37

#### References

## Chapter Two

### Fabrication and Methods

#### Abstract

2.1 Design and fabrication of the plasma chamber.....	46
2.2 Description of the experimental setup for time of flight studies.....	48
2.3 Electron density from Michelson interferometry.....	55
2.3.1 Evaluation of electron density .....	55
2.4 $T_e$ measurements using Langmuir probes.....	58

#### References

## **Chapter Three**

### **Space resolved atomic and ionic dynamics in laser produced silver plasma**

Abstract

3.1 Evolution of neutral silver atoms .....	64
3.2 Space-resolved intensity measurements and plume expansion.....	68
3.3 Temporal profiles and time-resolved spectra at the plasma core .....	72
3.4 Dynamics of positive ions.....	74
3.4.1 Spatial dependence of ion TOF profiles.....	75
3.4.2 Influence of pressure on ion profiles.....	78
3.5.3 Ion TOF profiles as a function of laser energy .....	81
3.5 Space-resolved electron temperature measured using Langmuir probes .....	84
3.7 Summary.....	85

References

## **Chapter Four**

### **Prompt electron emission and impact ionization during laser ablation of silver**

Abstract

4.1 Electron temporal profiles .....	91
4.2 Comparison of TOF profiles of different species.....	97
4.2.1 UV absorption from the plasma core .....	99
4.2.2 Direct multiphoton absorption and ionization.....	100
4.2.3 Collisional ionization due to prompt electrons.....	100
4.3 Time-resolved spectroscopy .....	101
4.3.1 Nitrogen as ambient gas .....	102
4.3.2 Argon as ambient gas.....	104
4.3.3 Carbon dioxide as ambient gas.....	107
4.3 Summary.....	109

References

## **Chapter Five**

### **Angular distribution of ablated species**

Abstract

5.1 Angular dependence of ablated species.....	112
5.2 Summary.....	120

References

## **Chapter Six**

### **Ionization and collective drift in laser-plasma from $\text{YBa}_2\text{Cu}_3\text{O}_7$**

Abstract

6.1 Electron density measurements using laser interferometry .....	124
6.2 Laser-plasma interaction and ionization.....	126
6.3 Radial drift in laser plasmas.....	130
6.4 Discussion on electron heating and formation of charged double layer.....	135
6.5 Summary.....	138

References

## **Chapter Seven**

### **Time-resolved study of spectral emissions and anomalous line profiles in laser generated plasma from $\text{YBa}_2\text{Cu}_3\text{O}_7$**

Abstract

7.1 Time resolved emission from $\text{YBa}_2\text{Cu}_3\text{O}_7$ plasma at atmospheric pressure.....	143
7.2 Self-reversal and anomalous profile of $\text{Ba}^+$ resonance line in $\text{YBa}_2\text{Cu}_3\text{O}_7$ plume. 146	
7.2.1 Discussions on self-reversal of $\text{Ba}^+$ emission.....	149
7.2.2 Discussion on profile of $\text{Ba}^+$ resonance line at high laser intensities.....	152
7.3 Summary.....	155

References

## **Chapter Eight**

### **Summary and Conclusions**

8.1 Laser generated plasma from silver targets .....	159
8.2 Laser produced plasma from $\text{YBa}_2\text{Cu}_3\text{O}_7$ .....	161
8.3 Future trends .....	162

# Laser produced plasmas

## **Abstract**

This introductory chapter gives a brief idea on laser produced plasma which is relevant in understanding the subsequent chapters. The processes that occur in laser produced plasmas are too numerous and a description of the whole range of phenomena is not attempted here due to space limitations. The chapter deals with the laser absorption by the bulk of the target, laser-plasma interactions, the effect of various parameters on the evolution of the plasma, plasma diagnostic techniques etc.

The invention of high power lasers has become a milestone in the study of light matter interactions and the related linear and non-linear phenomena. Just after the invention of high power laser systems by Maiman, the phenomenon of gas breakdown and dense plasma formation upon focusing of strong laser fields has been demonstrated.<sup>1</sup> Since then, there has been tremendous interest in the phenomenon of optical breakdown and plasma formation in solids, liquids and gases. Now it has come to a stage where the intensities are so high that even the dynamics of nuclear motions may be perturbed in the intense laser fields. The name *laser ablation* is used generically to describe such explosive laser matter interactions above the damage threshold intensities. The ablative interaction depends very much on the wavelength of irradiation, the optical power density and the properties of the material. Depending upon the duration of the laser pulse and intensity, the explosive mechanisms can be described as vaporization or ablation even though such a division is not ideal since the simultaneous occurrence of the two cannot be ruled out. In this thesis various aspects of explosive laser matter interactions and subsequent plasma formation from solids are discussed. This introductory chapter deals with different processes involved in the interaction of high power laser beams with solid targets and the dynamics of the evolution of the resulting plasma. A complete review of the subject is not attempted but a brief introduction to the subject relevant in the context of the thesis is given.

A target in condensed phase is heated due to the irradiation by the laser pulse and a high density plasma is formed in the near vicinity. The processes taking place are heating, melting, vaporization and expansion. A large number of theoretical as well as experimental descriptions regarding the various mechanisms that lead to the ablation of a surface due to laser irradiation are available in the literature.<sup>2-26</sup> The mechanisms of laser heating of the target and the resulting plasma depend critically on the laser power density. Even though one cannot strictly say that at certain laser intensity a particular process happens, the various processes are classified according to laser power density, the duration of the laser pulse and the material characteristics.

In pulsed laser ablation, the thermal effects play an important role as demonstrated by the pioneering works of Kelly and others.<sup>27-31</sup> At comparatively low laser intensities, the vaporization from the extreme outer surface and boiling from an extended near surface region take place whereas at high laser intensities, additional effects like *phase explosion*<sup>2,32-34</sup> and *sub surface heating model*.<sup>35</sup> A large number of model calculations are made for the study of laser-matter interaction processes.<sup>36-50</sup> All these studies include models of laser-solid interactions initiating the vapor plume, plume ionization and heating through laser absorption, hydrodynamic and collisional descriptions of the plume transport, dynamics of cluster formation, effect of ambient gas on plume evolution etc.

Apart from the study of laser matter interactions, pulsed laser ablation is primarily employed for the deposition of several materials in thin film form on suitable substrates.<sup>4,51</sup> It has been proved to be a convenient and accurate method for thin film deposition as better control over film characteristics can be obtained by varying the laser parameters and ambient conditions. Pulsed laser deposition (PLD) is far superior to the conventional deposition techniques<sup>1</sup> such as vacuum evaporation and sputtering since PLD can be done in reactive gas environments which is an essential criterion for the deposition of high quality oxide thin films, especially superconducting films. PLD of high-Z metallic multilayer superlattices are employed in

the development of X-ray mirrors.<sup>52</sup> Metal buffer layers are said to be useful for the deposition of high  $T_c$  superconducting thin films.<sup>53</sup> Because of the low resistivity and stability, thin metal films are widely used in optoelectronics and integrated circuits for forming ohmic contacts with semiconductors. However the full utilization of laser ablation in thin film deposition has not been possible due to various reasons. The successful deposition of stoichiometric thin films by the method of PLD demands the characterization of the ablation plume with temporal, spatial and angular variations.<sup>54-59</sup>

### **1.1 Laser absorption in solids**

The mechanisms of laser induced material removal can basically be classified in to two; *viz.* thermal and nonthermal. In a thermal process, as the name indicates the absorbed energy is rapidly converted into thermal energy which induces bond breaking. But in a nonthermal process, the laser photons selectively excite specific bonds in the materials thereby ejecting the atoms and molecules directly. In the case of materials which are normally transparent to the laser light at a given laser wavelength, the targets may be desorbed due to nonlinear absorption or laser generated absorbing defect sites. In metallic solids, the light is absorbed by the free electrons present in the target. Even in the case of insulators, there are free electrons in the conduction band at a finite temperature above absolute zero. These electrons may absorb the laser light and induce a cascade growth of the density of free electrons through collisions.

During the interaction of a laser with a solid targets, the laser energy is absorbed by free electrons due to inverse bremsstrahlung (A figurative representation of the process is shown in fig1.1). Then the evolution of the absorbed laser energy involves thermalisation within the electron subsystem, energy transfer to the lattice and the energy losses due to the electron heat transport into the target. The first of the three processes, *viz.* thermalisation of the electron subsystem, can be considered as very fast. Then the energy transport into the lattice can be described by the following coupled nonlinear equations<sup>60-62</sup>

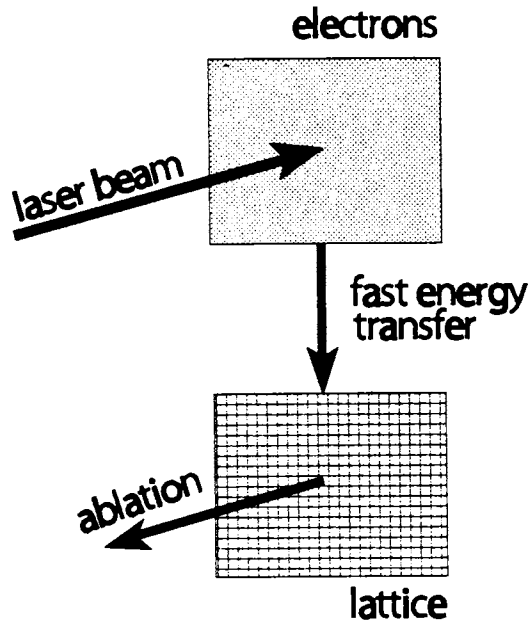


**Figure 1.1** Figure showing the mechanism of laser absorption by the conduction electrons and energy transfer to the lattice through electron-phonon interactions during high power laser interaction with solids.

$$C_e \frac{\partial T_e}{\partial t} = k_e \frac{\partial^2 T_e}{\partial z^2} - \gamma (T_e - T_i) + I(t) A \alpha \exp(-\alpha z) \quad (1.1)$$

and

$$C_i \frac{\partial T_i}{\partial t} = \gamma (T_e - T_i) \quad (1.2)$$

Here  $z$  is the distance perpendicular to the target surface,  $I(t)$  is the laser intensity,  $A = 1 - R$  and  $\alpha$  are the surface transmittivity and material absorption coefficient respectively,  $C_e$

and  $C_i$  are the heat capacities of the electron and lattice subsystems per unit volume,  $\gamma$  is the electron phonon coupling constant and  $k_e$  is the electron thermal conductivity.

In the above equations, the thermal conductivity of the lattice subsystem is neglected since the values are much less than that of the electrons. Hence electrons can be heated to very high transient temperatures. Eesley<sup>63</sup> have shown through numerical simulations a nonequilibrium electron heating during picosecond laser interaction with copper. In fact, three different time scales that are involved in the process<sup>60</sup> viz.  $\tau_e$ ,  $\tau_i$  and  $\tau_L$ . Here  $\tau_e = C_e/\gamma$  is the electron cooling time,  $\tau_i = C_i/\gamma$  is the lattice heating time ( $\tau_e \ll \tau_i$ ) and  $\tau_L$  is the duration of the laser pulse. Depending upon these time scales and the width of the laser pulse, the interaction of laser pulses with metals is again divided into three regimes called femtosecond, picosecond and nanosecond interactions in accordance with the discussions given in Ref. 60.

### 1.1.1 Interactions in femtosecond time scales

The characteristic electron energy relaxation time is of the order of 1 ps in usual metals<sup>62-64</sup> Therefore it can be assumed that during femtosecond laser interaction with solids the pulse width is very much less than the electron cooling time *i.e.*  $\tau_L \ll \tau_e$ . Also when the electron energy is less than the Fermi energy, the electron heat capacity and the nonequilibrium electron thermal conductivity are given by  $C_e = C_e' T_e$  (where  $C_e'$  is a constant) and  $k_e = k_0(T_e) (T_e/T_0)$  where  $k_0(T_e)$  is the conventional equilibrium thermal conductivity of the metal. Therefore, during the time when the laser pulse is *ON*, the electron lattice coupling can be neglected. Therefore the electron conduction term in the above equations is very small and therefore the differential equations (1.1) and (1.2) are reduced to a single equation given by

$$C_e' \frac{\partial T_e^2}{\partial t} = 2I_0 \alpha A \exp(-\alpha z) \quad (1.3)$$



which upon integration gives,

$$T_e(t) = \left\{ T_0^2 + \frac{2I_0\alpha A}{C_e} t \exp(-\alpha z) \right\} \quad (1.4)$$

Here  $I_0$  is the incident laser power density and  $T_0 = T_e(0)$  is the initial temperature of the electrons. When the laser light is terminated, the electrons must have attained maximum energy and since the thermal conduction to the lattice in femtosecond time scale can be neglected, the temperature of the electron is given by,

$$T_e(\tau_L) \approx \left( \frac{2I_0\tau_L\alpha}{C_e} \right)^{1/2} \exp\left(-\frac{z}{\delta}\right) \quad (1.5)$$

Assuming that the electrons were heated up well above the ambient temperature  $T_0$  i.e.  $T_e(\tau_L) \gg T_0$  and also that the absorption of the electromagnetic radiation takes place only upto the skin depth  $\delta (= 2/\alpha)$ .

Thus the electrons have attained the maximum energy during the laser pulse and now the energy is being transferred to the lattice when the laser pulse is *OFF*. The electron energy is now being transferred to the lattice which has an initial temperature  $T_i = T_0$ . The electrons are rapidly cooled due to energy transfer to the lattice in picosecond time scales and heat conducts to the bulk and the lattice temperature  $T_i$  is given by<sup>60</sup>

$$T_i \approx \frac{I_a\tau_L}{C_i} \exp(-\alpha z) \quad (1.6)$$

Significant evaporation occurs when  $C_i T_i$  becomes larger than  $\rho\Omega$ , where  $\rho$  is the density and  $\Omega$  is the specific heat of evaporation per unit mass i.e. when the energy deposited

inside the target per unit mass exceeds the specific heat of vaporization per unit mass. Therefore the condition for strong evaporation becomes

$$F_a \geq F_{th} \exp(\alpha z) \quad (1.7)$$

where  $F_a = I_a \tau_L$  is the absorbed laser fluence and  $F_{th} = \rho \Omega / \alpha$  is the threshold laser fluence for evaporation. Also the ablation depth per pulse  $L$  has a logarithmic dependence on the laser fluence of the form,

$$L \approx \alpha^{-1} \ln \left( \frac{F_a}{F_{th}} \right) \quad (1.8)$$

Therefore during femtosecond pulse interaction with solids, the energy is absorbed and during the process of energy transfer to the lattice the laser pulse is *OFF*.

### 1.1.2 Interactions in picosecond time scales

In the case of picosecond laser interactions, the conditions on various time scales become  $\tau_e \ll \tau_L \ll \tau_i$ . That is, the laser pulse length becomes much larger than the electron cooling time. But the lattice heating time still remains less than the width of the laser pulse. Therefore by neglecting  $T_0$  the temperature  $T_i$  becomes<sup>60</sup>

$$T_i \approx T_e \left\{ 1 - \exp \left( -\frac{t}{\tau_i} \right) \right\} \approx \frac{t}{\tau_i} T_e \quad (1.9)$$

That is, the lattice temperature remains much less than the  $T_e$  during the laser pulse. The electron temperature at the end of laser pulse is given by,

$$T_e \approx \frac{I_a \alpha}{\gamma} \exp(-\alpha z) \quad (1.10)$$

and the temperature after the electron energy being transferred to the lattice is given by

$$T_i \approx \frac{I_a \tau_L}{C_i} \exp(-\alpha z) \quad (1.11)$$

Therefore the expression for  $T_i$  is the same both is the femtosecond and picosecond time scales and the logarithmic dependence of the ablation depths on the laser pulse remains true during picosecond laser pulse interactions also.

### 1.1.3 Interactions in nanosecond time scales

In the nanosecond case the condition  $\tau_L \gg \tau_i$  is fulfilled. Thus, there is enough time for the electron and lattice temperatures to be in equilibrium, *i.e.*  $T_e = T_i = T$  and in that case, the equations (1.1) and (1.2) reduce to a simple equation of the form,

$$C_e \frac{\partial T}{\partial t} = k_0 \frac{\partial^2 T}{\partial z^2} + I_0 \alpha \exp(-\alpha z) \quad (1.12)$$

The threshold required for strong evaporation *i.e.* the energy required to be deposited inside the target per unit mass equals or exceeds the specific heat of vaporization per unit mass, is given by<sup>65</sup>

$$I_{th} \approx \frac{\rho \Omega D^{1/2}}{\tau_L^{1/2}} \quad (1.13)$$

or

$$F_{th} \approx \rho \Omega D^{1/2} \tau_L^{1/2} \quad (1.14)$$

That is, the threshold laser fluence which is necessary for evaporation grows as  $\tau_L^{1/2}$ .

## 1.2 Mechanisms of laser ablation

Pulsed laser ablation is again classified according to the interaction processes, the heating

rate and the laser power density. The various processes include phase explosion, normal vaporization, normal boiling, sub-surface heating etc. A usual assumption is that the absorbed energy heats up the target surface to the melting point and then to the vaporization temperature which is not always true. The various target vaporization processes are briefly described below. In what follows is a description of the processes which occur after the electron energy is transferred to the lattice.

### 1.2.1 Phase explosion

At laser intensities of the order of  $\text{GW cm}^{-2}$  or higher obtained using nanosecond or even shorter laser pulses, instead of the combined effect of melting and vaporization, the process of *phase explosion* occurs. If the heating rate is sufficiently high, the influence of the evaporation from the surface of the liquid metal on the transport of material is very weak.<sup>33</sup> The material is directly vaporized from the solid phase and the surface temperature exceeds the vaporization temperature within a fraction of the laser pulse duration and the energy dissipation through vaporization is rather low. Therefore the surface layer is vaporized, the temperature of the underlying material will become equal to that of the vaporization temperature. The pulsed heating makes it possible to establish experimentally a metastable state in the liquid lying between the binodal and the critical point in the saturation curve in a phase diagram. A metastable liquid has an excess energy so that it decomposes exclusively into liquid and vapor phases. Such a process is termed as *phase explosion*.<sup>33</sup>

With weak superheating of the liquid, the phase explosion occurs primarily due to heterogeneous nucleation which appears at the existing nucleation centers (for example, gaseous inclusions). Since there are only a few centers, the phase transition in this case occurs rather slowly. But near the thermodynamic critical point there can be a homogeneous formation of vapor nuclei because of fluctuations in the liquid. The frequency of homogeneous nucleation at a temperature  $T > T_0$  is given by<sup>32</sup>

$$J = B \exp\left(-\frac{\Delta G_n}{kT}\right) \quad \text{nuclei cm}^{-3} \text{ s}^{-1} \quad (1.15)$$

where  $\Delta G_n$  is the change in the Gibb's free energy during the formation of a spherical critical nucleus,  $B$  is a weak function of temperature and pressure in comparison with the exponential factor. Calculations show that considerable superheating is required for the realization of homogeneous nucleation in liquid metal.<sup>32</sup> Under non-stationary conditions, the rate of nucleation is given by

$$J(t) = J \exp\left(-\frac{\tau}{t}\right) \quad (1.16)$$

where  $t$  is the time and  $\tau$  is the time for the establishment of non-stationary nucleation after instantaneous superheating of the liquid which is estimated<sup>32</sup> to be 10-100 ns. After giving appropriate values to the constants, the rate of nucleation is given by<sup>2</sup>

$$J = 1.5 \times 10^{32} \exp\left(-\frac{\Delta G_n}{k_B T}\right) \quad \text{nuclei cm}^{-3} \text{ s}^{-1} \quad (1.17)$$

To have an estimate of the rate of nucleation, let us take the example of Cesium as given by Martynyuk.<sup>32,33</sup>  $J = 1 \text{ nucleus cm}^{-3} \text{ s}^{-1}$  at  $T = 0.874 T_c$  and  $J = 10^{26} \text{ nucleus cm}^{-3} \text{ s}^{-1}$  at  $T = 0.905 T_c$ . Therefore  $J$  is numerically significant only near the thermodynamic critical temperature. Kelly and Miotello<sup>2,3</sup> show that the nucleation process has a time constant comparable to the laser pulse width. Because of the short time scale, the system passes beyond the boiling temperature to a temperature below the thermodynamic critical temperature, when the tensile strength of the liquid drops to zero and density fluctuations occur.<sup>66,67</sup> As a result of the above discussed processes, the near surface region of the surface relaxes explosively into a mixture of vapor and equilibrium liquid droplets. The observation of the liquid droplets as well as the vapor has been done by many researchers

who have been involved in experimental measurements and imaging<sup>68</sup>.

During phase explosion fractional vaporization is negligible and this process is considered to be non-thermal. An order of magnitude estimate of the pressure developed at the ablation spot is given by<sup>69</sup>

$$P_a = 21.4 \times 10^{-6} \left( \frac{I^3}{\lambda \tau_L^{1/2}} \right)^{1/4} \quad \text{atmospheres} \quad (1.18)$$

Here  $I$  ( $\text{W cm}^{-2}$ ) is the laser power density,  $\lambda$  (cm) is the laser wavelength and  $\tau_L$  is the laser pulse width in seconds. An estimate of the pressure developed at the ablated spot can be done with a laser intensity  $10^{10}$   $\text{W cm}^{-2}$  and laser pulse duration 10 ns, which has typical values of  $10^4$  atmospheres. Therefore the resulting expansion of the ablated material to the low pressure ambient should be described after taking into account the concepts of gas dynamics.

For phase explosion to be a possible sputtering mechanism, the necessary condition is that the laser power density is sufficiently high and the pulse width sufficiently short so that the target reaches  $\sim 0.9 T_{ic}$  at and beneath the surface where  $T_{ic}$  is the thermodynamic critical temperature. The thermodynamic critical temperature constitutes the upper limit to which the temperature of the target surface can be raised and it should be noted that similar upper limits do not apply to the particles in the plume. *Homogeneous* bubble nucleation occurs and the target makes a rapid transition from superheated liquid to a mixture of vapor and equilibrium liquid droplets.

### 1.2.2 Normal vaporization

The phenomenon of vaporization is predominant when the laser pulse duration is in microseconds or longer and when the laser power density<sup>70</sup> is  $\leq 10^6$   $\text{W cm}^{-2}$ . The electron phonon energy transfer takes place on a time scale of  $\sim 0.1$  picoseconds and the absorbed energy is rapidly converted into heat. Heat dissipation is very fast compared to the

duration of the laser pulse. The depth of vaporization depends critically on the thermal conductivity and thermal diffusivity of the materials. In principle, normal vaporization can happen essentially at any laser intensity and pulse length. The target undergoes normal vaporization from the extreme outer surface. Nucleation in the vapor plume does not enter into picture. Since the vapor pressure is non-zero at all temperatures exceeding 0 K, the surface temperature is not fixed.

### 1.2.3 Normal boiling

In the process of normal boiling, the material is first melted and then evaporated. The interaction is predominantly thermal in origin and hence elements of higher vapor pressure will be enriched in the vapor resulting in fractional vaporization. If the pulse length is sufficiently longer, heterogeneous nucleation occurs and the target undergoes *normal boiling* from a zone extending from the surface to a depth related to the absorption length. The surface temperature remains fixed and the temperature gradient at and beneath the surface is zero.

### 1.2.4 Sub-surface heating model

In sub-surface heating model, the target surface is heated either to the melting or to the boiling temperature followed by rapid vaporization. Therefore the surface is subjected to cooling and the sub surface region retains higher temperature. As a result, the pressure is much higher beneath the surface and a type of explosion takes place which is similar to *phase explosion*.<sup>35,71</sup> Such a mechanism of ablation is not forbidden for temperatures above  $T_{lc}$  which in turn is not permitted at the surface of a condensed phase. Therefore it is not said to be a likely process in laser ablation according to the arguments given by Kelly and Miotello<sup>2,3</sup>

## 1.3 Effect of collisions on time of flight profiles

During expansion into the ambient, the atoms and ions attain very high velocities of the order of  $10^5 - 10^6 \text{ cm s}^{-1}$ . The time taken by these species to travel specific distances above the target surface is a measure of the velocity of these species. Such measurements

are referred to as time of flight (TOF) measurements and there exist different ways such as optical emission spectroscopy, mass spectroscopy, electronic probes etc. for monitoring the time of flight profiles. In a laser produced plasma, TOF profile obeys an elliptical Maxwell-Boltzmann distribution of the form<sup>72</sup>

$$N(t) = \frac{\zeta}{t^3} \exp \left\{ -\frac{m}{2k_B T_{xy}} \left[ \left( \frac{x}{t} \right)^2 + \left( \frac{y}{t} \right)^2 \right] - \frac{m}{2k_B T_z} \left( \frac{z}{t} - u \right)^2 \right\} \quad (1.19)$$

where  $t$  is the flight time,  $\zeta$  is a scaling factor,  $m$  is the fragment mass and  $u$  is the stream velocity.  $T_{xy}$  is the component of the equivalent temperature of the species in the  $x$  and  $y$  directions (same in both directions) and  $T_z$  that in the  $z$ -direction (propagation direction). The temperature at the surface is calculated by assuming either isothermal expansion<sup>73</sup> or adiabatic expansion.<sup>74</sup>

Usually the observed kinetic energies are much larger than that estimated from the species temperature similar to that in eqn. (1.19). TOF profile as calculated from eqn.(1.19) is true in a collisionless case. But the collisions inside the plasma cannot be neglected at high laser power densities,<sup>75</sup> and the particles undergo several collisions during expansion is to vacuum. The effect of collisions in a supersonic jet expansion is to get a more directed motion of the beam.<sup>76</sup> Collisions make the kinetic energy (KE) distribution narrow, but with larger peak velocity. In addition, collisions can cool the rotational and vibrational energies of molecules in this expansion thereby converting the rotational and vibrational energies to translational energy. A further broadening of the velocity distributions may occur due to the formation of the so called Knudsen layer (KL) which happens with a minimum of 3 collisions per particle.<sup>77</sup> Knudsen layer is formed within a few mean free paths from the target where negative velocities develop among the particles. In order to have the momentum conservation, a positive flow velocity (center of mass velocity) also develops for the species. According to the collisional



expansion model, the surface temperature  $T_s$  is related to the KE of particles through the relation  $KT_s = E/\eta$  where  $\eta$  ranges from 2.52 for monatomic species to 3.28 for polyatomic species.<sup>78</sup> In the collisionless case  $\eta$  takes the usual value of 2.

In the presence of collisions in the plasma and KL formation the *half-range* Maxwellian velocity distribution for various species in collisionless plasma gets modified into a *full-range* Maxwellian in a center of mass system. Correspondingly, the exponential part of the distribution function for the velocity component normal to the system changes from

$$\exp(-mv_x^2 / kT_s) \quad v_x > 0 \quad (1.20a)$$

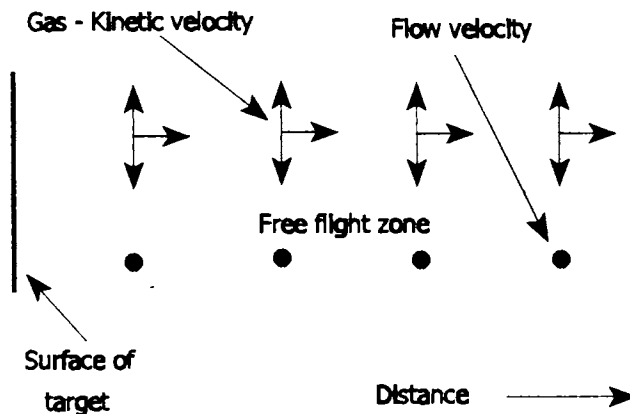
to

$$\exp[-m(v_x - u_K)^2 / 2kT_K] \quad -\infty < v_x < \infty \quad (1.20b)$$

where  $u_K$  is the center of mass velocity similar to the velocity of sound.  $T_K$  is about 70% of  $T_s$  for monatomic species.<sup>79</sup> A *Knudsen layer* can also be defined as the layer at which the above mentioned change in velocity distribution occurs.

When the number densities are still higher, the downstream boundary of the *Knudsen layer* acts like the throat of nozzle leading to the phenomenon of unsteady adiabatic expansion. The exponential part of the Maxwell-Boltzmann distribution is similar to eqn. (1.20b) with the distinction that here  $u_K$  is greater than sound velocity and the temperature<sup>80</sup> is less than  $T_K$ . Moreover when *Knudsen layer* formation is a highly nonequilibrium collision process, *unsteady adiabatic expansion* is an equilibrium phenomenon. Beyond the *Knudsen layer* boundary the system is better described by the formalism of unsteady adiabatic expansion. At still farther distances, in situations with three spatial dimensions, or in situations with short enough pulse widths, a stage is reached where there is no further interactions, the so called freezing length. The schematic showing all these processes is given<sup>2</sup> in Figure 1.2. The Knudsen layer,

(a) Collisionless expansion



(b) Expansion in the presence of collisions

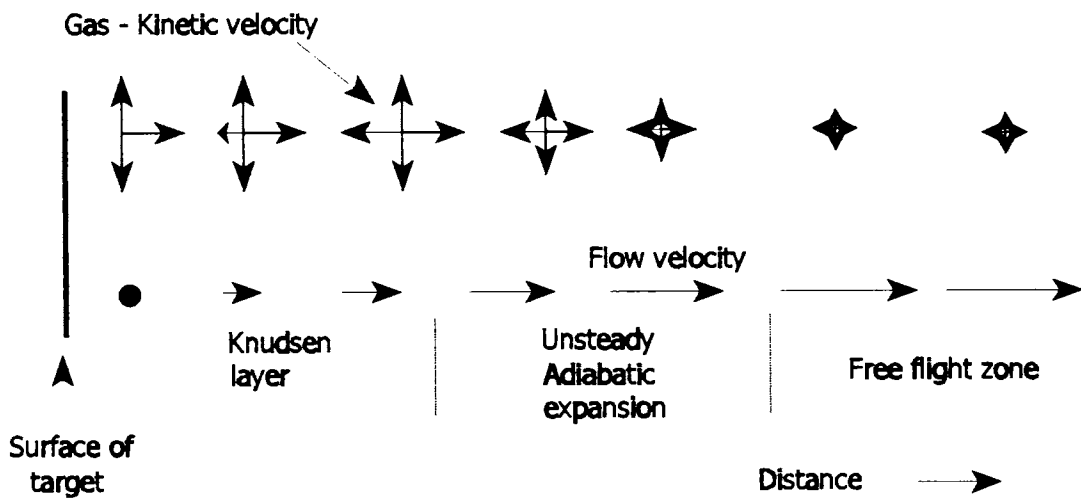


**Figure 1.2** (a) Schematic representation of particles emitted from a target surface which enter immediately into free flight. A continuous, one dimensional column of gas with  $v_x > 0$  and  $u = 0$  is assumed to arise. (b) Schematic representation of the formation of a Knudsen layer followed by an unsteady adiabatic expansion and free flight. The gas nearest the target surface is characterized by  $v_x > 0$  and  $u = 0$ , while at the KL boundary the gas shows  $-\infty < v_x < \infty$  and  $u = u_K$  [The figure is reproduced from R Kelly and A Miotello, *Nucl. Instr. Meth. Phys. Res.* **122** (1997) 374]

unsteady adiabatic expansion zone and free flight zone are shown separately and the distances between them are not according to the scale.

In order to describe the exact situation of collisional expansion, the emitted particles are divided into three groups. The first class expands collisionless and is described by a *half-range* Maxwell Boltzmann distribution. The second class forms the *Knudsen layer* due to collisions and the velocity distribution is given by<sup>78</sup>

$$f_K^\pm(v_x, v_y, v_z) \propto \exp\left\{-\frac{2E_I + m[(v_x - u_K)^2 + v_y^2 + v_z^2]}{2kT_K}\right\} \quad (1.21)$$

$-\infty < v_x, v_y, v_z < \infty$ . Here  $v_i$  ( $i = x, y, z$ ) stands for the velocity components,  $E_I$  is the total internal energy,  $m$  is the mass and  $T_K$  the temperature less than  $T_s$ . A third class of particles recondense at the target surface and is ascribed a distribution function  $f_K^-$  with  $v_x < 0$  and the sticking probability is assumed to be unity. There are situations in which the sticking coefficients are not unity and the particles are retro-reflected.<sup>81</sup> Also *Knudsen layer* causes the TOF spectra to be displaced to higher velocities, simulating higher values of  $T_s$  for on-axis measurements. For off-axis measurements, the TOF spectra are displaced to lower peak velocities simulating lower values<sup>82</sup> of  $T_s$ . The formation of *Knudsen layer* considerably alters the angular distribution of the ablated species. *Knudsen layer* causes the angular distribution to evolve from  $\cos\theta$  to more nearly  $\cos^4\theta$ .

#### 1.4 Some useful ablation parameters

In order to have a basic idea of the various plasma conditions that exist at the laser focal spot, numerical estimations can be made using the following formulae.<sup>69</sup> The parameters are calculated with a laser intensity  $10^{10}$  W cm<sup>-2</sup>, laser wavelength 1064 nm and laser pulse width 10 ns

$$\text{Pressure:} \quad P_a = 21.4 \times 10^{-6} \left( \frac{I^3}{\lambda \tau_L^{1/2}} \right)^{1/2} \approx 10^4 \text{ atm} \quad (1.22)$$

$$\text{Temperature:} \quad T_e = 2.8 \left( I \lambda \tau_L^{1/2} \right)^{1/2} \approx 29 \text{ eV} \quad (1.23)$$

$$\text{Plume density:} \quad n = 9 \times 10^{11} \frac{I^{1/4}}{\left( \lambda \tau_L^{1/2} \right)^{3/4}} \approx 3 \times 10^{20} \text{ cm}^{-3} \quad (1.24)$$

$$\text{Velocity:} \quad V = 0.37 \times 10^6 \left( I \lambda \tau_L^{1/2} \right)^{1/4} \approx 1.2 \times 10^6 \text{ cms}^{-1} \quad (1.25)$$

$$\text{Critical density:} \quad n_c = \frac{\omega^2 m_e \epsilon_0}{e^2} \approx 10^{21} \text{ cm}^{-3} \quad (1.26)$$

Here  $\omega = 2\pi\nu$  is the light angular frequency,  $\epsilon_0$  is the permittivity of free space,  $m_e$  is the electron mass and  $e$  is the electron charge. The quantities that have been calculated using the above equations exist at the ablation spot. Due to the highly transient nature of the plume, these quantities vary as time elapses and as the distance from the target increases.

### 1.5 Plasma shielding of laser light

Plasma shielding is a process by which the laser light is being prevented from reaching the target by several processes like inverse bremsstrahlung, atomic and/or ionic absorption etc. The laser induced surface plasma becomes optically dense at high laser power density. The latter part of the laser pulse will interact with the plasma and it will either be absorbed or reflected. The concept of plasma shielding was developed in the early 1970s by Ready.<sup>83</sup> Recently Russo and co-workers have done considerable amount of work on plasma shielding of the laser light as applied to both picosecond and nanosecond laser pulses.<sup>70,84</sup> They have shown that the initial fast electrons with

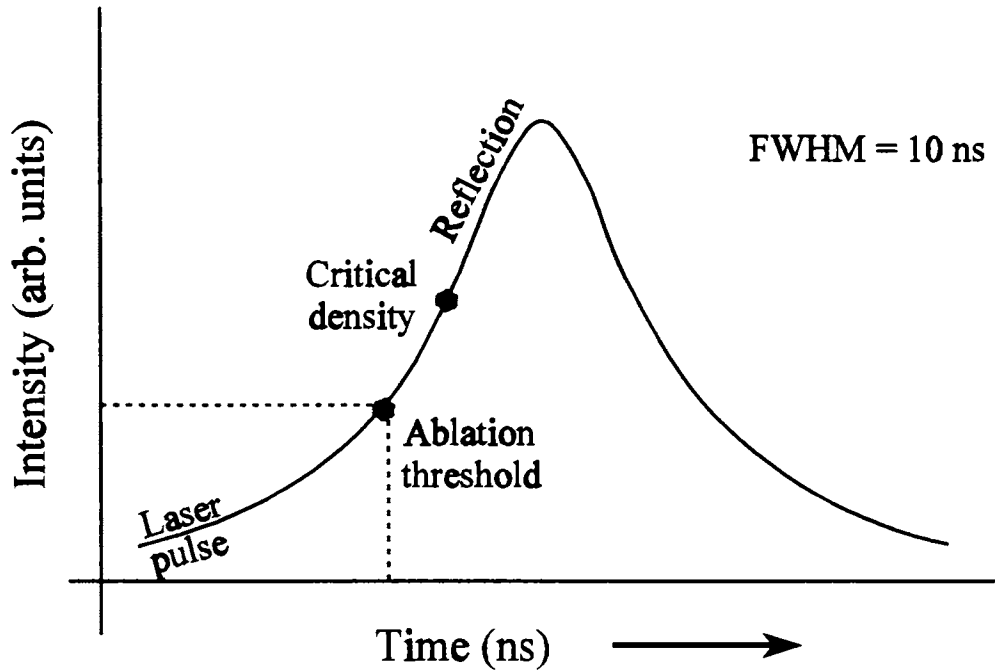


**Figure 1.3** Figure showing the various processes that are taking place during the laser pulse.

velocities of the order of  $10^9$  cm  $s^{-1}$  absorb laser photons during collisions with the support gas atoms due to inverse bremsstrahlung while picosecond laser interaction with solids. The role of atoms and ions is not so apparent since those species travel only a few angstroms (velocities of the order of  $10^6$  cm  $s^{-1}$ ) during a picosecond laser pulse. But during nanosecond laser pulse, the atoms and ions travel several micrometers from the target surface and it is these atoms/ions which absorb laser light through inverse bremsstrahlung upon collision with each other. There were no reports available on the observation of fast electrons contributing to plasma shielding in nanosecond laser ablation with solids until we have shown recently that there are laser heated photoelectrons present during nanosecond laser interaction with silver which contribute to plasma shielding.<sup>85</sup> Those results are also described in Chapter 4 of the thesis.

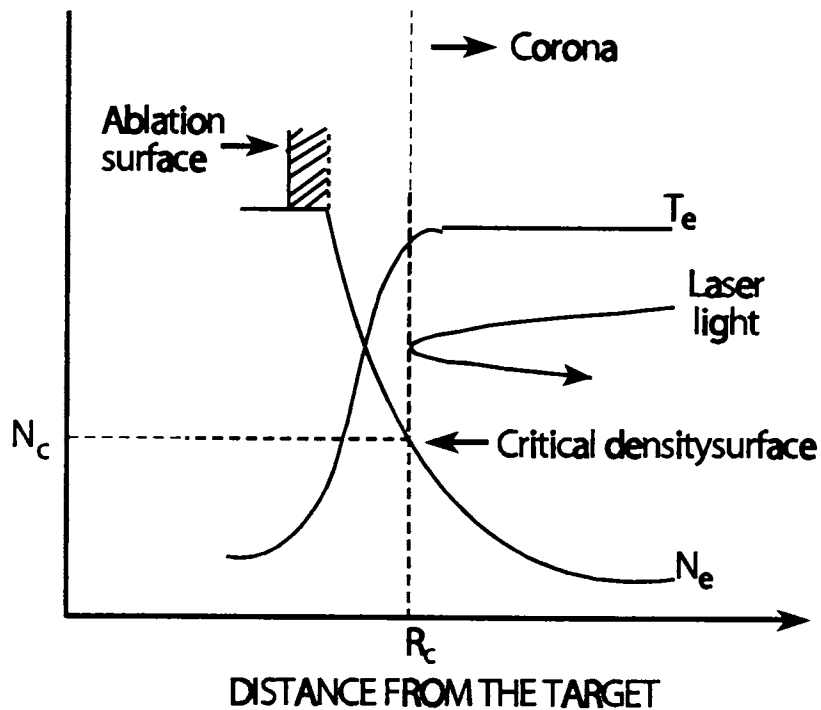


**Figure 1.4** Schematic showing the structure of the laser produced plasma.

The plasma from the solid targets are formed during the leading part of the laser pulse and the maximum thickness of the plasma plume at the end of the laser pulse is given by<sup>86</sup>  $l_0 \sim v_0 \tau_L$ . With  $v_0 = 10^5 - 10^6 \text{ cm s}^{-1}$  and  $\tau_L = 10 \text{ ns}$ ,  $l_0 \sim 10 - 100 \text{ } \mu\text{m}$ . That is during the period of the laser pulse, the plasma is confined to regions as small as  $10 - 100 \text{ } \mu\text{m}$ . Therefore the latter part of the laser pulse has to interact with a highly dense plasma with very small dimensions. These processes are shown schematically in Fig.1.3 Plasma is produced when the laser energy is reached above the ablation threshold for the material. The laser shielded off from reaching the target as the density of the plasma

exceeds the critical density. Thereafter the laser is reflected from the plasma in which it is shown that during the leading edge of the laser pulse itself, the energy exceeds the threshold for ablation. As the laser pulse evolves, the density at the ablation spot exceeds the critical density and the plasma become opaque to the laser radiation. Thereafter, the remaining part of the laser pulse is reflected. By using the above concepts, the structure of the laser plasma as it expands into the ambient is given in Fig.1.4 The outer region where the density is less than the critical density is called the corona, the region where the density is greater than the critical density is the conduction region. The boundary between the two is usually termed as the critical density surface.<sup>87</sup> The plasma has a steep density gradient along the target normal. The density has a larger value towards the target surface and at some point nearer to the target, the density exceeds the critical density which is defined in eqn. (1.26). The laser beam penetrates into the plasma only if the density is less than the critical density. Therefore the laser ablation plume consists of two regions, the outer corona ( $n_e \leq n_{ec}$ ) and the conduction region ( $n_e \geq n_{ec}$ ). A surface which separates the two is called the critical density surface. A sharp boundary between the conduction region and the outer corona should not be expected and hence the critical density surface may not be infinitely thin. The maximum length of the plasma can be calculated assuming spherical expansion as,

$$l_p = l f(\gamma) \left[ \frac{E_p}{\rho(\infty) l_0^3} \right]^{1/3\gamma} \quad (1.27)$$

where  $l_0$  is the initial length of the plume and  $f(\gamma) \sim 1$ . It should be noted that  $\gamma (= C_p/C_v)$  is the adiabatic index of the ablated plume and  $E_p$  is the thermal energy of the vapor plume.

### 1.6 Charged double layers in laser plasmas

When one speaks about plasma in general, the vital criterion which comes to the mind is the total charge neutrality which always remain true in any plasmas. But this charge neutrality can be violated locally which may lead to local electrical fields due to the

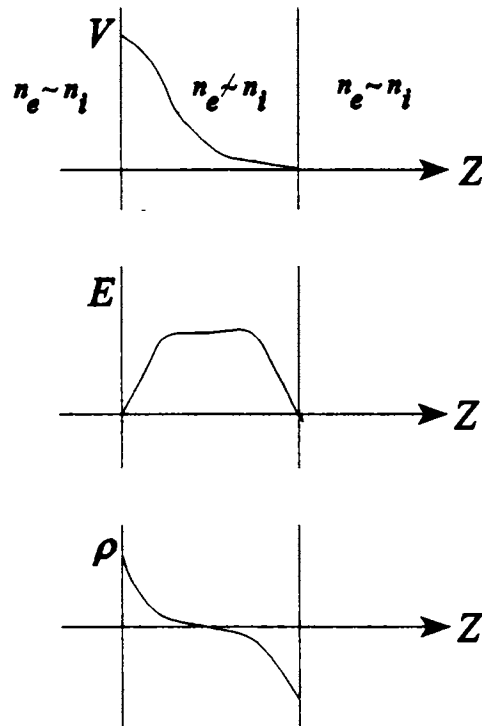


**Figure 1.5** Schematic description of the potential  $V$ , the electric field  $E$  and the charge density  $\rho$  in a static double layer

separated negative and positive charges and hence the concept of charged double layers arises. The charged double layer is defined as a discontinuity in the plasma potential. These electric double layers are regions of nonneutral plasma which induce a large potential drop thereby causing very strong electric fields. The positive and negative charges are separated by a characteristic distance which is of the order of the Debye length.<sup>88-90</sup> Double layers can be formed in a range of plasma densities which range from  $10^6$  to  $10^{21}$   $\text{cm}^{-3}$ . A precise definition of charged double layers can be given as two-dimensional charge densities of infinite magnitude with infinitely small distance such that a layer of dipoles of finite dimensions results.<sup>91</sup> A schematic of the potential  $V$ , Electric



field  $E$  and space charge density  $\rho$  as a function of distance across a static double layer is given in fig. 1.5 There are three conditions which exists for the formation of a charged double layer.<sup>90</sup> They are (i) the potential drop  $V$  through the layer must obey the relation,

$$V \geq \frac{k_B T_e}{e} \quad (1.28)$$

That is, the potential drop across the layers is of the order of the electron thermal energy. Here  $T_e$  is the plasma temperature at the layer boundary,  $k_B$  is the Boltzmann constant and  $e$  is the electron charge, (ii) quasi neutrality is locally violated in both space charge layers and (iii) global charge neutrality is ensured. This implies that the electric field is much stronger inside than outside the double layer. There are a number of theories such as Langmuir theory and Bohr theory which deal with the formation and dynamics of charged double layers and those are detailed in a review of the subject by Eliezer and Hora.<sup>90</sup> Detailed description is out of the scope of the present thesis and a general idea of the phenomena in connection with laser produced plasmas is given here.

A basic mechanism which lead to the formation of charged double layers is the absorption of the laser light by the electrons in the plasma. The two aspects of absorption which are of interest are (i) the fraction of the incident light that has been absorbed and (ii) the mechanism responsible for the absorption. As has been described earlier in Sec. 1.5 the laser light can penetrate to a depth which extends upto the critical density surface where the laser light is reflected. A further interaction will not go beyond the skin depth similar to that happen during the interaction of light with metallic surfaces. Out of the many processes like (i) Inverse bremsstrahlung absorption (ii) resonant absorption and (iii) absorption due to parametric instabilities, the process of inverse bremsstrahlung is primarily responsible for laser absorption below  $10^{13} \text{ Wcm}^{-2}$ . Eliezer & Hora<sup>90</sup> gives a comparison of the relative magnitude of the processes in their article.

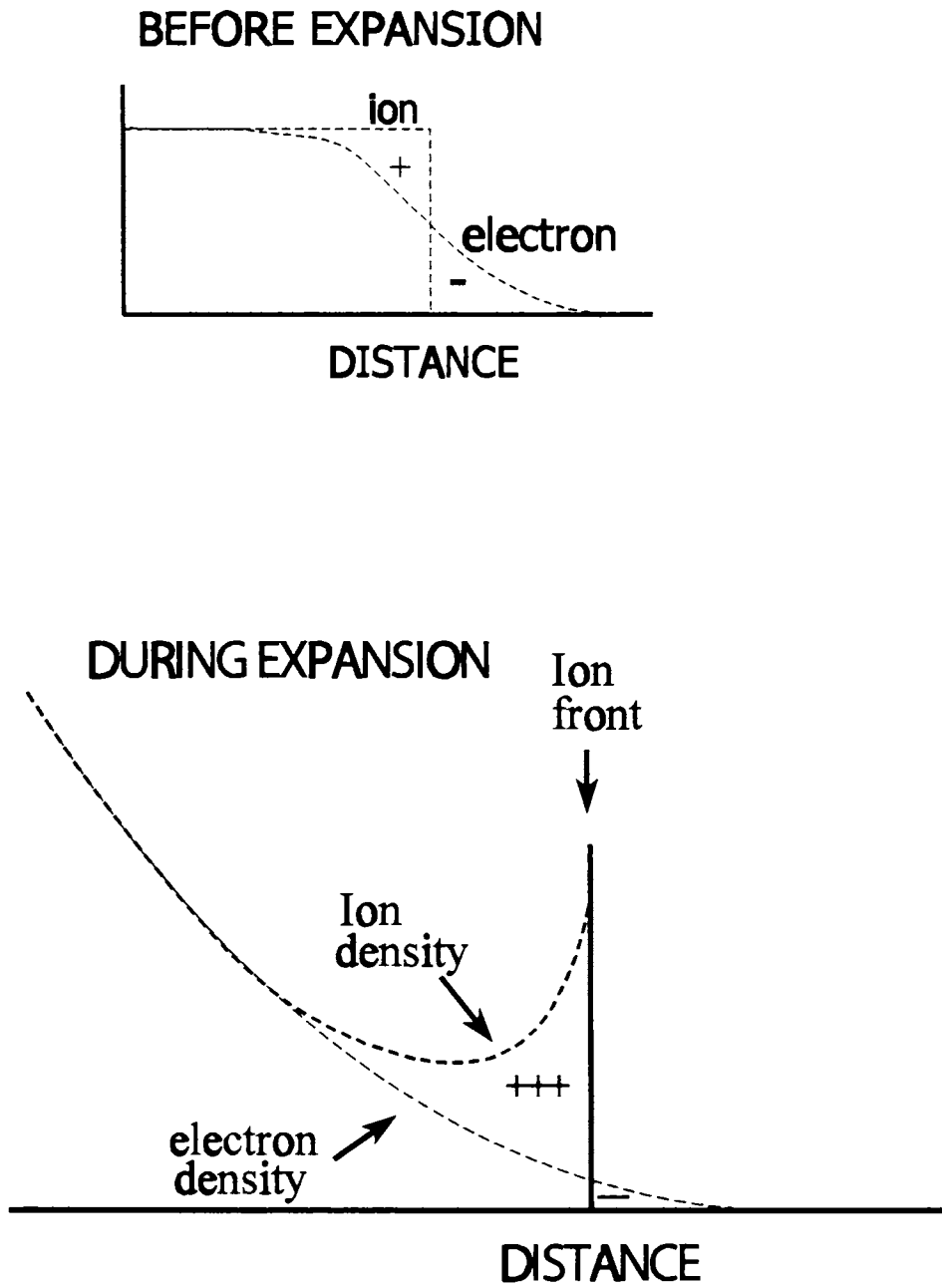


**Figure 1.6** Ion and electron densities in plasma before and during expansion [S Eliezer and H Hora *Phys. Rep.* 172 (1989) 339]

As has been discussed earlier, the irradiated matter consists of a dense inner core surrounded by a less dense and hot corona. The laser radiation is absorbed in the outer periphery of the plasma which extends upto the critical density surface defined as the region where the plasma frequency equals that of the laser light. Near the critical surface the electrons in the plasma are oscillating with the laser frequency so that the plasma refractive index becomes zero, the electromagnetic wave propagation ceases and total reflection occurs. The energy absorbed upto the critical density is transported inward to the ablation surface and outward into the expanding plasma. Transport of the heated electrons carries energy into plasma of greater than critical density layer. The electric field  $E$  is caused by the gradients of the electron density and temperatures, and is given by<sup>90</sup>

$$eE \cong \frac{1}{N_e} \frac{d}{dz} (3N_e k_B T_e) \quad (1.29)$$

under the assumption that  $T_e \gg T_i$ . At the critical density surface these gradients might cancel each other and therefore the extra contribution for nonlinear forces will play a crucial role in determining  $E$  because of the high laser power densities.

During the plasma adiabatic expansion, the ions are rapidly cooled and the electrons are heated up due to laser absorption. The electrons are thereby accelerated and attain more velocity which in turn will be spatially separated from the ions having greater inertia. The resulting charge separation ends up in the formation of charged double layers. Fig1.6 shows the ion and electron densities before and after the plasma expansion. At the plasma boundary there is a steepening of the ion front and the electrons density extends beyond the boundary and hence the formation of double layer and large potentials.

### 1.7 Effect of ambient gas

The ablated species expands into vacuum adiabatically due to the large pressure difference between the ablation spot and vacuum. The scenario is slightly different when

the expansion is in the presence of an ambient gas.<sup>92-104</sup> The interaction of the plasma plume with the ambient gas includes the formation of a shock front.<sup>105-110</sup> as well as chemical reactions.<sup>111,112</sup> The dynamics of the shock wave and plume expansion have been studied in detail using a variety of diagnostic techniques.<sup>113-119</sup> In shock wave model of plasma expansion, the ejected material acts like a piston which compresses the gas ahead of it and forms a shock wave. Most of the gas phase reactions happens at the shock layer.<sup>120</sup> The shock wave is basically a density discontinuity which moves very rapidly compressing the ambient molecules in front of the wave to form a denser layer thereby generating high temperatures. The position of the shock front ( $R_{sw}$ ) within the assumptions pertaining to strong explosions is given by<sup>109</sup>

$$R_{sw} \approx \xi \left[ \frac{Et^2}{\rho(\infty)} \right]^n \quad (1.30)$$

where  $\xi \approx 1$  The values of both  $\xi$  and  $n$  depends on the symmetry of the problem.  $n = 1/5$  for spherical expansion,  $n = 1/4$  for cylindrical symmetry for the shock front and  $n = 1/3$  for plane waves,  $\rho(\infty)$  is the undisturbed density of the ambient gas and  $E$  is the sum of the kinetic energy of the shock wave and the thermal energy of the vapor plume. The thickness of the shell which contains most of the mass of the shocked gas is<sup>72</sup>

$$\Delta R = R_{sw} \frac{\gamma - 1}{3(\gamma + 1)} \quad (1.31)$$

For strong shock waves when the pressure before the shock front ( $P_{sw}$ ) is very much larger than the ambient pressure ( $P(\infty)$ ) i.e  $P_{sw} \gg P(\infty)$ , the density ( $\rho_{sw}$ ) and temperature ( $T_{sw}$ ) at the shock front is<sup>121</sup>

$$\rho_{sw} = \rho(\infty) \frac{\gamma + 1}{\gamma - 1} \quad (1.32)$$

and

$$T_{sw} = T(\infty) \frac{\gamma - 1}{\gamma + 1} \frac{P_{sw}}{\rho(\infty)} \quad (1.33)$$

where the time dependent pressure is given by

$$P_{sw} = 2 \left( \frac{2\xi}{5} \right)^2 \left[ \frac{E^2 \rho^2(\infty)}{t^6} \right]^{1/5} \gg P(\infty) \quad (1.34)$$

Here  $\gamma$  and  $T(\infty)$  refer to background gas. Another consequence of the presence of the background gas is that the ablated species may react with ambient gas molecules resulting in the formation of various molecules in the vapor phase. Such reaction rates are very high near the contact front between the plume and the ambient gas since the turbulence in the plume causes fast mixing.

## 1.8 Spectroscopic diagnostics of laser plasmas

Optical emission spectroscopy has been widely used for the diagnostics of laser produced plasmas.<sup>122-126</sup> Emission spectroscopic methods can be employed for both space resolved and time resolved measurements and these are very important in the diagnostics of laser produced plasmas which are highly transient with steep density and temperature gradients.

### 1.8.1 Stark broadening of spectral lines

Electron density determination from the measured width of emission lines is one of the most powerful methods for plasma diagnostics.<sup>127-131</sup> The line shapes of emission lines are sensitive to local plasma conditions such as temperature, pressure and electron

density. The broadening occurs due to the microscopic electric field of the ions and electrons in the plasma. The Coulomb fields of individual ions and electrons are situated within a sphere of radius equal to the Debye length away from the radiator. In order to measure the electron densities from the stark broadened profiles, one has to ensure that other broadening mechanisms like Doppler broadening are a minimum. The Doppler broadening arises due to the randomness isotropy in velocity. But in a laser plasma the velocity distributions are highly anisotropic and almost unidirectional and Doppler broadening of spectral emission is a minimum. Another source of error is self-absorption along the line of sight. In that case, appropriate corrections has to be made to the observed line shapes. Also in the case of weak and very broad lines, the underlying continuum has to be subtracted before the stark width is measured.

In an actual experiment, the properly corrected line profile is matched with stark profile calculated for a range of electron densities. Calculated stark broadening parameters are available in standard tables.<sup>132,133</sup> Much more simple procedure for the evaluation of electron densities from stark broadening is based on the comparison of measured and calculated line widths. The line width (FWHM) of the stark broadened atomic line is given by<sup>134</sup>

$$\Delta\lambda_{1/2} = 2W\left(\frac{N_e}{10^{16}}\right) + 3.5A\left(\frac{N_e}{10^{16}}\right)^{1/4} (1 - 1.2N_D^{1/3})W\left(\frac{N_e}{10^{16}}\right) \quad (1.35)$$

Here  $N_e$  is the electron density,  $W$  is the electron impact width parameter,  $A$  is the line broadening parameter and  $N_D$  is the number of particles in the Debye sphere at a plasma temperature  $T_e$  which is given by

$$N_D = 1.72 \times 10^9 \frac{[T_e(eV)]^{3/2}}{[N_e(cm^{-3})]^{1/2}} \quad (1.36)$$

Therefore the electron density measurement from the width of spectral lines is fairly

straight forward. The first term in the right hand side of eqn. (1.35) gives the contribution of electron impact and the second that from ion impact. Usually, the contribution from the ions is neglected being very small and hence second term vanishes in eqn (1.35).

The stark widths and shifts are being used for the measurements of electron density of laser plasmas. For example, Smith & Peacock<sup>135</sup> used the wing intensities of the stark broadened Lyman lines, for which the upper level is thermally populated with respect to the free electrons and fully stripped ions enable the deduction of electron density in high temperature laser plasmas. Electron density of the order of  $10^{21} \text{ cm}^{-3}$  were determined by monitoring the width of C IV resonant lines in the X-ray region. Boiko<sup>136</sup> *et al.* successfully used the X-ray spectroscopic method to measure electron densities  $N_e > 10^{20} \text{ cm}^{-3}$  in laser plasmas with high electron temperature  $T_e > 0.2 \text{ keV}$ . The methods considered in those measurements were based on (i) relative intensities of resonance and intercombination lines in the spectra of Helium like ions (ii) relative intensities of satellite lines in spectra of Hydrogen like ions (iii) relative intensities of Hydrogen like resonance doublet components and (iv) stark broadening of the lines of Hydrogen like ions. Mehlman<sup>137</sup> *et al.* measured the temperature and density of laser produced plasmas using vacuum ultraviolet spectroscopy. In that case the electron densities were of the order of  $10^{18} \text{ cm}^{-3}$  and electron temperature between 2 and 4 eV. Kielkopf<sup>138</sup> measured the electron density from the stark broadened profiles of Hydrogen  $H_\alpha$  and  $H_\beta$  lines. Recently, Haynes<sup>139</sup> *et al.* computed the effect of ion dynamics and opacity on stark broadened line profiles in hot dense plasmas. Renner<sup>140,141</sup> *et al.* effectively utilized the shifts of the Lyman line series of aluminum in the X-ray region to numerically simulate the plasma densities in dense laser produced plasmas. Apart from all these, there are a number of reports which deal with the determination of electron density of laser produced plasmas using the stark broadened line profiles of emission lines.<sup>142,143</sup>

### 1.8.2 Determination of electron temperature using emission spectroscopy

In every plasma, there exists ionized species and electrons which counter balance to have total charge neutrality. Therefore in order to characterize the plasma, one has to look into the density and energy of these ions and electrons. The particle energy is in general expressed in terms of the temperature and the relevant temperature is that which describes the distribution function of the species dominating the radiative processes (in dense plasmas, temperature of electrons). Since the plasma is in high temperature state, there exist radiative processes and the emission can be anywhere in the electromagnetic spectrum depending on the central temperature of the plasma. The emission spectra from the plasma can give an in-depth information related to the temperature under certain equilibrium criteria which control the emission process. The two main equilibrium criteria are briefly described below.

#### 1.8.2.1 Local thermodynamic equilibrium

The spectroscopic diagnostics of a plasma requires certain local equilibrium conditions that must exist in each small volume element of the plasma. Then the densities in specific quantum states are those pertaining to a system in complete thermodynamic equilibrium. Both electrons and ions will have nearly Maxwellian velocity distributions in every small volume elements and in each short time interval. Eventhough the two kinetic temperatures are different, the Maxwellian velocity distribution ( $f$ ) have the general form,

$$f = \left( \frac{M}{2\pi k_B T_e} \right)^{3/2} \exp\left( -\frac{Mv^2}{2k_B T_e} \right) \quad (1.37)$$

Another condition for the existence of local thermodynamic equilibrium (LTE) is that the bound electrons are required to populate the discrete energy levels<sup>144</sup> in accordance with the Boltzmann distribution,



$$\frac{N_m}{N_n} = \frac{g_m}{g_n} \exp\left[-\frac{E_{m,n}}{k_B T_e}\right] \quad (1.38)$$

and the free particle densities are required to follow the Saha equation<sup>144</sup>

$$\frac{N^z N_e}{N^{z-1}} = 6 \times 10^{21} T^{3/2} \exp\left(-\frac{E_I^{z-1}}{T_e}\right) \text{ cm}^{-3} \quad (1.39)$$

Here  $N_e$  is the electron density in  $\text{cm}^{-3}$ ,  $N_m$ ,  $N_n$ ,  $N^z$  and  $N^{z-1}$  are the population densities in different levels viz.  $m$ ,  $n$  and the ground state (of neutrals and ions).  $z$  is the ionic charge,  $E_{m,n} = E_m - E_n$  is the energy difference between the levels  $m$  and  $n$  in eV.  $E_I^{z-1}$  is the ionization energy of species of charge  $z-1$  in the ground state.

In LTE, the ratio of the emissivity  $\varepsilon_\omega$  [ $\text{W cm}^{-3}$  per steradian per frequency interval ( $d\omega$ )] to the absorption coefficient  $\alpha_\omega$  ( $\text{cm}^{-1}$ ) in every volume element is a universal constant (Kirchoff's Law) equal to the Planck's blackbody intensity given by<sup>145</sup>

$$\frac{\varepsilon_\omega}{\alpha_\omega} \equiv B(\omega, T_e) = \frac{\hbar \omega^3}{4\pi^3 c^2} \left[ \exp\left(\frac{\hbar \omega}{k_B T_e}\right) - 1 \right]^{-1} \text{ W cm}^{-2} \text{ sr}^{-1} (d\omega)^{-1} \quad (1.40)$$

Here  $c$  is the speed of light and  $\omega$  is the angular frequency of the emitted light.

In LTE, the electron-atom and electron-ion collision processes must be extremely rapid and must dominate the plasma rate equations. Therefore LTE will be approached only at sufficiently large particle densities. A necessary (not sufficient) condition for the existence of LTE<sup>144,145</sup> is that

$$N_e \geq 1.4 \times 10^{14} T_e^{1/2} E_{mn}^3 \text{ cm}^{-3} \quad (1.41)$$

where  $T_e$  and  $E_{mn}$  are in eV. Since the ionization potentials are different for the lower and

upper levels, the complete collision dominated equilibria is difficult to achieve for all the energy levels. If low lying levels do not participate in the physical problem under study and can therefore be left out of consideration, one may arrive at the condition for partial LTE for higher lying levels in the form<sup>146</sup>

$$N_e \geq 7 \times 10^{18} \frac{z^6}{n^{17/2}} \left[ \frac{k_B T_e}{E_H} \right]^{1/2} \text{ cm}^{-3} \quad (1.42)$$

where  $E_H$  is the ionization potential of hydrogen and  $n$  is the principal quantum number of the level.

### 1.8.2.2 Corona equilibrium

When the electron density is too low for complete LTE, another class of steady state equilibrium become applicable. In such cases, the electron collisional excitation and ionization is no longer balanced by collisional de-excitation. But the collisional excitation is balanced by radiative recombination and spontaneous decay. The distribution function of free electrons is still Maxwellian and Kirchoff's law also holds. But the Saha equation is now replaced by a new relation for fractional ionization<sup>146,147</sup>

$$\frac{N^z}{N^{z-1}} = \frac{S}{\alpha_R} \quad (1.43)$$

where  $S$  is the collisional ionization coefficient and  $\alpha_R$  is the radiative recombination coefficient. The corona model is applicable in the parameter range given by

$$\frac{10^{12}}{\tau} \leq N_e (\text{cm}^{-3}) \leq 10^{16} [T_e (\text{eV})]^{7/2} \quad (1.44)$$

where  $\tau$  is the plasma relaxation time in seconds. In order to use spectroscopic techniques for the determination of the electron temperatures we assume one of the equilibrium

conditions, viz. LTE or coronal equilibrium conditions to hold. Then the temperature is determined using standard relations. After all, it is required to verify that the equilibrium conditions hold, using the measured quantities.

### 1.8.3 $T_e$ from relative line intensity measurements

The relative intensities of the lines from the same element at the same ionization state can be used to determine the electron temperature of the plasma. Two appropriate lines are selected from the spectrum and their intensities are used for the evaluation of  $T_e$ . This method is based on the fact that the densities of various excited states are proportional to the products of the statistical weights with the exponentials of the negative ratios of excitation energy and thermal energy  $k_B T_e$ . Assuming negligible self-absorption one may arrive at an equation for the electron temperature as<sup>146</sup>

$$k_B T_e = \frac{E' - E}{\ln \left( \frac{I \lambda^3 g' f'}{\Gamma \lambda'^3 g f} \right)} \quad (1.45)$$

where  $I$ ,  $\lambda$ ,  $g$ ,  $E$  and  $f$  are the total intensity integrated over the profile, wavelength, statistical weight of the lower state of the line, excitation energy and absorption oscillator strength respectively, of one line. The primed quantities are that of the other line. Therefore the measurement is straight forward once all these parameters are known. The major source of error (10 - 30%) in the above equation is that for the value of oscillator strength.  $k_B T_e$  is typically of the order of the largest separation  $E' - E$  between excitation energies of nonresonance lines. Therefore lines must be selected in such a way that  $E' - E$  is much greater than a  $k_B T_e$  to be measured. If one has to take into account the deviations from the LTE conditions, the above equation is modified to,

$$k_B T_e = \frac{E' - E}{\ln \left( \frac{I E^3 \lambda^3 g' f'}{I' E'^3 \lambda'^3 g f} \right)} \quad (1.46)$$

This equation is valid only if electron densities are such that the criterion in Eqn.(1.42) is underfulfilled at least by an order magnitude for both upper levels.

Relative line intensity measurements for the same element and ionization state do not give very accurate results because of the relatively small value of  $E' - E$  when visible light is used for the measurements. Then the line intensity ratio becomes rather insensitive to temperature variations. Now the successive ionization stages of the same element can be utilized for  $T_e$  measurements since now the value of  $E' - E$  is enhanced by the value of the ionization energy. In that case, under conditions of LTE, the ratio of line intensities are given by<sup>146</sup>

$$\frac{I'}{I} = \frac{f' g' \lambda'^3}{f g \lambda^3} (4\pi^{3/2} a_0^3 N_e)^{-1} \left( \frac{k_B T_e}{E_H} \right)^{3/2} \exp \left( - \frac{E' + E_I - E - \Delta E_I}{k_B T_e} \right) \quad (1.47)$$

Primed quantities refer to the line for higher ionization state and  $\Delta E_I$  is the reduction of ionization energy  $E_I$  of the lower ionization energy given by<sup>146</sup>

$$\Delta E_I = \frac{ze^2}{4\pi\epsilon_0\lambda_D} \quad (1.48)$$

Here  $z$  is the charge of the ion,  $e$  is the electron charge,  $\epsilon_0$  is the permittivity of free space and  $\lambda_D$  is the Debye radius, the typical length to which the electric field of an individual charged particle extends before it is effectively shielded by the oppositely charged particles in the neighborhood. The expression for the Debye length has a general form given by

$$\lambda_D = \left( \frac{\epsilon_0 k_B T_e}{e^2 N_e} \right)^{1/2} \quad (1.49)$$

The intensity ratio given in eqn.(1.47) depends on electron densities and the measurement of electron temperature using this equation is accurate only above a density of  $10^{17} \text{ cm}^{-3}$ . To extend the measurements to lower electron densities, the conditions of corona equilibrium is used and then the intensity ratio is given by<sup>146</sup>

$$\frac{I'}{I} \approx \frac{f' g' \lambda^3}{f g \lambda^3} \exp\left( \frac{E'_I - E'_I - E_I + E}{k_B T_e} \right) \frac{S}{\alpha_R} \quad (1.50)$$

The intensity ratio is now independent of electron density. Electron temperature measurements in laser produced plasmas were effectively carried out by several authors using spectroscopic methods from the ratio of the intensities of emission lines. The method assumes the validity of complete thermodynamic equilibrium or corona equilibrium for less dense plasmas. The method has been successfully utilized in several experiments on plasma diagnostics.<sup>129,147-154</sup> In some of the reports the validity of the results were checked by evaluating the conditions for LTE in the plasma.<sup>155-157</sup> Other methods which use light for the plasma parameters in laser produced plasmas are Thomson scattering<sup>158</sup> interferometry.<sup>159-163</sup>

### 1.9 Plasma diagnostics using Langmuir probes

The Langmuir probe is a simple instrument which contains only a piece of wire but capable of giving valuable information regarding the plasma parameters like the electron temperature and density. The volt-ampere (V-I) characteristics contains the information about the temperature of the plasma. The bias voltage is usually applied relative to the ground potential. The Langmuir probe theory assumes that the plasma quiescent and homogeneous and that the electrons and ions are in separate thermal equilibrium with the electron temperature very much higher than the ion temperature. Fig.1.7 gives a typical

plot of the V-I characteristics of the Langmuir probe. When the probe is highly negatively biased it collects all positive ions entering the plasma sheath while the electrons are repelled. This is the saturation ion current given by

$$i = \frac{n_i v_i A}{4} \quad (1.51)$$

where  $n_i$  is the ion density,  $v_i$  is the ion velocity and  $A$  is the probe area. As the probe is made more positive, the net current flow starts to decrease because the highest energy electrons overcome the applied bias and reach the probe. When the potential reaches  $V_f$ , there is no net current through the probe. At  $V_f$  electrons are repelled to the point that their current is just equal to the ion current. This potential is called floating potential and is the voltage at which the probe would assume as if it were not connected via external circuits to any voltage source. An expression for the floating potential is given by<sup>164</sup>

$$V_f = \frac{k_B T_e}{2e} \ln \left( \frac{m_i}{2\pi m_e} \right) \quad (1.52)$$

where  $m_i$  is the ion mass. As the probe is made more positive, electrons with still lower energies can reach the probe surface and the current increases further. For all positive potentials, the probe is surrounded by a sheath of electrons and the sheath produces a space charge barrier that inhibits further electron collection. As the applied probe voltage<sup>165,167</sup> reaches the plasma potential,  $V_p$ , (shown in Fig.1.7) the fluxes of ions and electrons correspond to the random currents due to thermal motion and probe bias voltage changes from electron retarding to electron accelerating. Above  $V_p$  the collected probe current should reach a saturation value  $I_e(sat)$  from which the electron density is calculated using the formula<sup>165,166</sup>

$$I_e(sat) = \frac{1}{4} n_e v_e A \quad (1.53)$$

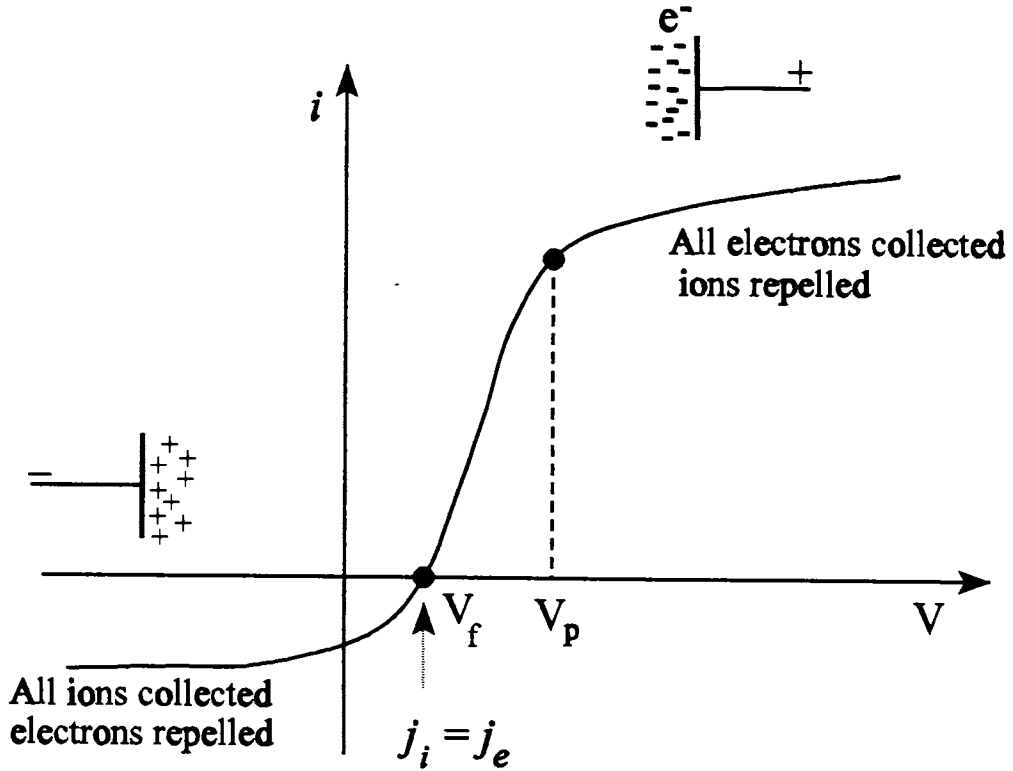


**Figure 1.7** A typical V-I characteristics of Langmuir probe.  $V_f$  is the floating potential where the ion current equals the electron current.  $V_p$  is the plasma potential which is obtained from the position of the knee of the electron saturation portion of the V-I characteristics (Figure reproduced from D L Flamm and G K Herb in *Plasma etching: An introduction* by D M Manos and D L Flamm (Eds.) (Academic press, New York 1989) p.31)

where  $v_e$  is the electron velocity given by

$$v_e = \left( \frac{8k_B T_e}{\pi m_e} \right)^{1/2} \tag{1.54}$$

Here  $m_e$  is the mass of electron. In actual situation the electron current does not saturate completely indicating that the effective probe area is increasing with probe voltage.<sup>165,167</sup>

Assuming that the electrons satisfy a Maxwellian distribution, one can arrive at a relation between the probe current and the applied voltage when the probe is increasingly negative<sup>165</sup>

$$I_e = \frac{1}{4} n_e v_e A \exp\left(-\frac{eV}{k_B T_e}\right) \quad (1.55)$$

where  $I_e$  is the probe current due to electrons,  $V$  is the applied probe voltage,  $k_B$  Boltzmann constant and  $T_e$  is the electron temperature. It is evident from the above equation that a plot between  $\ln(I_e)$  and  $V$  will yield a straight line with slope  $e/k_B T_e$  from which the electron temperature can be determined.

### 1.10 Summary

The laser matter interaction and plasma formation are very complex and the phenomena taking place are innumerable. This introductory chapter deals with the various processes taking place in the laser produced plasma which are relevant to the understanding of the work described in the coming chapters. The absorption of the laser light by the target is discussed in the beginning and the ablation mechanisms thereafter. Next the interaction of the laser light with the plasma and the formation of charged double layer is described. The chapter gives a brief idea of the general structure of laser plasmas. Since these are highly transient objects with large density gradients along the target normal, the description is given in terms of distance from the target. Some ablation parameters such as the pressure developed at the ablation spot, the velocity of the ablated species, the electron temperature, the particle density, the critical density of the plasma etc. are also defined and estimated in order to have an idea of the order of magnitude of these quantities. In the last part, the two plasma diagnostic techniques *viz.* optical emission spectroscopy and Langmuir probes which are used in the present investigations are



briefly given. The local thermodynamic equilibrium and corona equilibrium conditions are mentioned in connection with the spectroscopic diagnostics of the plasma.

## References

- <sup>1</sup>P D Maker, R W Terhune, C M Savage in *Proc. of Third International Conference on Quantum Electronics* by P Grivet and N Bloembergen (Eds.), Columbia Uty. Press, New York 1964 p.155
- <sup>2</sup>R Kelly and A Miotello, *Nucl. Instr. Meth. Phys. Res. B* **122** (1997) 374
- <sup>2</sup>R Kelly and A Miotello, *Appl Surf. Sci* **96-98** (1996) 205
- <sup>4</sup>D B Chrisey & G K Hubler (Eds.) *Pulsed laser deposition of thin films* John Wiley & Sons, New York, (1994) and references therein
- <sup>5</sup>T P Hughes *Plasmas and Laser light* (Adam Hilger, 1975)
- <sup>6</sup>J C Miller and R F Haglund (Eds.) *Laser ablation: Mechanisms and Applications* (Springer-Verlag, 1991)
- <sup>7</sup>R K Singh and J Narayan, *Phys. Rev. B* **41** (1990) 8843
- <sup>8</sup>R K Singh, H Holand and J Narayan, *J. Appl. Phys.* **68** (1990) 233
- <sup>9</sup>J C S Kools, T S Baller, S T De Zwart and J Dielman, *J. Appl. Phys.* **71** (1992) 4547
- <sup>10</sup>A V Bulgakov and N M Bulgakova, *J. Phys. D: Appl. Phys.* **31** (1998) 693
- <sup>11</sup>B Braren, K G Casy and R Kelly, *Nucl. Instr. Meth. Phys. Res. B* **58** (1991) 463
- <sup>12</sup>D H Lowndes, D B Geohegan, A A Puretzky, D P Norton and C M Rouleau, *Science* **273** (1996) 898
- <sup>13</sup>V Kumar and R K Thareja, *J. Appl. Phys.* **64** (1988) 5269
- <sup>14</sup>K L Saegner *Processing of Advanced Materials* **2** (1993) 1
- <sup>15</sup>K L Saegner *Processing of Advanced Materials* **3** (1993) 63
- <sup>16</sup>R Richter, *Thin Solid Films* **188** (1990) 275
- <sup>17</sup>S Amoruso, M Armenate, V Berardi, R Bruzzese and N Spinelli *Appl. Phys. A* **65** (1997) 265
- <sup>18</sup>B S Yilbas, Z Yilbas and N Akiakoyun, *Opt & Laser Tech.* **28** (1996) 503
- <sup>19</sup>R Srinivas and B Brurer, *Chem. Rev.* **89** (1989) 1303
- <sup>20</sup>J A Mc Mordie and P D Roberts, *J. Phys. D: Appl. Phys.* **8** (1975) 768

- <sup>21</sup>J R Ho, C P Grigoropoulos and J A C Humpfrey, *J. Appl. Phys.* **79** (1996) 7205
- <sup>22</sup>V P Silin, *Physica Scripta* **T63** (1996) 148
- <sup>23</sup>R Winkler and M W Wuttke, *Appl. Phys. B.* **54** (1992) 1
- <sup>24</sup>J M Green, W T Silfvast and O R Wood II, *J. Appl. Phys.* **48** (1977) 2753
- <sup>25</sup>P E Dyer, A Issa and P H Key, *Appl. Surf. Sci.* **46** (1990) 89
- <sup>26</sup>R W Dreyfus, *J. Appl. Phys.* **69** (1991) 1721
- <sup>27</sup>R Kelly, J J Cuomo, P A Leary and J E Rothenberg, *Nucl.Instr.Meth.Phys.Res. B* **7/8** (1985) 755
- <sup>28</sup>R Kelly, A Miotello, B Brare, A Gupta and Casey, *Nucl.Instr.Meth.Phys.Res. B* **65** (1992) 187
- <sup>29</sup>R Kelly *Nucl. Instr. Meth. Phys. Res. B* **46** (1990) 441
- <sup>30</sup>G Wedler and H Ruhmann, *Surf. Sci.* **121** (1982) 464
- <sup>31</sup>J P Cowin, B J Auerbach, C Becker and L Wharton, *Surf. Sci.* **78** (1978) 454
- <sup>32</sup>M M Martynyuk, *Sov. Phys. Tech. Phys.* **19** (1974) 793
- <sup>33</sup>M M Martynyuk, *Sov. Phys. Tech. Phys.* **21** (1976) 430
- <sup>34</sup>U Seydel and W Fuke, *J. Phys. F: Metal Phys.* **8** (1978) L157
- <sup>35</sup>F W Dabby and U C Paek, *IEEE J. Quantum Electro.* **QE-8** (1972) 106
- <sup>36</sup>Richard F Huglund Jr., *Appl. Surf. Sci.* **96-98** (1996) 1
- <sup>37</sup>J N Leboeuf, K R Chen, J M Donato, D B Geohegan, C L Liu, A A Puretzki and R F Wood, *Appl. Surf. Sci.* **96-98** (1996) 14
- <sup>38</sup>S I Anisimov, B S Luk'yanchuk and A Luches, *Appl. Spectroscopy* **96-98** (1996) 24
- <sup>39</sup>N Seifert, G Betz and W Husinsky *Appl. Surf. Sci.* **96-98** (1996) 33
- <sup>40</sup>K R Chen, J N Leboeuf, R F Wood, D G Geohegan, J M Donatto, C L Liu and A A Puretzky, *Appl. Surf. Sci.* **96-98** (1996) 45
- <sup>41</sup>C R Phipps Jr., T P Turner, R F Harrison, G W York, W Z Osborne, G K Anderson, X F Corlis, L C Haynes, H S Steels, K C Spicochi and T R King, *J. Appl. Phys.* **64** (1988) 1083
- <sup>42</sup>G Granse, S Vollmer, A Lenk, A Rupp and K Rohr, *Appl. Surf. Sci.* **96-98** (1996) 97
- <sup>43</sup>X L Mao, WT Chen, M Caetano, MA Shannon and R E Russo, *Appl.Surf.Sci.* **96-98** (1996) 126
- <sup>44</sup>G J Pert, *J Plasma Phys.* **35** (1986) 43

- <sup>45</sup>G J Pert, *J Plasma Phys.* **36** (1986) 415
- <sup>46</sup>G J Pert, *J Plasma Phys.* **39** (1988) 241
- <sup>47</sup>G J Pert, *J Plasma Phys.* **49** (1993) 295
- <sup>48</sup>J H Bechtel, *J. Appl. Phys.* **46** (1975) 1585
- <sup>49</sup>E G Gamaly *Laser & Particle beams* **12** (1994) 185
- <sup>50</sup>K H Song, X Xu, *Appl. Phys. A* **65** (1997) 477
- <sup>51</sup>J C Miller and D B Geohegan (Eds.) *Laser Ablation: Mechanisms and Applications – II*  
American Institute of Physics, New York (1994)
- <sup>52</sup>J C S Kools in *Pulsed laser deposition of thin films* by D B Chrisey & G K Hubler (Eds.) John  
Wiley & Sons, New York, (1994) p.455
- <sup>53</sup>R E Russo, R P Reade, J M McMillan and B L Olsen, *J.Appl.Phys.* **68** (1990) 1354
- <sup>54</sup>D B Geohegan, *Thin Solid Films* **220** (1992) 138
- <sup>55</sup>J Gonzalo, C N Afonso, F Vega, D Martinez Garcia and J Perriere, *Appl.Surf.Sci.* **86** (1995) 40
- <sup>56</sup>T Venkatesan, X D Wu, A Inam, Y Jeon, M Croft, E W Chase, C C Chang, J B Watchman, R  
W Odom, F R di Brozolo and C A Magee, *Appl.Phys.Lett.* **53** (1988) 1431
- <sup>57</sup>K L Saegner in *Pulsed laser deposition of thin films* by D B Chrisey & G K Hubler (Eds.)  
John Wiley & Sons, New York, (1994) p.199
- <sup>58</sup>I Weaver and C L S Lewis, *J.Appl.Phys.* **79** (1996) 7216
- <sup>59</sup>P E Dyer, *Appl. Phys. Lett.* **55** (1989) 1630
- <sup>60</sup>B N Chichkov, C Momma, S Nolte, F. von Alvensleben and A Tunnermann, *Appl. Phys. A* **63**  
(1996) 109
- <sup>61</sup>H E Elsayed Ali, T B Norris, M Pessot and G A Mourou, *Phys. Rev. Lett.* **58** (1987) 1212
- <sup>62</sup>G L Eesley, *Phys. Rev. B.* **33** (1986) 2144
- <sup>63</sup>G L Eesley, *Phys. Rev. Lett.* **51** (1983) 2140
- <sup>64</sup>X Y Wang, D M Riffe, Y S Lee and M C Downer, *Phys. Rev. B* **50** (1994) 8016
- <sup>65</sup>C. Momma, B.N. Chichkov, S. Nolte, F Von Alvensleben, A. Tunnermann, H. Welhing and  
Wellegehausen, *Opt. Comm* **129** (1996) 134

- <sup>66</sup>P E Dyer, S R Farrer and P H Key, *Appl. Surf. Sci.* **54** (1992) 255
- <sup>67</sup>P E Dyer, S R Farrer and P H Key, *Appl. Phys. Lett.* **60** (1992) 1890
- <sup>68</sup>See for example L C Chen in *Pulsed laser deposition of thin films* by D B Chrisey and G K Hubler (Eds.) John Willy & Sons (1994) and references cited therein
- <sup>69</sup>R W Dreyfus, C Phipps and A Vertes in *Laser ablation: Mechanisms and Applications II* by J C Miller and D G Geohegan (Eds.), American Institute of Physics, New York (1993) p.285
- <sup>70</sup>R E Russo, *Appl. Spectroscopy* **49** (1995) 14A
- <sup>71</sup>F P Gaghano and U C Paek *Appl. Opt.* **13** (1974) 274
- <sup>72</sup>D Bauerle, *Laser processing and Chemistry*, Springer (1996) p.533
- <sup>73</sup>J C S Kools, T S Baller, S T DeZwart and J Dielman, *J. Appl. Phys.* **71** (1992) 4547
- <sup>74</sup>S I Anisimov, R S Luk'yanchuk and A Luches, *Appl. Surf. Sci.* **96-98** (1996) 24
- <sup>75</sup>R.W.Dreyfus, R.Kelly and R.E. Walkup, *Nucl. Instr. Meth. Phys. Res. B* **23** (1987) 557
- <sup>76</sup>J.B. Anderson, *Molecular Beams and Low Density Gas Dynamics* by P.P.Wegener (Ed.) Marvel Decker, NY (1974)
- <sup>77</sup>I Noor Butcha, R R Luches and Y Zeiri, *J. Chem. Phys.* **86** (1987) 5916
- <sup>78</sup>R Kelly and R W Dreyfus, *Suf. Sci.* **198** (1988) 263
- <sup>79</sup>S I Anisimov, *Sov. Phys. JETP* **27** (1968) 182
- <sup>80</sup>J B Anderson and J B Fenn, *Phy. Fluids* **8** (1965) 780
- <sup>81</sup>Riju C Issac, K Vasudhevan Pillai S S Harilal, Geetha K Varier, C V Bindhu, Pramod Gopinath, P Radhakrishnan, V P N Nampoore and C P G Vallabhan, *Appl. Surf. Sci.* **125** (1998) 227
- <sup>82</sup>R Kelly and R W Dreyfus, *Nucl. Instr. Meth. Phys. Res. B* **32** (1988) 341
- <sup>83</sup>J F Ready, *Effect of High Power Laser Radiation* 1971 p.67
- <sup>84</sup>X L Mao and R E Russo, *Appl. Phys. A* **64** (1997) 1
- <sup>85</sup>Riju C Issac, Geetha K Varier, Pramod Gopinath, S S Harilal, V P N Nampoore and C P G Vallabhan *Appl. Phys. A*, in press (1998)
- <sup>86</sup>S I Anisimov, D Bauerle and B S Lukyanchuk, *Phys. Rev. B* **48** (1993) 12076
- <sup>87</sup>R L McCroy and J H Sources in *Laser Induced Plasmas and Applications* by L J Redziemski

and D A Cremers (Eds.) (Marcel Dekker, New York 1989) p.228

<sup>88</sup>S Elizer S and A Ludmirsky, *Laser and Particle beams* **1** (1983) 251

<sup>89</sup>H Hora P Lalousis and S Eliezer, *Phys Rev. Lett* **53** (1984)1650

<sup>90</sup>S Elizer & H Hora, *Phys. Rep.* **172** (1989) 339

<sup>91</sup>Jose G *Theoretical Physics*, Hafher Publishing Co. New York (1959) P. 273

<sup>92</sup>S S Harilal, Riju C Issac, C V Bindhu, V P N Namoopri and C P G Vallabhan, *J. Appl. Phys.* **80** (1996) 3561

<sup>93</sup>S S Harilal, Riju C Issac, C V Bindhu, V P N Namoopri and C P G Vallabhan, *J. Appl. Phys.* **81** (1997) 3637

<sup>94</sup>D B Geohegan, *Appl. Phys. Lett.* **60** (1992) 2732

<sup>95</sup>S S Harilal, C V Bindhu, V P N Namoopri and C P G Vallabhan, *Appl.Phys.Lett.* **72** (1998) 167

<sup>96</sup>V Kumar and R K Thareja, *J Appl. Phys.* **67** (1990) 3260

<sup>97</sup>Y I Lee, K Song, H K Cha, JM Lee, M C Park, G H Lee and J Sneddon, *Appl. Spectroscopy* **51** (1997) 959

<sup>98</sup>A F Golovin, SS Lemtsov, and B T Fedyushin, *Sov. J. Quantum Electron* **21** (1991) 1359

<sup>99</sup>Abhilasha, P S R Prasad and R K Tharaja, *Phys Rev E* **48** (1993) 2929

<sup>100</sup>Z Paszti, Z E Horvath, G Peto, A Karacs and L. Guzzi, *Appl. Surf. Sci* **109/110** (1997) 67

<sup>101</sup>Riju C Issac, K Vasudevan Pillai, S S Harilal, Geetha K. Varier, CV Bindhu, Pramod Gopinath, P Radhakrishnan, VPN Nampoore and CPG Vallabhan, *ApplSurf.Sci.* **125** (1998) 227

<sup>102</sup>X Y Chen, S B Xiong, Z S Sha, Z G Liu, *Appl. Surf. Sci.* **115** (1997) 279

<sup>103</sup>D B Koopman, *Phys. Fluids* **15** (1997) 1959

<sup>104</sup>B Y Man, X T Wang and G T Wang, *Appl. Spectroscopy* **51** (1997) 1910

<sup>105</sup>D. A Freiwald, *J. Appl. Phys.* **43** (1972) 2224

<sup>106</sup>J I Bobin, Y A Durand, Ph. P Langer and G Tonon, *J. Appl. Phys.* **39** (1968) 4184

<sup>107</sup>WKA Kumudini, Y Nakayama, Y Nakata, T Okada and M Maeda, *J.Appl.Phys* **74** (1993) 7510

<sup>108</sup>S J Lee, K Imen, and SD Allen, *J. Appl. Phys.* (1993) 7044

<sup>109</sup>Y B Zeldovich and Yu P Raizer in *Physics of Shock Waves and High Temperautre*

- Hydrodynamic Phenomena* by W D Hayes and R F Probst (Eds.) Academic Press, London 1966 p.93
- <sup>110</sup>X Y Chen, S B Xcong, Z S Sha, Z G Lin, *Appl. Surf. Sci.* **115** (1997) 279
- <sup>111</sup>S S Harilal, Riju C Issac, C V Bindhu, Pramod Gopinath, V P N Nampoore and C P G Vallabhan, *Spectrochimica Acta A* **53** (1997) 1527
- <sup>112</sup>G Hatem, C Colon, J E Campos, *Spectrochimica Acta* **49A** (1993) 509
- <sup>113</sup>Srinivasan R, B Braren and K G Casey, *J. Appl. Phys.* **68** (1990) 1842
- <sup>114</sup>Srinivasan R, K G Casey, B BrarenIn and M Yeh, *J. Appl. Phys.* **67** (1990) 1604
- <sup>115</sup>Grun J, J Stamper, C Manka, J Resnick, R Burris and BH Ripin, *Appl. Phys. Lett.* **59** (1991) 246
- <sup>116</sup>Proyer S and E Stangl, *Appl. Phys. A* **60** (1995) 573
- <sup>117</sup>Grad L and J Mozina, *Appl. Surf. Sci.* **69** (1993) 370
- <sup>118</sup>P L Ventzek, R M Gilgembach, D M Heffelfinger and J A Sell, *J. Appl. Phys.* **70** (1991) 587
- <sup>119</sup>Ediger M N and G H Petit, *J. Appl. Phys.* **71** (1992) 3510
- <sup>120</sup>R W Dreyfus, *Appl. Surf. Sci.* **86** (1995) 29
- <sup>121</sup>L D Landau and E M Lifshitz, *Fluid dynamics* (Pergamon, Oxford 1974)
- <sup>122</sup>J Hermann, C Boulmer-Leborgne and D Hong, *J. Appl. Phys* **83** (1998) 691
- <sup>123</sup>Z Szymanski, J Kurzyna and W Kalita, *J. Phys. D: Appl. Phys.* **30** (1997) 3153
- <sup>124</sup>C Aragon and J A Aguilera, R W P McWhirter *J. Phys. B* **1** (1968) 1180
- <sup>125</sup>B C Boland, F E Irons and R W P Mc Whirter *J. Phys. B* **1** (1968) 1180
- <sup>126</sup>J Lague, W Juchmann, E A Brinkmann and J B Jeffris, *J. Vac. Sci. Technol.* **A16** (1998) 397
- <sup>127</sup>A H El-Astal and T Morrow, *J. Appl. Phys.* **80** (1996) 1156
- <sup>128</sup>L Zhang, S Han, Z Xu, Z Zhang, P Fan and Lan Sun, *Phys. Rev. E* **51** (1995) 6059
- <sup>129</sup>R Tambay, R Singh and R K Tareja, *J. Appl. Phys.* **72** (1992) 1197
- <sup>130</sup>P J Wolf, *J. Appl. Phys* **72** (1992) 1280
- <sup>131</sup>F Fuso, L N Vyacheslavov, G Masciarelli and E Arimondo, *J. Appl. Phys.* **76** (1994) 8088
- <sup>132</sup>H R Griem *Plasma Spectroscopy* (Mc.Graw Hill, New York, 1964)
- <sup>133</sup>H R Griem *Spectral Line Broadening by Laser Plasmas*, Academic Press, New York (1974)

- <sup>134</sup>D B Geohegan in *Pulsed laser deposition of thin films* by D B Chrisey and G K Hubler (Eds.), John Wiley & Sons (1994) p. 138
- <sup>135</sup>C C Smith and N J Peacock, *J. of Phys. B: At. Mol. Phys.* **11** (1978) 2749
- <sup>136</sup>V A Boiko, S A Pikuz and A Ya Faenov, *J. Phys. B: At. Mol. Phys.* **12** (1979) 1889
- <sup>137</sup>G Mehlman, D B Chrisey, P G Burkhalter, J S Horwitz and D A Newmann, *J. Appl. Phys.* **74** (1994) 53
- <sup>138</sup>J F Kielkopf, *Phys. Rev. E* **52** (1995) 2013
- <sup>139</sup>D A Haynes Jr., D T Garber, C F Hooper Jr., R C Mancini, Y T Lee, D K Bradley, J Delettrez, R Epstein and P A Jaanimagi, *Phys. Rev. E* **53** (1996) 1042
- <sup>140</sup>O Renner, P Sondhauss, D Salzmann, A Djaouis, M Koenig and E Foster, *J. Quant. Spectr. Radiat. Transfer* **58** (1997) 851
- <sup>141</sup>O Renner, D Salzmann, P Sondhauss, A Djaouis, E Krousky and E Foster, *J. Phys. B: At. Mol. Opt. Phys.* **31** (1998) 1379
- <sup>142</sup>C B Leborgne, J Hermann and B Duhreuil, *Appl. Phys. A* **55** (1992) 340
- <sup>143</sup>S S Harilal, C V Bindhu, Riju C Issac, V P N Nampoore and C P G Vallabhan, *J. Appl. Phys.* **82** (1997) 2140
- <sup>144</sup>George Bekefi *Principles of laser plasmas* (John Wiley & Sons, 1976) p. 590
- <sup>145</sup>R W P Mc Whirter (1965) in *Plasma diagnostic techniques* by R H Huddleston and S L Leonard (Eds.), Academic Press, New York]
- <sup>146</sup>H R Griem, *Plasma spectroscopy* (Mc Graw Hill New York 1964) p.148
- <sup>147</sup>Kiichiro Kagawa, Mineo Ohtani, Sadahiro Yoki and Sadao Nakajima, *Spectrochimica Acta* **39B** (1984) 525
- <sup>148</sup>Martha R Joseph, Ning Xu and Vahid Majidi, *Spectrochimica Acta* **49B** (1994) p.89
- <sup>149</sup>CM Davies, HH Telle, DJ Montgomery and RE Corbett, *Spectrochim. Acta B* **50** (1995) 1059
- <sup>150</sup>J Hermann, A J Thomann, C Boulmer-Leborgne and B Dubreuil, *J. Appl. Phys.* **77** (1995) 2928
- <sup>151</sup>H C Lee, R W Dreyfus, W Marine, M Sentis and I A Movtcha, *Appl. Surf. Sci.* **96-98** (1996) 164
- <sup>152</sup>J Hermann, C Boulmer-Leborgne and D Hong, *J. Appl. Phys.* **83** (1998) 691
- <sup>153</sup>X L Mao, M A Shannon, A J Fernandez and R E Russo, *Appl. Spectroscopy* **49** (1995) 1054

- <sup>154</sup>C C Popovics, P Renaudin, O Rancu, F Gilleron, J C Ganthier, O Larroche, O Peyrusse, M Dirksmoller, P Sondhauss, T Missala, I Uschmann, E Foster, O Renner and E Kronsky, *Phys. Plasmas* **4** (1997) 190
- <sup>155</sup>D Lacroix, G Jeandel and C Boudot, *J. Appl. Phys.* **81** (1997) 6599
- <sup>156</sup>Z Andreic, V Henc-Bartolic and H J Kunze, *Physica Scripta* **47** (1993) 405
- <sup>157</sup>X T Wang, B Y Man, G T Wang, Z Zhao, Y Liao, B Z Xu, Y Y Xia, L M Mei and X Y Hu, *J. Appl. Phys.* **80** (1996) 1783
- <sup>158</sup>S M Cameroon, M D Tracy and J F Camacho, *IEEE Trans. Plasma Science* **24** (1996) 45
- <sup>159</sup>R E Walkup, J M Jasinski and R W Dreyfus, *Appl. Phys. Lett.* **48** (1986) 1690
- <sup>160</sup>C D David Jr., *Appl. Phys. Lett* **11** (1967) 394
- <sup>161</sup>I Usru, M Sioica, I N Mihailescu and D Craciun, *Infrared Phys.* **29** (1989) 9
- <sup>162</sup>T Mochizuki, K Hirata, H Ninomiya, K Nakamura, K Maeda, S Horiguchi and Y Fujiwara, *Opt. Commn.* **72** (1989) 30
- <sup>163</sup>Geetha K Varier, Riju C Issac, S S Harilal, C V Bindhu, V P N Nampoori and C P G Vallabhan, *Spectrochimica Acta B* **52** (1997) 657
- <sup>164</sup>D M Manos and H F Dylla in *Plasma etching: An introduction* by D M Manos and D L Flamm (Eds.) (Academic Press, New York 1989) p.263
- <sup>165</sup>J M Hendron, C M O Mahony, T Morrow and W G Graham *J. Appl. Phys* **81** (1997) 2131
- <sup>166</sup>F F Chen in *Plasma diagnostic techniques* by R H Huddleston and S L Leonard (Eds.) (Academic, New York 1965)
- <sup>167</sup>M A Libermann and A J Lichtenberge *Principles of plasma discharges and material processing* (Wiley, New York 1994)



# Fabrication and Methods

## **Abstract**

The present chapter gives a description of the basic experimental setup that has been used for the analysis of the plasma. Design of the plasma chamber fabricated as part of the investigations is also illustrated.

In chapter 1, a brief description of the different experimental techniques which are being used for the diagnostics of laser produced plasma plumes is given. In the present case, we have used three different techniques *viz.* optical emission spectroscopy, Langmuir probes and Michelson interferometry for the study of laser produced plasmas from solids. In order to perform the experiments, a versatile plasma chamber is designed and fabricated which is successfully coupled to rotary and diffusion vacuum pumps to produce pressure as low as  $10^{-5}$  mbar inside the chamber.

## **2.1 Design and fabrication of the plasma chamber**

The essential constituents of the experimental setup for the laser ablation experiments is a plasma chamber which contains gas inlets, optical view ports, probe insertion ports, substrate holder for thin film deposition, provision for vacuum pumps etc. A multi purpose plasma vacuum chamber which fulfill all these requirements is fabricated as part of the investigations. The schematic of the front view of the chamber is given in figure 2.1. The chamber consists of a bottom plate, body of the chamber and a top plate. Two optical viewing ports of diameter 10 cm are introduced for emission diagnostics of the plasma. A third window which is having diameter 4 cm is used as laser inlet.

The base of the chamber is a mild steel disk plated in soft chromium having thickness 1.5 cm and diameter 35 cm. A central hole with diameter 12 cm allows the plasma chamber to be in contact with the diffusion and rotary pumps. The body of the chamber is 18cm high with three glass windows. The top plate of the chamber is a disk

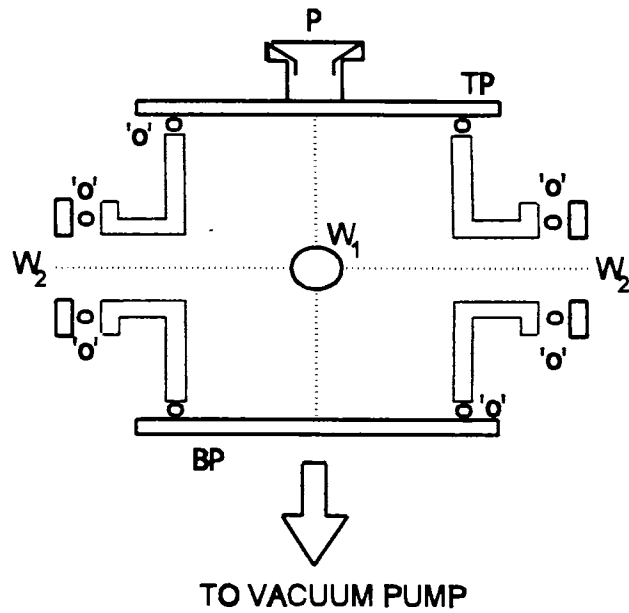


**Figure 2.1** Front view of the vacuum chamber. The three viewing ports on the body of the chamber is seen. The top plate is having provisions for the insertion of target holder.  $W_1$  Laser inlet glass window,  $W_2$  Optical monitoring windows, TP top plate, BP Bottom plate, P Target holder rod inlet, O 'O' rings.

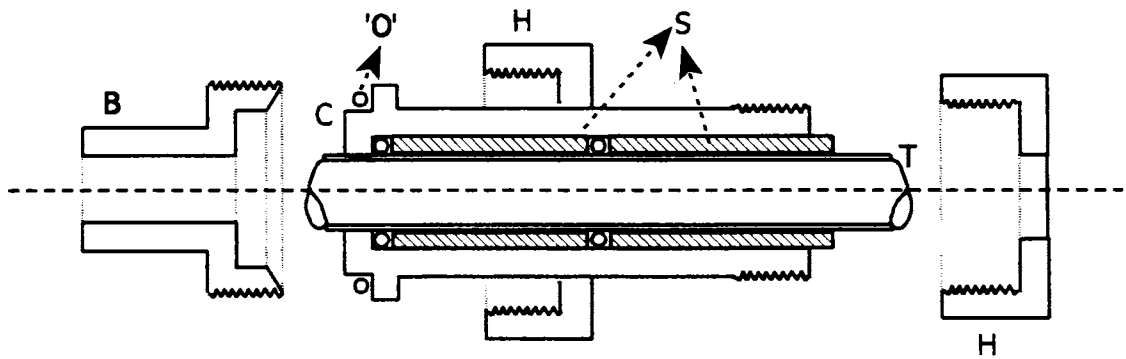


**Figure 2.2** Design of the vacuum seal used for the insertion of the substrate holder and the Langmuir probe. B Body of the chamber, C Coupling, H Holder, S Sleeves, T Hollow tube, O 'O' rings.

with thickness 1.5 cm and diameter 35 cm again made of mild steel and coated with soft chromium. Besides these the chamber has provisions for inserting Langmuir probes and holders for thin film deposition which is controlled from outside without disturbing vacuum. At  $45^{\circ}$  to the beam axis there are two rods inserted into the chamber through which holding rods for the substrate and the probes are inserted. These rods can be moved in and out, in order to vary the target- substrate or target- probe distance. This has been done with the help of a vacuum seal, the schematic of which is shown in the figure 2.2. When the holder H in figure 2.2 is tightened, the sleeves S will move inwards thereby causing lateral expansion of the 'O' rings. Then the 'O' rings will hold tightly the hollow tube T. Therefore the tube can be moved in or out without disturbing vacuum.

## 2.2 Description of the experimental setup for time of flight studies

The optical emission from different species inside the plasma plume gives vital information regarding the time of flight (TOF) profiles of various species inside the plasma.<sup>1-5</sup> The experimental configuration adopted for spectral as well as Langmuir probe measurements is schematically shown in figure 2.3. The plasma is produced using a Q-switched Nd:YAG laser (Quanta Ray DCR II) operated at the fundamental wavelength of 1064 nm with pulse width (FWHM) 9 ns and repetition frequency 10 Hz. The target used are discs of diameter 1.5 cm and thickness 2-3 mm approximately, which is kept inside the plasma chamber. The targets were rotated about an axis parallel to the laser beam and frequently translated during irradiation in order to avoid multiple hits at the same location for long time. Multiple hits at the same location will cause pitting of the target, thereby causing change in laser spot size and hence change in intensity at the focal spot. A convex lens of focal length 30 cm focuses the laser beam to the target (spot radius 50  $\mu\text{m}$ ). Laser beam hits the target surface at an angle of  $45^{\circ}$  for film deposition and at  $90^{\circ}$  during spectral measurements. In most of the cases, the experiment is

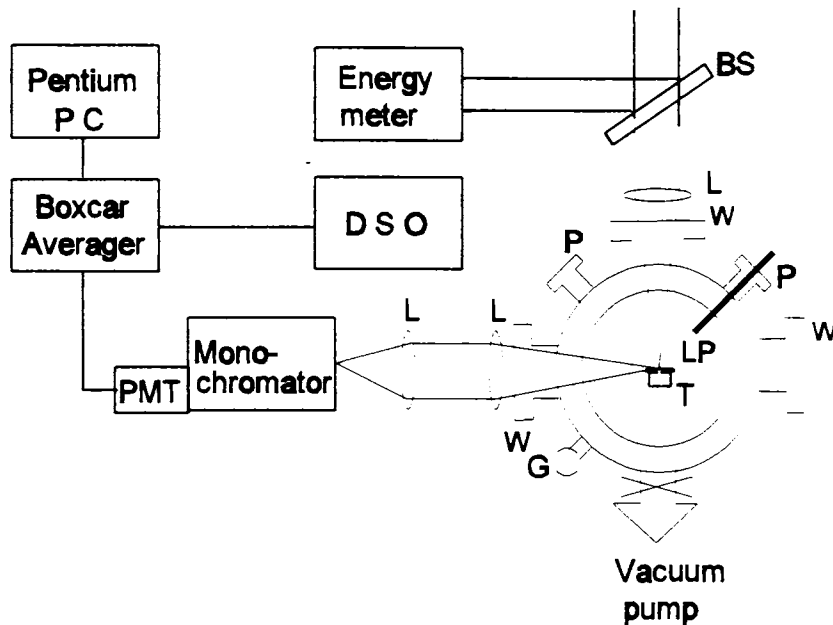


**Figure 2.3** Schematic diagram of the experimental setup used for spectral as well as Langmuir probe measurements. P M T: Photomultiplier tube, P C: Personal computer, D S O: Digital storage oscilloscope, T: Target holder and rotator, G: Vacuum measuring gauge, LP: Langmuir probe, P: Probe insertion ports, L: Lens, W: Optical viewing ports

performed inside the chamber and in some circumstances when the experiment is done at atmospheric pressure, the experiment is performed outside the plasma chamber.

The chamber is connected to diffusion and rotary vacuum pumps and an ultimate pressure of  $10^{-5}$  mbar is obtainable inside the chamber. The chamber also has glass windows for optical monitoring and have provisions for thin film substrate holders. The time of flight (TOF) measurements were performed after one-to-one imaging of the luminous plasma plume on to the entrance slit of a monochromator by appropriate collimating and focusing lenses. The optical emission is viewed normal to the expansion direction of the plume. Using proper slits and apertures any vertical

segment of the plasma situated at definite distances from the target surface can be selected for analysis. The wavelength selection was done by a high resolution spectrometer (SPEX Model 1704, 1 m, grating with 1200 grooves per mm blazed at 500 nm and slit width limited resolution 0.015 nm ). A thermoelectrically cooled photomultiplier tube (Thorn EMI, KQB-9863, rise time 2 ns) was used as the photodetector at the exit slit of the monochromator. The TOF signals are monitored on a digital storage oscilloscope (200 MHz, Iwatsu DS 8621) having input impedance of 50 ohms. While charting the spectrum, a boxcar averager is used for averaging and time-gating the signals. Usually intensities from 10 successive pulses were averaged to get a good signal to noise ratio. For spatially resolved studies, different regions of the plasma plume are focused on to the monochromator slit. Hence the present setup is suitable for both space and time resolved spectral measurements. The complete emission spectrum in the range 350-700 nm is analyzed with the above setup. During electron density measurements using the stark broadened profiles of emission lines, the same setup is used with minimum monochromator slit widths for better resolution. The time-of-flight signals of ions and electrons are sometimes measured using Langmuir probes and the probe insertion ports are also shown in the figure. The probe power supply and other details are given in section 2.4. The laser pulse energy is measured with a calibrated laser energy meter (Delta Developments) and the power density at the focal spot is calculated after reflection corrections from the lens and window surfaces.

Plate 1 gives the photograph of the actual experimental setup. The various instruments are marked in the figure and illustrated in the caption. Plates 2 and 3 are the photographs of the laser ablated plumes from  $\text{YBa}_2\text{Cu}_3\text{O}_7$  and silver respectively at a chamber pressure 0.16 mbar. The figure shows that the plumes are very luminous objects the color of which depends on the constituents of the plasma. There exists definite boundaries between the plume and the ambient gas.



**Plate 1** Photograph of the experimental setup



**Plate 2** Photograph of the laser produced plasma from  $\text{YBa}_2\text{Cu}_3\text{O}_7$  at a chamber pressure of 0.16 mbar

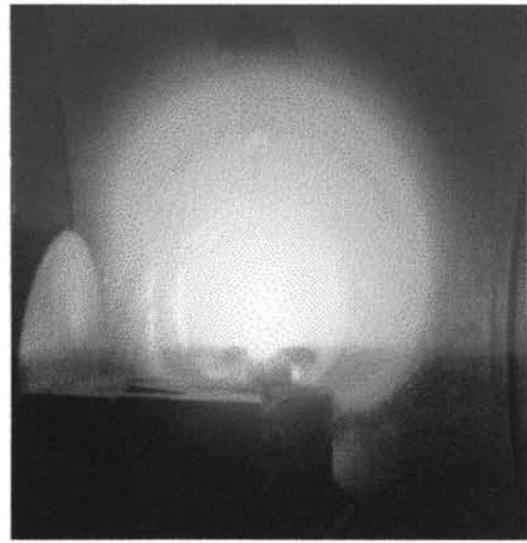


**Plate 2** Photograph of the laser produced plasma from Silver at a chamber pressure of 0.16 mbar

## 2.3 Instrumental specifications

The specifications of various instruments that have been used in the present measurements are given below:

### 1. Nd:YAG Laser<sup>6</sup>

Model & Make	: Quanta Ray (Spectra Physics), DCR 11, Pulsed Nd:YAG laser
Wavelength	: 1064 nm
Pulse energy	: 275 mJ (Maximum)
Pulse width (FWHM)	: 9 ns $\pm$ 0.5 ns
Pulse repetition frequency	: 10 Hz, 1-14 Hz range
Spatial mode	: Diffraction coupled, uniphase, nearly diffraction limited, 6.4 mm diameter
Line width	: <0.0011 nm
Linear polarization	: > 98%

### 2. Monochromator<sup>7</sup>

Model & Make	: SPEX 1704
Grating	: 1 meter focal length, 1200 grooves/mm Blazed at 500 nm
Resolution	: 0.01 nm for slit width 10 $\mu$ m & height 2mm, spectral band pass 0.08 nm
Detector	: Thermoelectrically cooled (-50 °C) photon counting PMT, KQB 9863 (Thorn EMI), 2 ns rise time

Wavelength scanning : Using microprocessor controlled CD2A compudrive arrangement. Minimum scan speed 0.0001-1 nm/sec. Minimum step resolution 0.00025 nm. Scan mode can be selected either continuous or burst. In most of the experimental results presented here the continuous mode scanning is selected.

### 3. Boxcar averager<sup>8</sup>

Model & Make : SR 250, Stanford Research Systems

Sensitivity : Volt out/volt in may be set from 1V/1V to 1V/5mV

Filter : An input filter allows coupling of DC, AC above 10Hz and AC above 10 KHz

Signal input : 1 M $\Omega$  input impedance,  $\pm$  2V DC usable range, protected to 100V DC. External 50 $\Omega$  termination is made during measurements for better time response

Averaging : An exponential moving average may be taken over 1,3,10,30 ... to 10000 samples

Average output :  $\pm$  10V DC full scale with output impedance less than 1 $\Omega$  and a 1mA drive capability

Trigger : Triggered synchronously with the laser pulse

Gate delay : Variable from 1ns to 10 ms ( $\pm$  0.01 %)

Gate width : 2 ns to 15  $\mu$ s ( $\pm$  2 ns Or 20% of full scale whichever is greater)



Computer interface : The averaged output is transferred to a personal computer using the SR 245 computer interface module which provide a variety of the scanning, counting and communication functions. Data communication is made through the RS-232 serial port.

#### 4. Photodiode<sup>9</sup>

Model & Make : HP 4207, Hewlett Packard  
Response time : less than 1 ns  
Active area :  $8 \times 10^{-3} \text{ cm}^2$   
Dark current : 2.5 nA  
Noise equivalent power :  $< -108 \text{ dBm}$   
Series resistance :  $50 \Omega$   
Flux responsivity : 0.5 A/W at 770 nm  
Quantum efficiency :  $\sim 70 \%$  at 632.8 nm  
Power dissipation : 100 mW (between  $-55$  to  $125 \text{ }^\circ\text{C}$ )

#### 5. Digital Storage Oscilloscope<sup>10</sup>

Model & Make : IWATSU, DS8621, 200 MHz, 4 Channels  
Rise time : 1.7 ns  
Input impedance :  $1 \text{ M}\Omega/50 \Omega$  selectable  
Averaging : 1 to 256 pulses  
Sensitivity : 0.2 mV/div  
Interfacing : RS 232 serial port

### 2.3 Electron density from Michelson interferometry

Electron density in laser produced plasmas can be measured using Michelson Interferometry.<sup>11-14</sup> The ablated material ejected from the target surface consists of ions, atoms, and molecules in addition to free electrons. All these species may be expected to contribute to the refractive index of the plasma. Even then the contributions from the atomic or ionic species can be neglected in cases when the probe laser frequency is sufficiently far from the resonance transitions. The atomic contribution to the refractive index  $\mu_{at}$  is given by<sup>15</sup>

$$\mu_{at} = 1 + \frac{e^2}{8\pi^2 \epsilon_0 m} \sum_i \frac{N_i f_i}{(\nu_i^2 - \nu^2)} \quad (2.1)$$

where  $e$  is the electron charge,  $\epsilon_0$  is the permittivity of free space,  $m_e$  is the mass of electron,  $N_i$  is the number density of the lower level of a transition,  $f_i$  is the oscillation strength,  $\nu_i$  any resonance frequency and  $\nu$  is the frequency of light used to make the measurements. The above equation suggests that the contribution from the atomic/ionic species to the refractive index is appreciable only near the resonance transitions. The probe beam wavelength is selected in such a way that it should be sufficiently far from the resonance transitions so that the contributions from atomic or ionic species to the refractivity can be neglected.

#### 2.3.1 Evaluation of electron density

The experimental setup for electron density measurements using interferometry is as shown in figure 2.4. An intensity stabilized 4 mW He-Ne laser (Spectra Physics, Model No.102-4) is used as the light source for the construction of the Michelson interferometer. The beam in one of the arms of the Michelson interferometer passes grazing the sample surface. The shift in the fringe pattern due to the presence of the

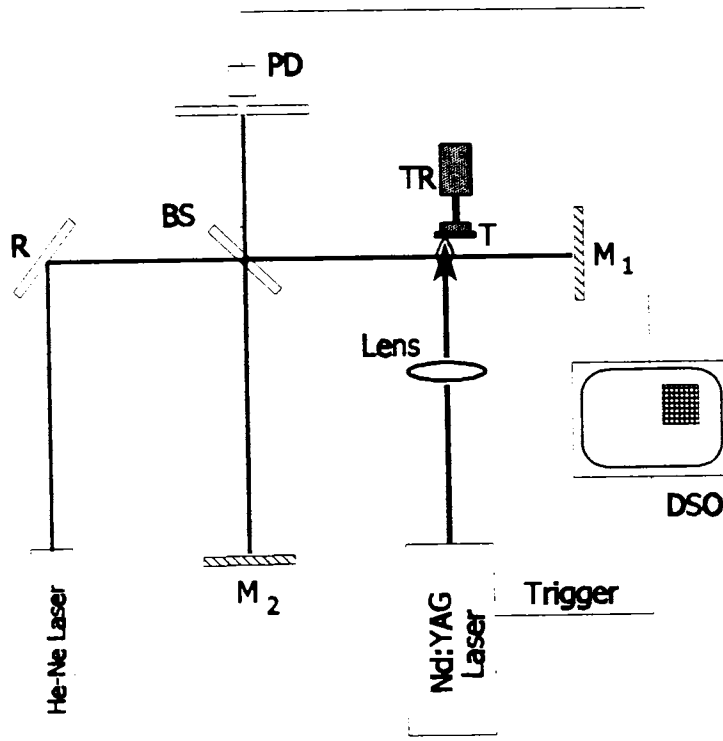


**Figure 2.4** Schematic diagram of the experimental setup used for the measurement of electron density using Michelson interferometry.  $M_1$ ,  $M_2$  Totally reflecting mirrors forming the interferometer; R Reflector; BS 50% beam splitter; PD Photodiode; TR Target rotating motor; T Target; DSO Digital storage oscilloscope.

plasma is measured as a voltage change using a fast *PIN* photo diode (HP -4207) and displayed on a 200MHz digital storage oscilloscope (Iwatsu, Model DS 8621). These voltage shifts were used to calculate the electron density of the plasma. All the measurements were done in a single pulse protocol in order to avoid the residual heating effect from the previous pulse. After a few measurements the target is rotated and translated so that fresh surface is available for ablation. High power laser radiation from a pulsed Nd:YAG (Quanta Ray DCR 11) laser at wavelength 1064 nm with pulse duration 9 ns (FWHM) is focused using a convex lens of focal length 20 cm normal to the target in order to produce the plasma. The target is placed slightly away

from the focal point of the lens and the laser spot size is  $7 \times 10^{-2}$  cm in radius which is measured from the etch pattern on a carbon film placed at the target position. The laser pulse energy is measured using a calibrated laser energy meter (Delta developments) and the power density at the focal spot is calculated after reflection correction from the lens surfaces. The pulse energy is varied during the experiment by using suitable attenuators. The experiment was performed on an indigenously built vibration isolation table.

The intensity distribution of the fringe pattern of a Michelson interferometer is given by,

$$I(t) = A^2 + B^2 + 2AB \cos[(\phi_A - \phi_B) - \gamma(t)] \quad (2.2)$$

where  $A$  and  $B$  are the amplitudes and  $\phi_A$  and  $\phi_B$  the phases of the two interfering beams respectively and  $\gamma(t)$  is the phase difference introduced due to the presence of the plasma. This derivation is made in accordance with the arguments given in Monson<sup>16</sup> et al. The shift in the fringe pattern resulting from this time dependent phase factor can be measured as voltage change in the output of the photodiode. For the intensity to be very sensitive to small changes in  $\gamma(t)$ , the operating point is chosen such that  $\phi_A - \phi_B = (m+1/2)\pi$ . Then the change in the output voltage of the photodetector  $\delta V(t)$  is,

$$\delta V(t) \propto 2AB \sin \left[ \frac{4\pi}{\lambda} \int_0^l \Delta\mu(t) dl \right] \quad (2.3)$$

where  $\lambda$  is the wavelength of the probe laser beam,  $l$  the lateral extension of the plasma and  $\Delta\mu(t)$  is the change in refractive index due to the presence of the plasma. When the phase difference  $(\phi_A - \phi_B)$  is taken through a phase change of  $\pi$ , i.e., the operating point is moved from the bright to the dark fringe center the corresponding

difference in intensities  $(I_{\max} - I_{\min})$  will be proportional to  $4AB$  in the absence of plasma. With a linear response for the photodetector, the corresponding voltage difference  $(V_{\max} - V_{\min})$  denoted by  $V$  is proportional to  $4AB$ . Therefore from eqn. (2.3),

$$\gamma(t) = \sin^{-1}\left(\frac{2\Delta V}{V}\right) \quad (2.4)$$

Assuming negligible absorption and light scattering at the probe wavelength, the index of refraction  $\mu$  of the plasma is given by<sup>17</sup>  $\mu^2 = 1 - (n_e/n_{ec})$  where  $n_e$  is the plasma electron density and  $n_{ec}$  the critical plasma electron density given by  $n_{ec} = (\omega^2 m \epsilon_0 / e^2)$  where  $\epsilon_0$  is the permittivity of free space,  $m$  the electron mass,  $e$  electron charge and  $\omega$  the angular frequency of the pump laser radiation.  $n_c$  has a typical value  $9.92 \times 10^{20} \text{ cm}^{-3}$  for the Nd:YAG laser wavelength ( $\lambda = 1064 \text{ nm}$ ). Also when the critical density  $n_e/n_{ec} \ll 1$ ,

$$\gamma(t) \cong \frac{e^2}{mc\omega\epsilon_0} \int_0^l n_e dl \quad (2.5)$$

for a path length  $l$  in the plasma. Therefore the line averaged electron density from eqn.(2.5) is,

$$\bar{n}_e \cong \frac{k\gamma(t)}{\lambda l} \quad (2.6)$$

where  $k \cong 1.778 \times 10^{12} \text{ cm}^{-1}$ . The phase factor  $\gamma(t)$  in eqn.(2.6) is experimentally found out using eqn.(2.4).

## 2.4 $T_e$ measurements using Langmuir probes

Langmuir probe is a simple instrument which contains only a piece of wire which can give valuable information regarding plasma parameters like electron density and temperature.<sup>5</sup> Probe signals also give information regarding the temporal profiles of

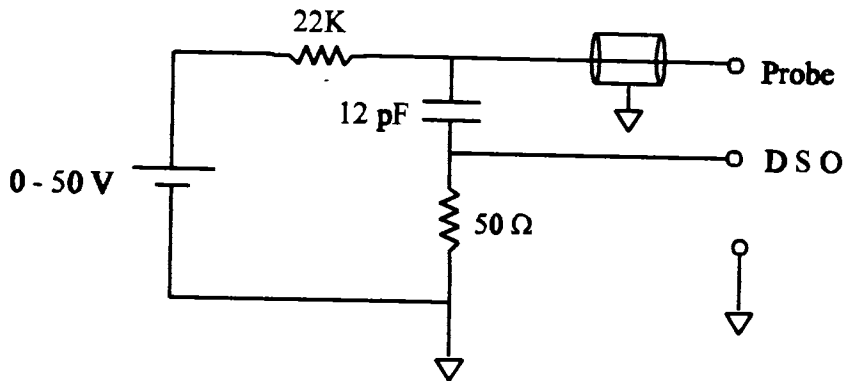


**Figure 2.5** Schematic of the probe power supply. DSO Digital Storage Oscilloscope

charged particles *viz.* electrons and ions. The probe is made up of a tungsten wire of diameter  $200\ \mu\text{m}$  and length 1 mm. The remaining length of the wire is insulated using perspex coatings. The probe is provided with external positive or negative supply depending upon the type of charges that has to be collected. The negative supply will collect positive charges and *vice versa*. The schematic of the power supply for the probe is given in Figure 2.5. The probe biasing is with respect to the ground and a 50 ohm load is provided at the input of the oscilloscope in order to have a fast time response. The time constant for the above circuit is about 600 ps. The measuring device for the probe current is a 200 MHz digital storage oscilloscope (Iwatzu DS 8621) which has a rise time of 1.7 ns. Therefore time resolutions of the order of a nanosecond is achieved with the present setup which is essential in the case of measurements of electron temporal profiles described in Chapter 4. In that case time resolved temperature measurements were performed.

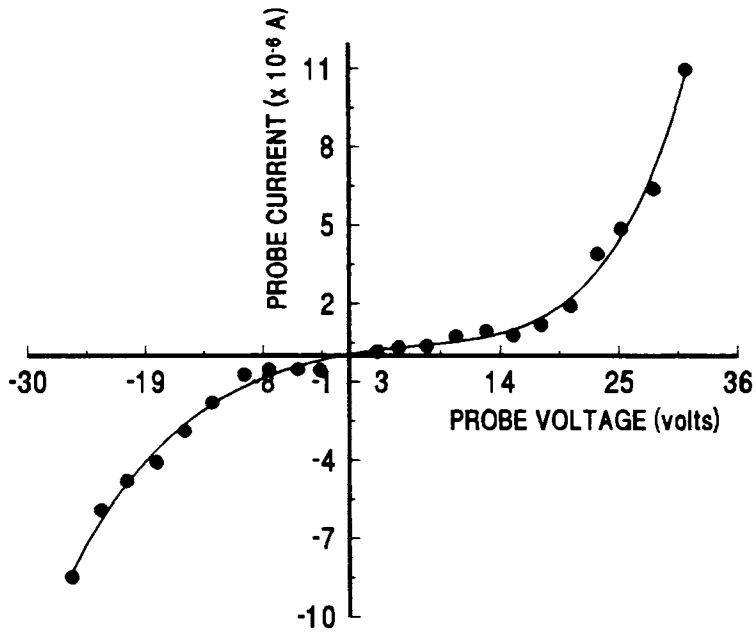


**Figure 2.6** Volt-ampere characteristics of the Langmuir probe showing the variation of both the electron current and the ion current with applied probe voltage.

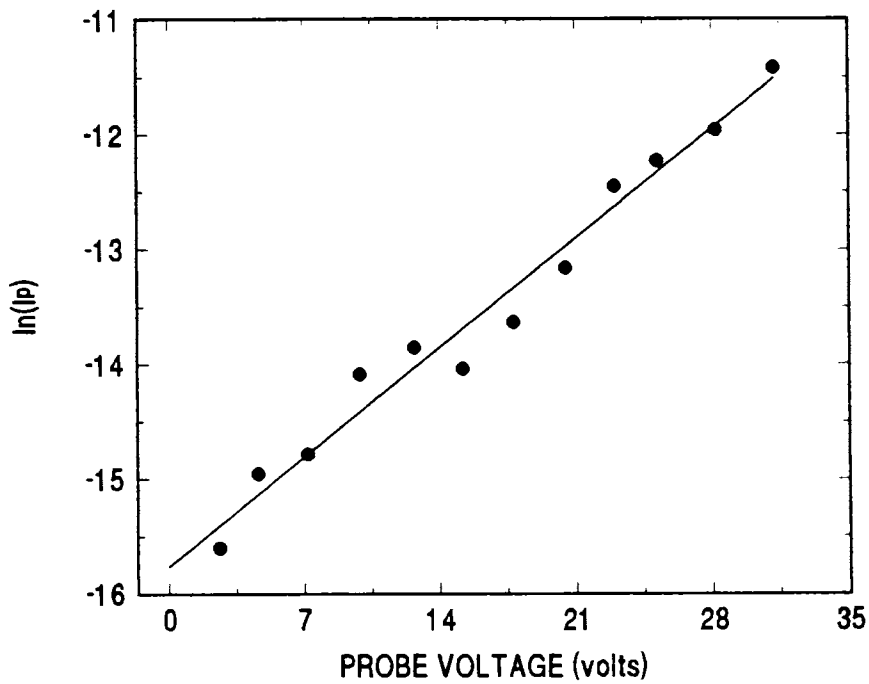


**Figure 2.7** Plot showing the linearity of the curve between  $\ln(I_p)$  and  $V_p$ . The slope of the line is given by  $(-e/k_B T_e)$

Electron temperature of the plasma is measured from the volt-ampere (V-I) characteristic of the Langmuir probe. A detailed description of the typical V-I characteristics of a probe is given in Chapter 1. Figure 2.6 gives the V-I characteristics of the Langmuir probe that has been used in the present measurements at a distance 0.6 cm from the target surface. The electron temperature is obtained from the plot between  $\ln(I)$  and the applied probe voltage  $V_p$  which is shown in figure 2.7. The plot gives a straight line with slope  $(e/k_B T_e)$ , the reciprocal of which gives the electron temperature.

### References

- <sup>1</sup>V Kumar and R K Thareja, J. Appl. Phys. **64** (1988) 5269
- <sup>2</sup>D B Geohegan, Thin Solid Films **220** (1992) 138
- <sup>3</sup>S S Harilal, C V Bindhu, Riju C Issac, V P N Nampoore and C P G Vallaban, J. Appl. Phys. **82** (1997) 2140
- <sup>4</sup>D H Lowndes, D B Geohegan, A A Puretzky, D P Norton and C M Rouleau, Science **273** (1996) 898
- <sup>5</sup> D B Geohegan in D B Chrisey and G K Hubler, (Ed.) (1994) *Pulsed laser deposition of thin films* John Wiley & Sons Inc., New York, p.115
- <sup>6</sup>Instruction Manual, Quanta Ray DCR 11 Pulsed Nd:YAG Laser, Spectra Physics, Germany
- <sup>7</sup>Operation and Maintenance instructions, 1704 SPEX Industries, New Jercey, USA
- <sup>8</sup>Operation Manual, Fast Gated Integrators and Boxcar Averagers, Stanford Research Systems, California, USA
- <sup>9</sup> Optoelectronics designers' Catalogue, Hewlett Packard (1981) p.332
- <sup>10</sup>Operation Manual, Digital Storage Oscilloscope DS8621, Iwatzu, Japan
- <sup>11</sup>R E Walkup, J M Jasinskii and R W Dreyfus, Appl. Phys. Lett. **48** (1986) 1690
- <sup>12</sup>Geetha K Varier, Riju C Issac, S S Harilal, C V Bindhu, V P N Nampoore and C P G Vallabhan, Spectrochimica Acta B **52** (1997) 657
- <sup>13</sup> Geetha K Varier, S S Harilal, C V Bindhu, Riju C Issac, V P N Nampoore and C P G Vallabhan, Mod. Phys. Lett. **10** (1996) 235
- <sup>14</sup>I V Lisitsyn, S Kohno, T Kawauchi, T Saeda, S Katsuki and H Akiyama *Jap. J. Appl. Phys.* **36** (1997) 6986
- <sup>15</sup>A P Thorne *Spectrophysics* Chapman and Hall (1974) p.380.
- <sup>16</sup>B Monson, Reeta Vyas and R Gupta *Appl. Opt.* **28** (1989) 2554
- <sup>17</sup>L Spitzer *Physics of fully ionized gases*, Interscience, NewYork (1956)



# Space resolved atomic and ionic dynamics in laser produced silver plasma

### **Abstract**

Optical emission spectroscopy and Langmuir probes are used to carry out time-of-flight analysis of atomic and ionic particles respectively. Time-of-flight profiles as a function of pressure is analyzed. Steepening of the ion density is observed at the plasma boundary which gives rise to the formation of a charged double layer and hence the velocity enhancement for the ions.

Many types of species are present within the ablated plume such as atoms, ions, molecules, clusters and free electrons. One may relate the various properties of these species with the quality of films.<sup>1</sup> The most important parameters which influence the film properties are the pressure, species energy, plasma temperature and angular distributions of the ablated species. Optical emission diagnostics is a relatively simple method and give *in situ* information on the species wise dynamics in the plasma. It is commonly employed for time-of-flight (TOF) measurements on the laser-ablated plumes and for the measurement of electron temperature and density of the laser-plasma. Langmuir probes are used to collect charged species in laser-plasmas in order to study their velocity distributions and temperature. Moreover laser ablation of materials is instrumental in producing highly ionized hydrogen-like and helium-like ions.<sup>2-4</sup>

The complex phenomena like laser-plasma interactions<sup>5</sup>, cluster formation and dissociation,<sup>6-8</sup> gas-phase chemical reactions,<sup>9,10</sup> plasma ionization,<sup>11</sup> gas dynamics<sup>12,13</sup> etc. obscure a complete understanding of the evolution and dynamics of laser-produced plasma plumes. In spite of all the primary and secondary mechanisms,

laser ablation of solids has been the subject of extensive research in recent times. Basic mechanisms of laser-ablation varies widely with the mechanical, thermal and absorptive properties of the material as well as with the laser parameters and ambient conditions.<sup>14,15</sup> There are a number of research articles describing the dynamics of the plasma plume with respect to ambient pressure, laser power density, laser wavelength<sup>16-20</sup> etc. Despite the extensive theoretical and experimental investigations carried out till date, the laser beam interaction with material, the evolution of the plasma, the gas phase dynamics and the conditions for congruent material transfer towards the substrate are not fully known. The presence of an ambient gas, for example, alters the properties of the plume significantly.<sup>21,22</sup> At high ambient pressure the plasma plume has a large angular spread due to scattering but in vacuum this scattering is negligible and the plume becomes more forward directed. Geohegan and Purezky<sup>23</sup> describes the broadening of the TOF profile in yttrium plasma at high pressure levels due to collisions with the background gas molecules. In vacuum, they found a narrow velocity profile for ionic species. Their observations have also revealed a fast and a slow component at high ambient pressure while only the fast component persists in vacuum. The slower component actually emerge due to the slowing down of the plume by collisions with ambient gas molecules. In that case such double peak structure appears only for limited distances and pressures.

Gas phase collisions inside the plasma play a major role in determining the spatial, temporal and angular distribution of ablated species as has been described in chapter 1. When the particle densities are high enough, collisions induce the formation of a thermalization layer called Knudsen layer (KL) within a few mean free paths from the target surface. Investigations on the formation of such a layer in laser-produced plasma plumes have been done by Kelly and others.<sup>24-29</sup> The formation of the KL results in stopped or backward moving material close to the target and strongly forward peaked velocity distributions away from the target. The *half range* Maxwellian velocity distribution is changed over to a *full range* Maxwellian distribution revealing the presence of backward moving particles. The KL formation is followed by a more forward peaked particle flux with an unsteady adiabatic expansion (UAE) of the plasma.

In this chapter some aspects of the dynamics of laser-ablated silver plasma in an argon ambient is studied. Argon is chosen as ambient gas since the presence of the inert ambient will reduce the possibility of gas-phase reactions and formation of molecules. The laser-plasma from silver becomes a favorite choice because of its monocomponent nature which is suited for studying laser-target, laser-plasma interactions and gas-phase kinetics. Pulsed laser deposited metallic silver films are used for the fabrication of good quality ohmic contacts to semiconductors as well.

The experimental configuration adopted for TOF measurements is schematically shown in Fig.2.3 (Chapter 2). The plasma is produced using a Q-switched Nd:YAG laser operated at the fundamental wavelength of  $1.064\ \mu\text{m}$  with pulse width 10 ns and repetition rate 10 Hz. Laser beam hits the target surface at an angle of  $45^\circ$  for measurements with Langmuir probes and at  $90^\circ$  during optical emission diagnostics. The detailed description of the experimental setup is given in chapter 2. A tungsten wire of diameter 200 microns, biased with negative voltage is used as an ion probe. The TOF signals were monitored on a digital storage oscilloscope. Signals from sixteen successive pulses were averaged to improve the signal-to-noise ratio before the output is stored in a PC connected to the oscilloscope.

### 3.1 Evolution of neutral silver atoms

Laser plasma is generated in vacuum at a laser power density of  $5 \times 10^{10}\ \text{W cm}^{-2}$ . Each laser pulse produces a bright luminous plasma plume in front of the target surface. Laser ablation causes particles to be ejected from the target with considerable velocities ( $\sim 10^6\ \text{cm s}^{-1}$ ) and the optical emission spectrum in the region 350–600 nm was monitored and emission lines from various atomic and ionic species were identified. Among the various emission lines, atomic lines of silver are most dominant. A few lines from singly ionized silver and argon are also present with reduced intensities. The monochromator is set at a fairly intense emission line of atomic silver (*viz.* 546.5 nm) and its intensities are monitored at various spatial distances away from the target surface. Similar measurements were performed on ions with a negatively biased Langmuir probes. The TOF profiles were investigated as a function of the background

gas pressure and distance from the target surface. The analysis of species present inside the plasma plumes yields important information on both the ablation process and the properties of films obtained by pulsed laser deposition. The TOF techniques permit one to determine the chemical nature of the ablation products as well as the energy distribution and laser-target interaction processes.

Various types of species usually observed during laser ablation are atoms, ions, clusters and certain molecules formed due to chemical reactions in the plasma. Apart from all these, there will be species produced in the ambient. Due to the presence of the various complex processes in the laser plasma such as plasma instabilities, chemical reactions, gas phase collisions and the formation of Knudsen layer, the calculations on the TOF profiles is not straight forward. In some cases the TOF profiles show multiple peaks instead of a single peak. The proper understanding of these widely varying behavior should take in to account the spatial and ambient conditions present inside the plasma chamber. For example, twin and triple peak distributions in the TOF profiles of carbon dimers in the laser produced carbon plasma have been investigated recently.<sup>7,8</sup> The comparison of various time delays show that a new peak is developed due to three body recombination at a distance away from the target. These species are formed outside the target in addition to dimers emitted directly from the target. At still higher pressure ranges, Lowndes<sup>30</sup> et al. have shown triple peak distribution in the TOF profiles of ions using Langmuir probes during laser ablation of ZnTe. A twin peak distribution in the TOF profile of silver atoms in vacuum has been investigated recently.<sup>31</sup> Beyond these, there are reports on the twin peak distribution in the TOF profiles of ions which exists only at a particular distance from the target. The appearance of the double peak depend critically on the ambient pressure and it has been reported to be due to the onset of Rayleigh Taylor instability at the plasma boundary.<sup>32</sup> In that case double peaks were observed in singly ionized species but the behavior was absent for higher ionized species. A simple ballistic behavior of particles cannot explain such observations which indicates the complex nature of the behavior of the constituents in the laser generated plasma. In an expanding laser plasma the time-of-flight distribution is described by an elliptical Maxwell-Boltzmann distribution<sup>33,34</sup> as given in Eqn. 1.19 in Chapter 1.

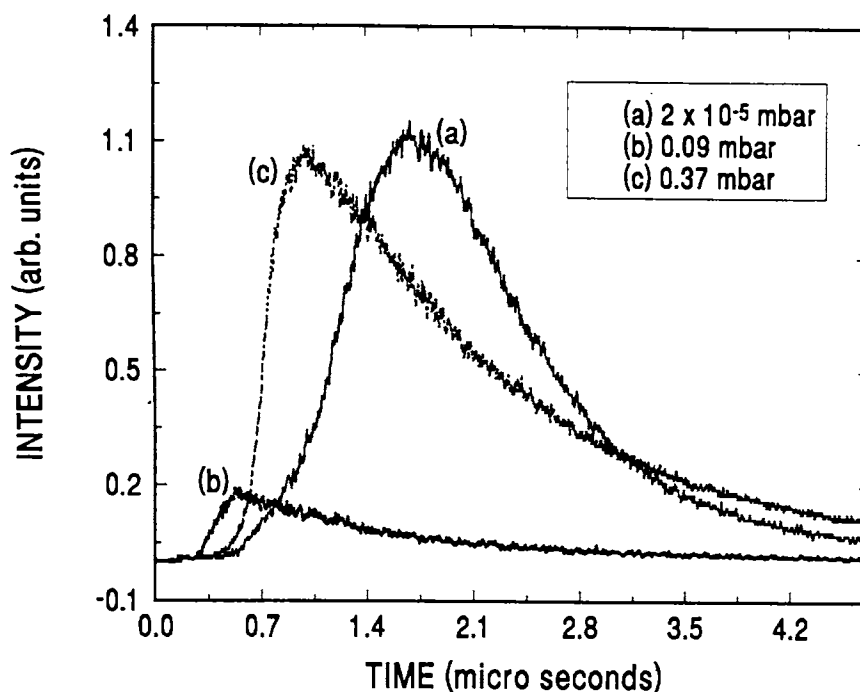


**Figure 3.1** Time of flight profile at different ambient pressures. (a)  $2 \times 10^{-5}$  mbar (b) 0.09 mbar and (c) 0.37 mbar. The optical emission line at 546.5 nm from excited silver atoms is selected for temporal measurements. The data is taken 0.5 cm from the target and at a laser power density  $5 \times 10^{10}$  W cm $^{-2}$ .

Fig.3.1 show the oscilloscope traces of the TOF signal of atomic silver at a laser power density of  $5 \times 10^{10}$  W cm $^{-2}$  at various ambient pressures and at a distance of 0.5 cm in front of the target surface. As has been reported earlier for the case of ionic species,<sup>35</sup> one may expect the velocity to increase as the pressure is decreased since the collisional deceleration and scattering of the particles with the ambient gas molecules is much lower at reduced pressures. Also the TOF signal became narrower implying a smaller velocity spread as the pressure is lowered. However, at ambient pressures below  $4 \times 10^{-3}$  mbar a second peak is developed in the TOF signal indicating a slower component. The temporal spread is larger for the newly developed peak and a trace of a fast component also is seen. The atomic species in the plasma corresponding to the two peaks seem to possess widely different evolution dynamics as will be seen below.

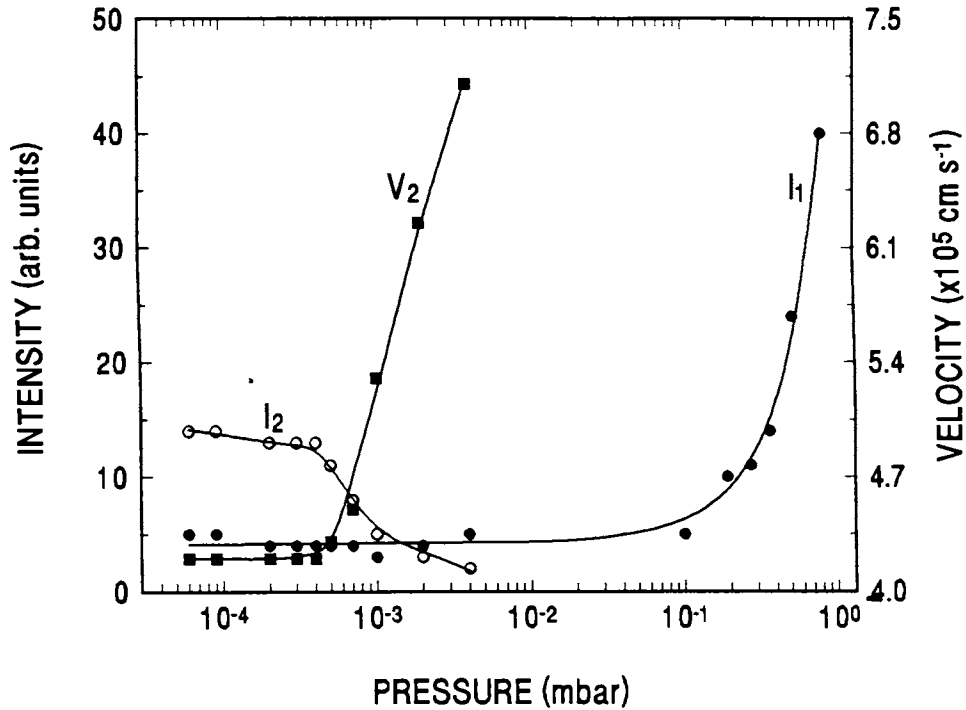


**Figure 3.2** Figure showing the intensity as well as the velocity of the two peaks with respect to chamber pressure. There exists an intermediate pressure region where the plasma emission is almost nil.

Fig.3.2 shows the intensities as well as the velocities of the two peaks (hereafter we use the notation P1 for the faster peak and P2 for the delayed peak developed at low pressure) as a function of ambient pressure. The emission intensity not only corresponds to the overall plume density but also the plasma temperature. The fast component, P1 has maximum intensity at relatively high ambient pressures and the intensity gradually reduces as the pressure is reduced. This can be explained as due to the populated excited states resulting from various collisional processes like three body recombination of ions and electrons, electron impact excitation etc. which depend on the temperature as well as the density of the plasma which in turn decide the charge transfer and recombination processes. However, the intensity of P2 is somewhat higher below  $4 \times 10^{-3}$  mbar and is almost constant below  $1 \times 10^{-3}$  mbar. Therefore an additional source for the neutrals is indicated below  $4 \times 10^{-3}$  mbar. The velocity ( $V_2$ ) of the species corresponding to the P2 is found to increase with the

pressure till the two peaks in the TOF profile merge with each other above  $10^{-3}$  mbar. This shows that at relatively high pressure the two types of species have the same dynamics. The peak velocity corresponding to P1 has a constant value of  $1.7 \times 10^6$  cm s<sup>-1</sup> (not shown in the figure) at different pressures and within the plasma boundary with the ambient gas. That is, P1 is relatively unaffected by the presence of the background gas. This component is the one which penetrates the background gas with almost the same velocity as in the case in vacuum. The decrease in intensity could be due to the depletion of the excited state molecules at reduced pressure due to smaller number of collisional excitations.

### 3.2 Space-resolved intensity measurements and plume expansion

The intensity as well as the velocity at a pressure of  $2 \times 10^{-5}$  mbar as a function of distance from the target is shown in Fig.3.3. The intensity of P1 is rapidly decreased just above the target surface and thereafter it levels off. But in the case of the P2 at reduced pressure, the intensity first shows a small increase and then decreases gradually. Therefore one can safely assume that the major source of the slower species is not the target surface, but they originate from a region slightly away from the target surface. The intensity maximum occurs at a distance of about 0.1 cm away from the target surface. The velocities at various distances are also shown in Fig.3.3. For P1, the velocity remains steady up to about 0.6 cm and thereafter increases linearly. This means that above a certain distance, the particles obtain an additional kinetic energy. One possible reason for this could be the three body recombination of ions and electrons. The energy gained through three body recombination is converted to kinetic energy of atoms. The linear increase in the velocity is in agreement with the widely accepted theory of adiabatic plasma expansion.<sup>19,20</sup> During adiabatic expansion, the x-component of the velocity  $v_x$  is given by the relation,

$$v_x = \frac{x}{X(t)} \frac{dX(t)}{dt} \quad (3.1)$$

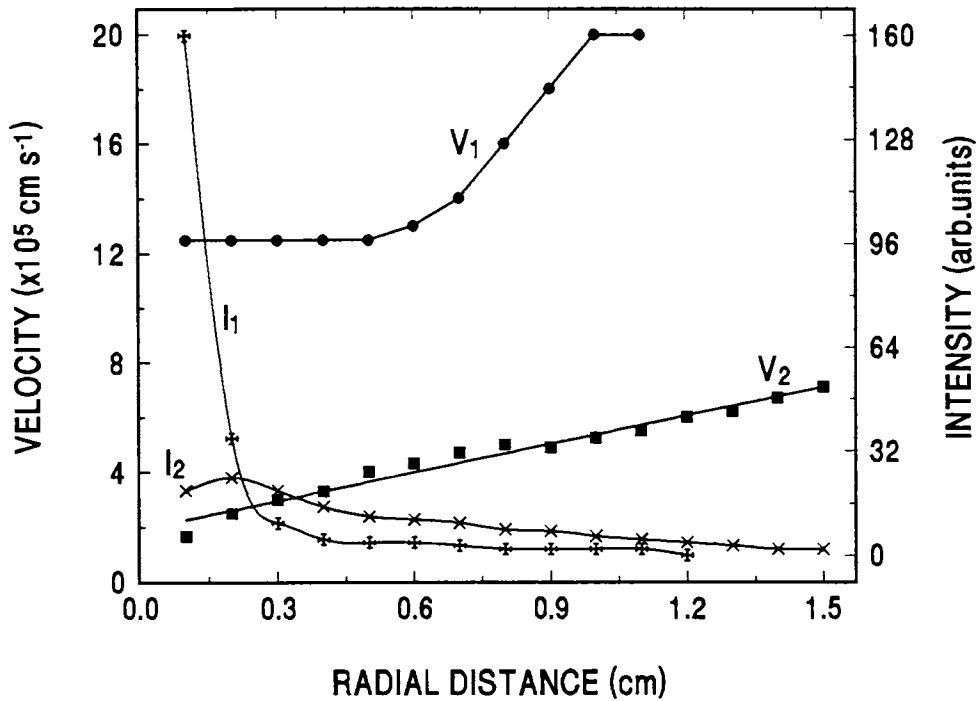


**Figure 3.3** Variation of the intensities and peak velocities of the two set of silver atoms with respect to distance from the target at  $2 \times 10^{-5}$  mbar.

Here  $X(t)$  is the dimension of the expanding plasma in x-direction and corresponds to the distance at which the plasma density decreases to 60.65%.<sup>20</sup> In the case of adiabatic plasma expansion, the velocities of all the constituent species increase linearly with distance from the target. In the case of P2, the velocity shows a linear increase with distance, characteristic of adiabatic plasma expansion. These observations on the intensity and velocity variations with respect to pressure and distance from the target clearly reveal the independent origin and dynamics of these two species as mentioned earlier.

At relatively high pressures, the plasma has to encounter increased resistance from the ambient gas molecules and a shock wave is formed at the plasma boundary. In general, there are various models like the drag model and the shock model which satisfactorily describe the plasma dynamics in the presence of an ambient gas. Drag model predicts that the plume will come to rest as a result of the resistance due to collisions with the ambient gas. In the shock model the expanding products ejected from the target act like a piston which accelerate the ambient gas to supersonic



speeds causing a shock wave ahead of the contact surface.<sup>33,36</sup> Within the assumptions pertaining to strong explosions, the position of the shock front  $R$  can be described as,<sup>33</sup>

$$R \approx \xi \left[ \frac{Et^2}{\rho(\infty)} \right]^n \quad (3.2)$$

where  $\xi$  is a scaling factor ( $\approx 1$  for air),  $\rho(\infty)$  is the undisturbed density of the background gas,  $E$  is given by the sum of the kinetic energy of the shock wave and the thermal energy of the vapor plume. The value of  $n$  depends on the symmetry of the shock front and for cylindrical symmetry  $n$  is equal<sup>33</sup> to  $1/4$ . In our case at relatively high pressure only the fast peak appears and the position-time plot for this is shown in Fig.3.4 at a pressure of 0.09 mbar. The dotted line is a power law fit to the data showing that the shock front obeys  $R \propto t^{1/2}$ . This means that  $n \approx 1/4$  and the shock wave almost has a cylindrical symmetry. At low pressure both P1 and P2 do not give any indication of the formation of the shock wave but instead show a rapid increase in  $R$  with time. Parabolic fits of the observed data for P1 and P2 are shown in Fig.3.4 corresponding to  $n = 1$  in Eqn.3.2 and with different scaling factors  $\xi$ . Thus such a behavior turns out to be characteristic of adiabatic expansion. The velocity of the particle is related to  $R$  through the relation,

$$v = aR^{-3(1-\alpha)} \quad (3.3)$$

where  $a$  is a constant.<sup>36</sup> Here  $\alpha$  is a fraction defined as  $P_c = \alpha P$ , where  $P_c$  is the pressure at the inner side of the shock front and  $P$  is the pressure behind the shock front. Fig.3.5 shows the velocity as a function of the radial distance above the target at 0.09 mbar. Initially the velocity shows an almost linear increase and it eventually comes down beyond a distance 0.3 cm from the target. The solid line in the figure is a model fit to the observed data for distances greater than 0.3 cm with  $\alpha = 2/3$  and  $\alpha = 4/3$ . At reduced pressure such a power law dependence of  $R$  on  $t$  such as the one described above is not observed.

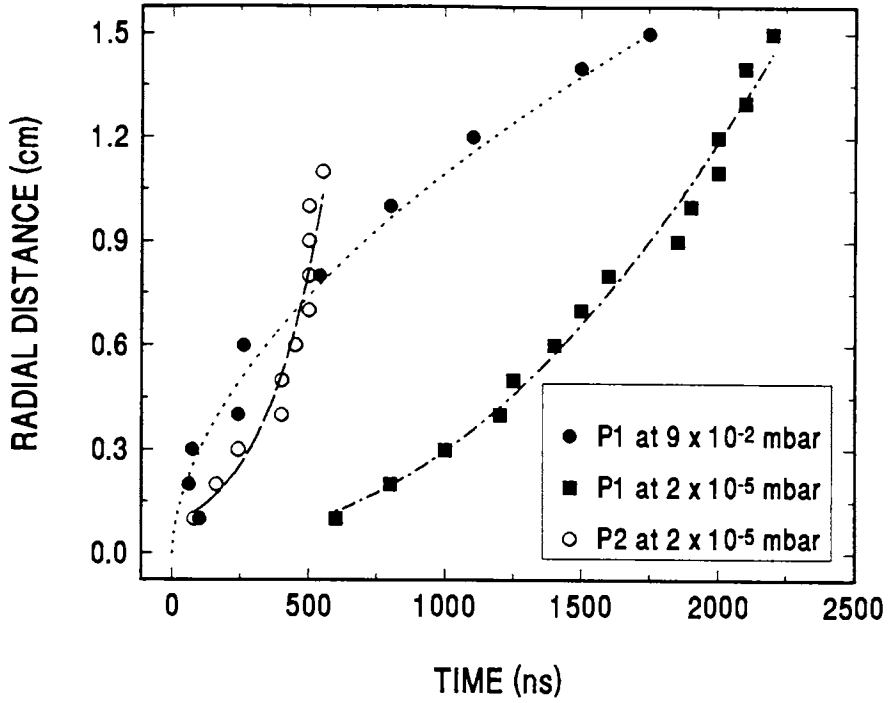


**Figure 3.4** Distance from the target ( $R$ ) as a function of time ( $t$ ). At relatively high pressure (0.09 mbar typically) the dependence is close to  $R \propto t^{1/2}$  while at reduced pressure the two peaks show much steeper evolution.

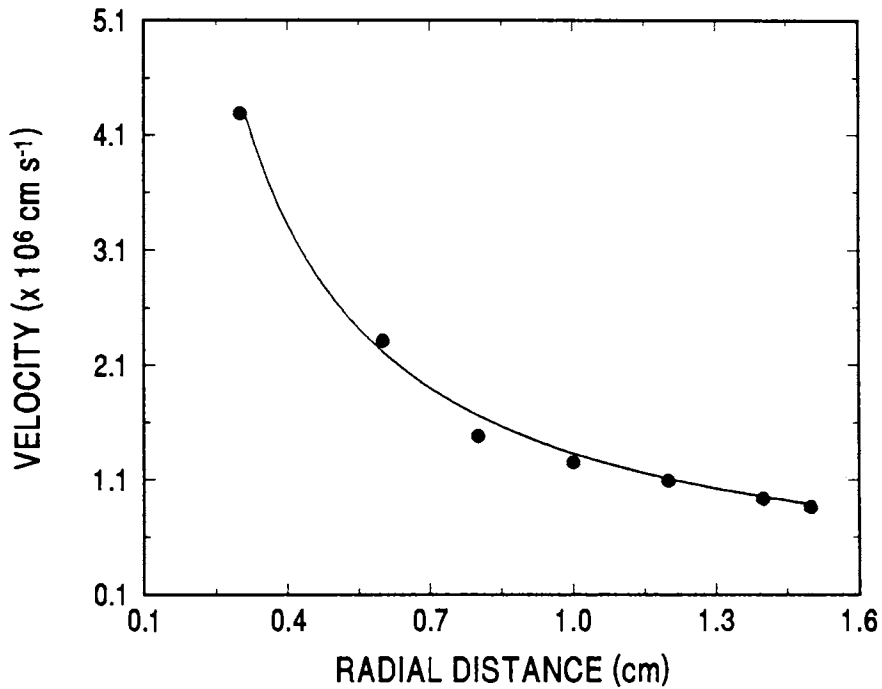


**Figure.3.5** Peak velocity corresponding to P1 as a function of radial distance at 0.09 mbar pressure. The solid line represents a fit to the data satisfying the shock model of plasma expansion.

### 3.3 Temporal profiles and time-resolved spectra at the plasma core

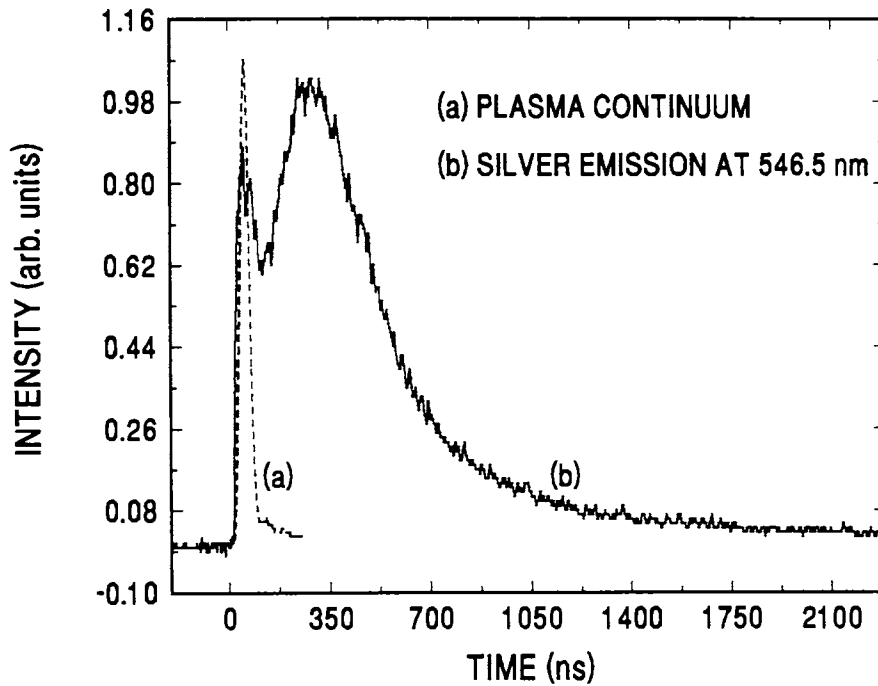


**Figure 3.6** The temporal profiles at the plasma core at two distinct wavelength. The two profiles show widely different characteristics which is explained in the text.

While doing the space-wise mapping of the TOF profiles in the plasma, the core region was also subjected to investigations. The plasma core is very bright and generally gives out white light emission. The time of flight profiles at the core are given in Fig.3.6. The TOF profiles depend critically on the wavelength of observation, *i.e.* whether one is observing at the continuum region or at an emission line of a particular species. Fig.3.6(a) shows the TOF profile when observed at the plasma continuum and Fig.3.6(b) shows that at the silver atomic emission at 546.5 nm. Two peaks are observed in the case of atomic emission which means that before the atomic species are produced, species which are responsible for the continuum emission are ejected from the target.

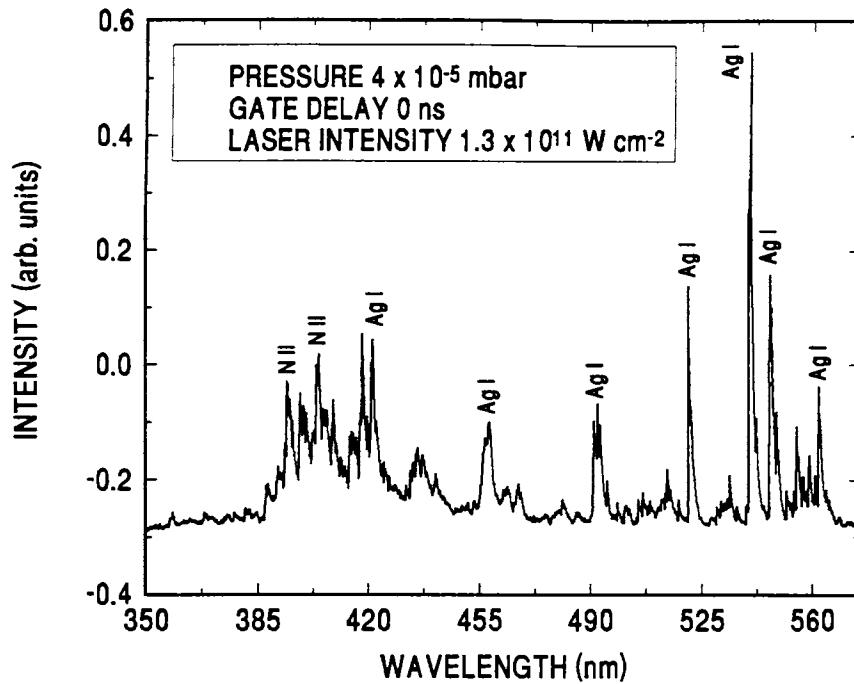


**Figure 3.7** The emission spectrum at the plasma core at a gate delay 0 ns and gate width 250 ns

In order to have a more clearer picture on the nature of the spectra during the existence of each peak, optical emission is recorded in the region 400-650 nm with the help of a boxcar averager for time gating. The spectrum during the first temporal peak (to be specific, gate delay 0 ns and gate width 250 ns) is shown in Fig.3.7. The spectrum shows continuum nature without any line emissions. The main sources of continuum emission are bremsstrahlung radiation and radiative recombination. In other words, the ions and electrons are responsible for continuum emission through either free-free or free-bound transitions. A more detailed description of these phenomena is given in chapter 7 while describing laser plasmas in air at normal atmospheric pressure.

Fig.3.8 shows that during the time period of the second peak (*i.e.* gate delay 720 ns and gate width 250 ns), the line-to-continuum ratio is large or one can say that the spectrum is dominated by line emissions. Therefore, the temperatures for this time period is assumed to be smaller since the rate of recombination and the subsequent de-excitations overcomes the rate of ionization. In short, during laser interaction with matter

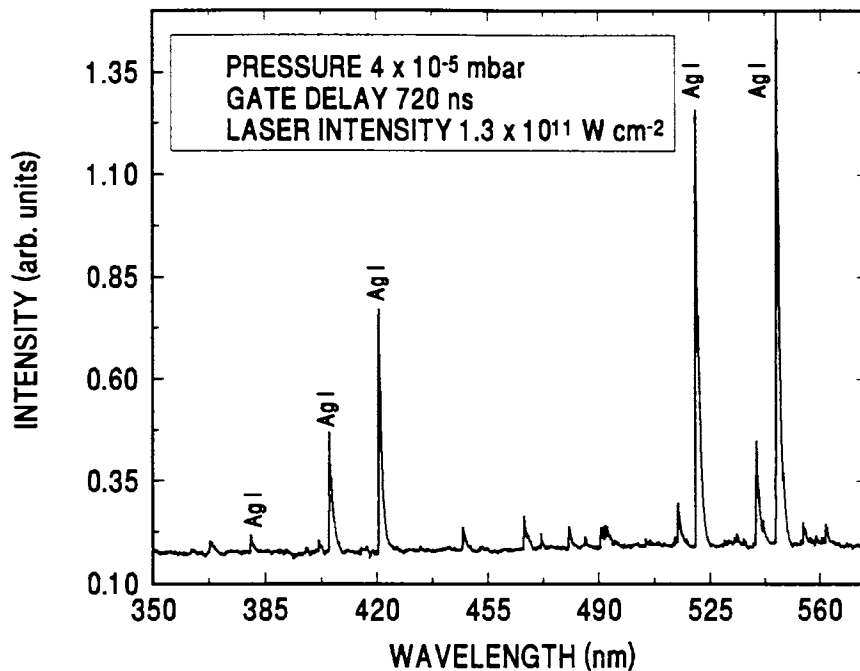


**Figure 3.8** The emission spectrum at the plasma core at a gate delay 720 ns and gate width 250 ns

initially there is a bunch of charged particles (mostly positive ions and electrons) which lasts only for a few nanoseconds and thereafter the plasma cools down, hence recombination and subsequent de-excitations dominate. The presence of plasma continuum is evident only inside the core and just outside the core the density and temperature are not high enough to produce continuum radiation.

### 3.4 Dynamics of positive ions

The mechanisms of laser absorption by materials vary widely depending on their optical, structural and thermal properties. In metallic solids, the laser absorption is primarily by the conduction electrons through inverse bremsstrahlung and the absorbed energy is transferred to the lattice through electron-phonon interactions. The electron-phonon energy transfer occurs in picosecond time scales and the temperature of the lattice rises well above the melting point and the material rapidly evaporates from the condensed phase. The pressure developed at the ablative spot can be as high as  $10^4$  atmospheres<sup>37</sup> (see section 1.4, Chapter 1) and the ablative products rapidly expand out of the focal spot to the surrounding low pressure ambient. The plume expansion and cooling

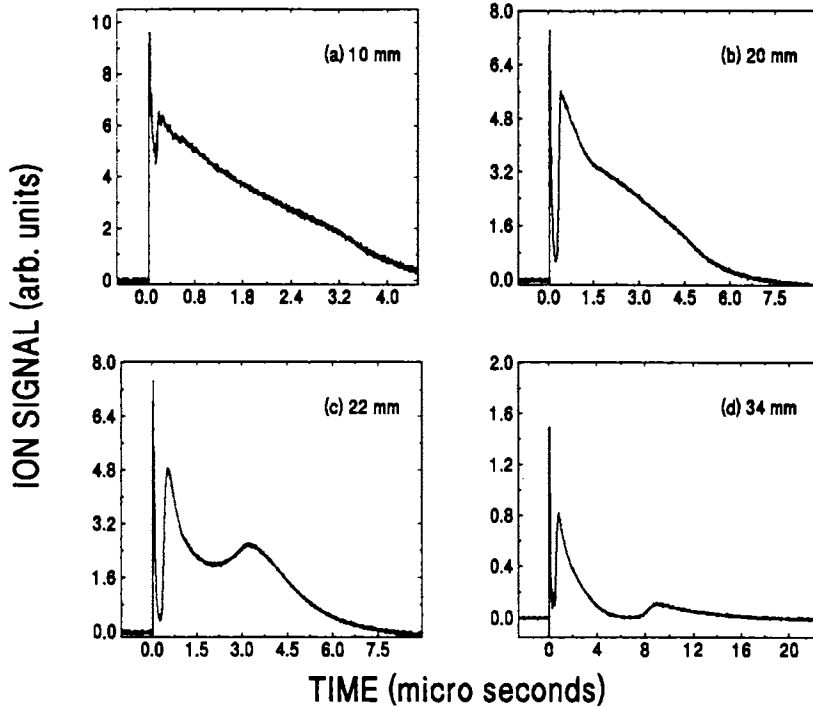
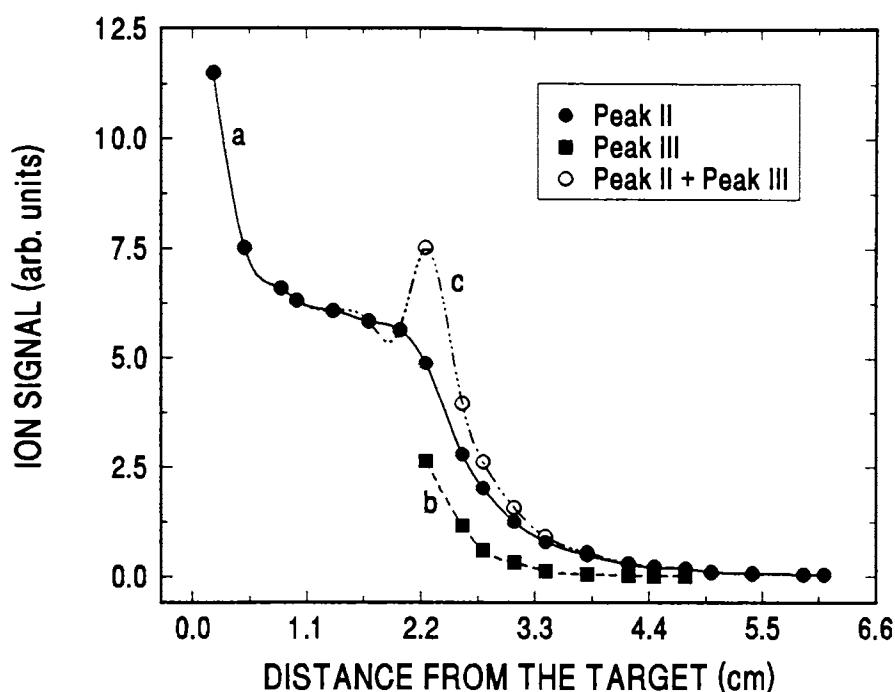


**Figure 3.9** TOF profiles of the positive ions at different distances from the target. Close to the target there are two peaks and the second peak splits into two at around 2.0 cm from the target. Laser power density is  $1.7 \times 10^{11} \text{ W cm}^{-2}$  and pressure 0.22 mbar

dynamics are expected to have a number of similarities with those of free jet expansion used to generate supersonic molecular beams since the average particle speed is many times higher than the mean random thermal speed and since the flux of the material is highly forward peaked<sup>38</sup>.

### 3.4.1 Spatial dependence of ion TOF profiles

At relatively high pressures the shock wave model explains the behavior of the ablation front.<sup>31</sup> During expansion the plasma acts like a piston and it expands in to the ambient with supersonic velocities and a shock front is generated. At a certain distance from the target, the pressure just before and after the ablation front equalizes and forms a well defined boundary. This boundary between the ablated plume and the ambient gas has not been studied in any great detail so far. At the boundary there exists a turbulent mixing of the ablation plume with the ambient gas. This might feed the onset of Raleigh-Taylor instability and other nonlinear processes at the boundary.<sup>32,39</sup> A shock front might be expected to occur when the plume and background pressures are equal.<sup>40</sup>



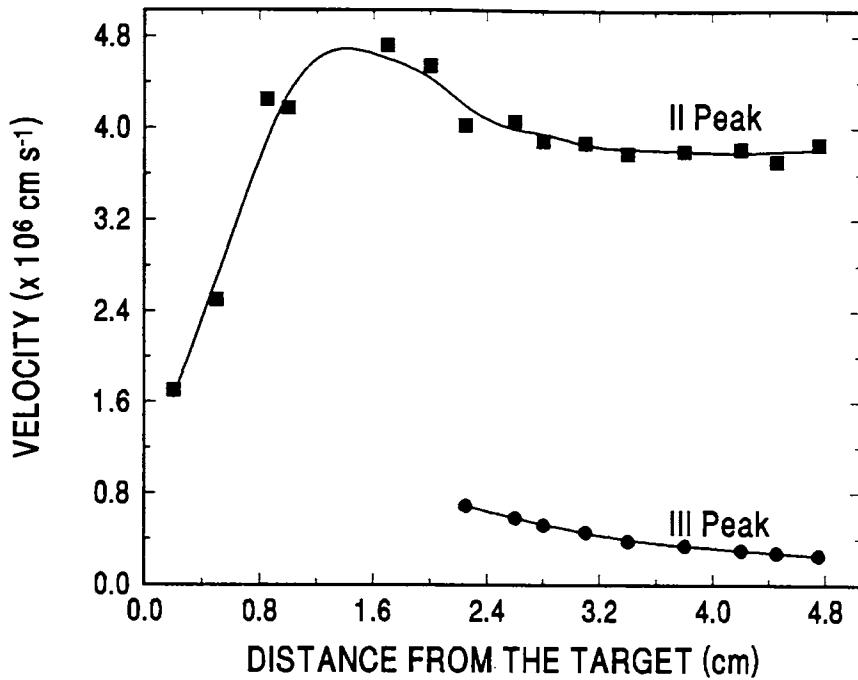
**Figure 3.10** Figure showing the variation of probe signal amplitude as a function of distance from the target. Curve (a) shows the probe signal corresponding to peak II and curve (b) that of III peak. The dotted line (c) is the sum of amplitudes of peak II and peak III which shows steepening of the ion front at the boundary.

Fig.3.9(a-d) show the TOF profiles of the ionic species in the laser produced silver plasma obtained using a negatively biased Langmuir probe. At distances close to the target, the TOF profile has only two peaks. The initial one is due to the presence of ionized ambient molecules. The ambient molecules are ionized primarily by collisions with electrons generated during laser interaction with silver. In fact there are two distinct temporal peaks in the TOF profile of the electron pulse, the one which lasts only during the laser pulse and the other which is much broader and comprising of electrons contained in the silver plasma.<sup>41</sup> The first prompt electron pulse is energetic enough to collisionally excite and ionize the ambient molecules and hence there is a local density of ambient ions. Therefore, the first peak in the ion TOF profile thus is due to the presence of the ionized ambient molecules. All these facts have been detailed in Chapter 4. The second is due to the ions in the laser-plasma which lasts for several microseconds. At around 2.2 cm away from the target surface, this second peak splits into two well defined peaks which continues for larger distances as shown in

Fig.3.9(d). Therefore, there exists a definite distance away from the target for the onset of this splitting. This has been observed recently in carbon plasma during spectroscopic investigations.<sup>42</sup>

Figs.3.10 (a) and 3.10 (b) show the intensity of the two peaks (Peak II and Peak III) as a function of distance from the target surface. Initially there is a sharp decrease in the ion probe current with respect to distance. This is expected since the probe current is proportional to the density of ions. The density of ions decrease very sharply with distance away from the target and this is evident from the sharp reduction in the probe current close to the target. Thereafter the probe current and hence the density of ions levels off up to a distance of 2.2 cm from the target surface. Again there is a sharp cut off in the probe current beyond 2.2 cm. At this point the latter temporal peak splits into two distinct components as shown in Fig.3.9 (c). The probe current due to the third peak also falls off gradually with distance. The dotted line in Fig.3.10 (c) shows the sum of the intensities of the two latter peaks as a function of distance. This indicates that there is a steepening of the ion front at the boundary. This is in qualitative agreement with the theoretical predictions of Sach and Schamel<sup>43</sup> and also by Eliezer and Hora<sup>44</sup> for charged double layer formation at the boundary. In the usual plasma expansion process, there exists a pure electron cloud ahead of the ion front. Hence there is a separated electron and ion charge clouds over the boundary of the plasma since the electrons being lighter diffuse faster than the ions in to the ambient. The separated ion and electron clouds are termed together as charged double layer which is defined to be regions of non-neutral plasma and consists of two adjacent non-neutral regions of opposite charges.<sup>45</sup> The typical separation between the oppositely charged layers is of the order of the Debye length which has dimensions usually of the order of microns. This in turn will accelerate the ions at the expense of electron energy causing an enhancement in the ion velocity in the vicinity of the boundary. The fast ions will then charge exchange with the neutral species which results in a new population of slow ions and fast species.<sup>40</sup> This is true in the present case also as shown in Fig.3.11. As we move away from the target surface, initially there is an increase in velocity with distance. This is in agreement with the predictions of adiabatic plasma expansion and here the thermal energy of the particles is converted





**Figure 3.11** Plot between the distance from the target and the velocity of ions. Particles corresponding to the III peak shows a gradual decrease in velocity. II peak velocity begin to decrease beyond 2 cm but attains a steady value beyond 2.2 cm.

to kinetic energy. But at about 2.0 cm, the velocity attains the maximum value and begin to decrease. But beyond 2.2 cm, the velocity remains constant indicating that there is an additional source of energy which accelerates the particles at the boundary. Just at the same point the second peak begin to develop and the velocity of which drops off rapidly with distance. This is because, the species constituting the third peak are decelerated due to collisions with the ambient molecules or atoms. The velocity of the species in the second peak remains constant beyond the boundary.

### 3.4.2 Influence of pressure on ion profiles

The emission characteristics, temperature and density of the plasma are influenced by the ambient conditions. The plume angular distributions and species velocities are greatly affected by the energy transfer between the plume and the ambient medium. At relatively high pressure, the plume is physically confined to smaller volumes and consequently the density and temperature are high. The onset of double

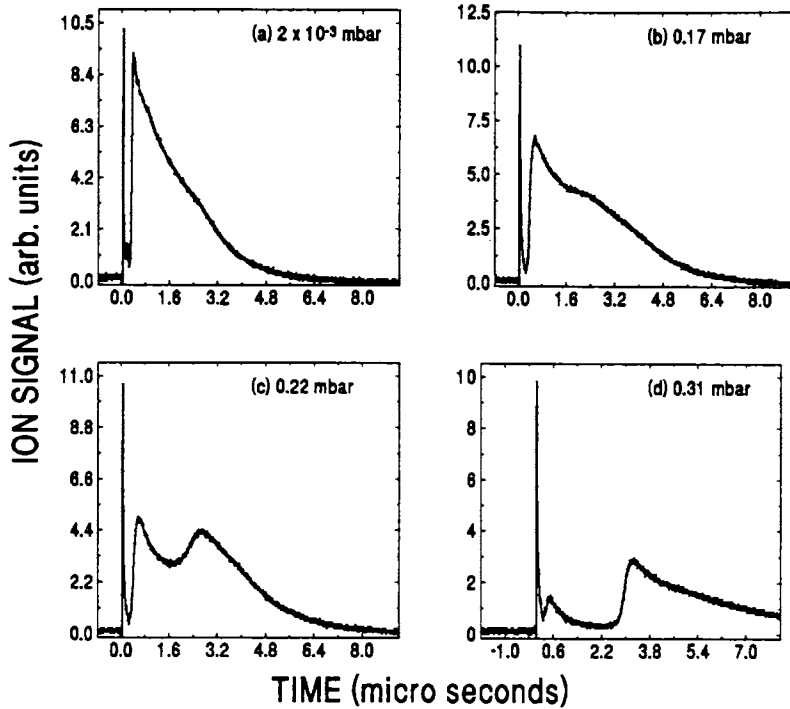


**Figure 3.12** TOF profiles of ions at different chamber pressures at a distance 2.2 cm away from the target. Laser power density  $1.7 \times 10^{11} \text{ W cm}^{-2}$ . Profiles show that the peak splitting depends on ambient pressure in the chamber

peak is highly pressure dependent and Fig.3.12(a-d) represents the pressure dependent TOF profiles at a distance 2.2 cm away from the target surface. It is observed that the peak splitting occurs around 0.17 mbar and as the pressure is increased, the two latter peaks become separated more in time.

Laser plasma expansion into an ambient gas has been well explained with the shock wave model of plasma expansion. The position of the shock front ( $R$ ) is related to the expansion time through Eqn. (3.3). Fig.3.13 gives the position-time graph for the second peak. The solid curve shows that  $R \propto t^{1/2}$  which is typical of a shock wave with cylindrical symmetry which is described earlier. Fig. 3.13 clearly indicates the presence of the shock waves at the expansion front. As has been explained in section 3.3.2, the plasma expansion into relatively high pressure ambient gas, the expansion front forms a shock wave having cylindrical symmetry. On the other hand for ambient pressure

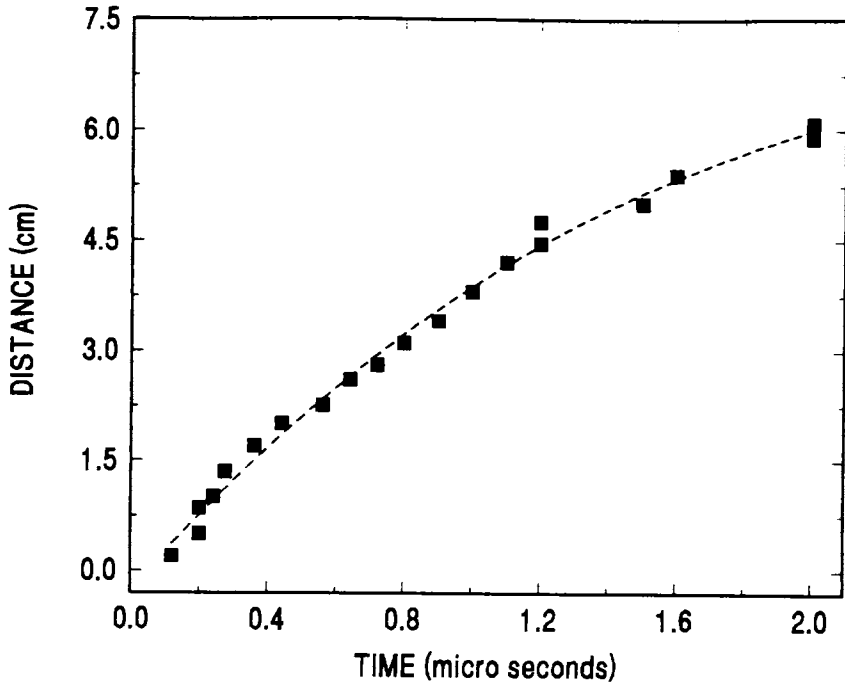


Figure 3.13 Plot between the radial position and time for the species corresponding to the second peak in the ion TOF profile

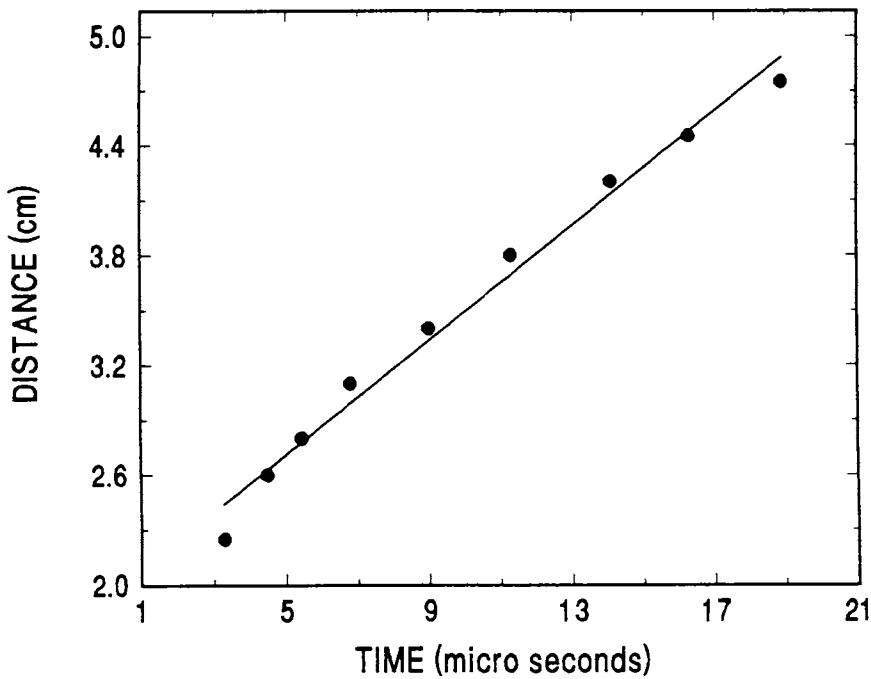


Figure 3.14 Plot between the radial position and time for the species corresponding to the third peak in the ion TOF profile

below  $10^{-3}$  mbar, the shock front formation is absent and the position of the ablation front has a parabolic dependence on expansion time. This is in accordance with the predictions of the well accepted theory of adiabatic plasma expansion recently reviewed by Singh and Narayan.<sup>19,20</sup> Fig.3.14 shows the position-time graph for peak III in which case the position of the ablation front is almost linearly proportional to the expansion time. Therefore the species corresponding to the third peak does not form a shock front instead it is decelerated by the ambient molecules.

Pressure dependent species TOF profiles during laser ablation of ZnTe have been analyzed by Lowndes<sup>30</sup> et al. in a recent report. They have observed three distinct types of species in the temporal profile at a particular distance from the target and at different ambient nitrogen pressure. The three peaks were identified as (a) the fast component due to the unscattered ions (b) ions that are slowed down by gas-phase collisions and (c) slow moving clusters formed through collisions. In the present report the chamber pressure is totally different from that of Lowndes et al. and also the nature of the target is different in the present experiment and hence the target absorption mechanism is different. Therefore the same explanations given by Lowndes et al. do not seem to hold in the present case.

### 3.5.3 Ion TOF profiles as a function of laser energy

The laser pulse power density plays a vital role in determining the dynamics, electron temperature and density of the plasma which reflect in the characteristics of the pulsed laser deposited thin films. The appearance of the third peak at a definite distance from the target depends critically on the laser intensity also. This is shown in Fig.3.15 at a distance of 2.2 cm from the target surface. At lower laser intensities, only the first two peaks were present and as the laser intensity is increased, the third peak begin to develop. But at very high laser intensities, the two latter peaks begin to overlap and the delay of the third peak decreases. At comparatively low incident laser intensities, the laser directly encounters the target and ablation takes place. But as the laser intensity

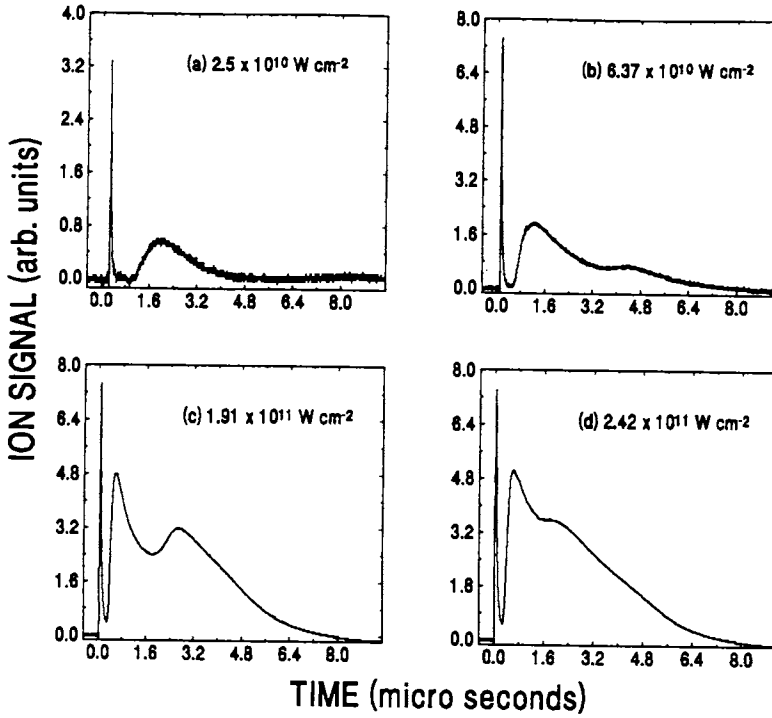


**Figure 3.15** TOF profiles of ionic species at different laser power densities. Distance from the target is 2 cm and chamber pressure 0.22 mbar

is increased, the leading part of the laser pulse itself is energetic enough to produce high density plasma within the etch depth. This plasma when confined to the volume of the etch spot will have densities higher than the critical density and in that case the laser photons will be screened off by the plasma from reaching the target. So the trailing edge of the laser pulse interacts primarily with the plasma when the densities are below the critical density. The incident laser power is absorbed by the plasma electrons directly through inverse bremsstrahlung, the absorption coefficient of which is given by<sup>46</sup>

$$\alpha_p = 3.69 \times 10^8 \left( \frac{Z^3 n_i^3}{T^{1/2} \nu^3} \right) (1 - e^{-h\nu/kT}) \quad (3.4)$$

where  $Z$ ,  $n_i$ ,  $T$  and  $\nu$  are the average ion charge, ion density, plasma temperature and frequency of laser light respectively. The above equation suggests that the absorption of photons by free electrons in a plasma is most effective at larger wavelengths and at

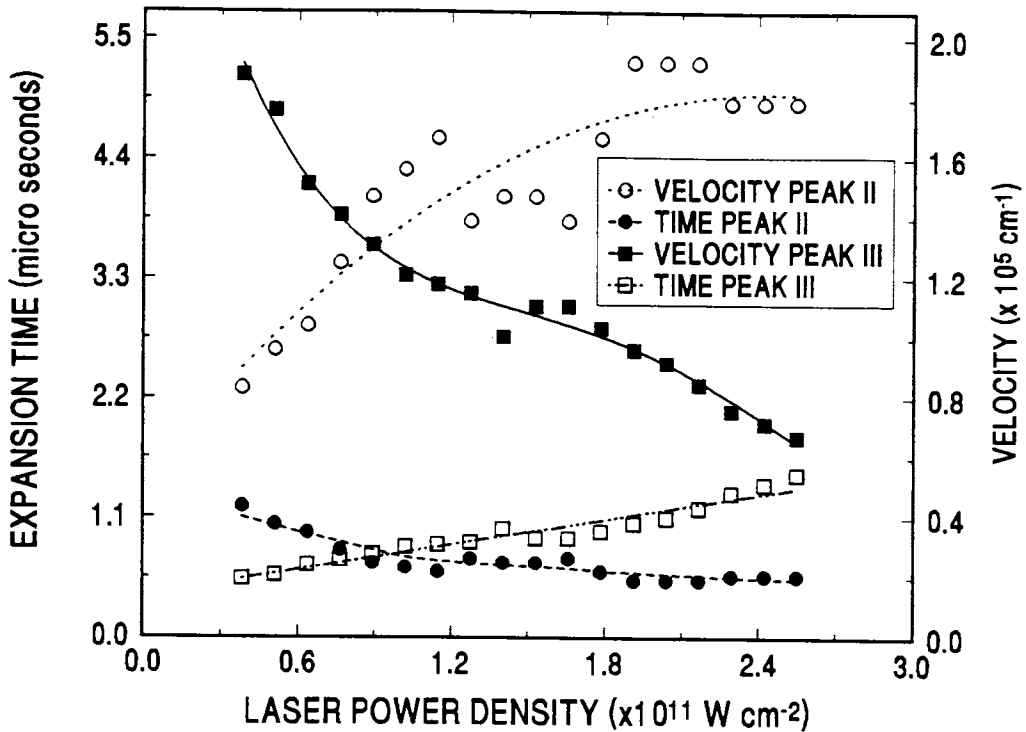


**Figure 3.16** Curve showing the expansion time and the velocities of peak II and peak III as a function of laser power density. The measurements is done at a distance 2 cm from the target and with chamber pressure 0.22 mbar.

relatively low temperatures. The absorbed energy is transferred to the ionic and neutral species in the plasma through collisions. At still higher fluences, the leading edge of the laser pulse produces plasma with densities higher than the critical electron density and in that case the laser light will be shielded off by the plasma. It has been reported<sup>37</sup> that during picosecond laser interactions, the shielding is due to absorption of laser light through inverse bremsstrahlung by fast electrons during collisions with gas atoms and with nanosecond laser interaction the shielding is due to the absorption by the atoms and ions. But we have recently observed fast prompt photoelectrons with energies  $\sim 60 \text{ eV}$  during nanosecond laser interaction with silver<sup>41</sup> and it is shown that during nanosecond laser interaction also the laser-heated photoelectrons play a major role in plasma shielding.

Fig.3.16 gives the variation of the time delays and velocities of the second and third peaks as a function of laser intensity at a distance 2 cm from the target surface. The expansion time decreases with laser power density for both the peaks. This means that the ions gain energy from the laser pulse. At high laser intensities, the velocity of the

faster peak (Peak II) is saturated whereas the velocity of the slower one (Peak III) continues to increase with laser intensity.

### 3.5 Space-resolved electron temperature measured using Langmuir probes

The two quantities which are of prime importance in any type of plasma are the plasma electron temperature and electron number density. Precise knowledge about these two quantities yields important conclusions on the nature of the plasma. Optical emission measurements from the constituent species is a suitable method for the determination of these parameters under local thermodynamic equilibrium (LTE) conditions. But in the case of laser-plasma optical emission diagnostic does not seem to be a suitable technique for determining plasma parameters over the full extent of the plasma even though it is commonly employed in laser-ablated plumes. This is because the conditions of LTE is not strictly valid in the case of laser-produced plasmas especially in regions sufficiently far from the target surface. But a properly biased Langmuir probe can be effectively used under circumstances where deviations from LTE may exist. But here the general assumption is that the particles obey Maxwell-Boltzmann velocity distributions. The applied probe potential does not accelerate or decelerate the charged particles in the plume<sup>47</sup> beyond the length equal to the Debye length which has dimensions of the order of microns. The plasma electrons shield the plume from the probe potential until distances equal to the Debye length. Thus Langmuir probes are effectively used for TOF measurements as well as for the determination of  $T_e$  and  $n_e$ . The theory and various experimental procedures are described in section 2.4 (Chapter 2) and now the prominent results will be discussed.

The time integrated electron temperature as a function of distance from the target is given in Fig.3.17 which shows that near the target ( $\approx 0.15$  cm) the temperature is  $\approx 20$  eV. This value of  $T_e$  is substantially higher than that due to the time resolved measurements to be described in section 4.1 (Chapter 4). It is difficult to go still closer to

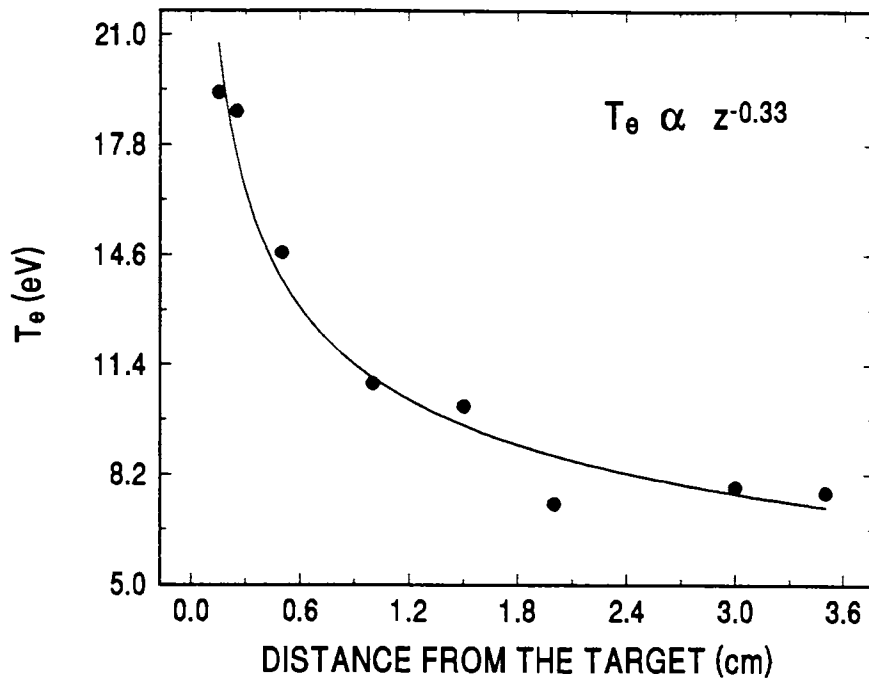


**Figure 3.17** Plot showing the variation of electron temperature with distance. The solid line show that  $T_e \propto z^{-0.33}$ .

the target with better spatial resolutions due to experimental configurations. But one can estimate the electron temperature at the focal spot using Eqn.1.23 (Chapter 1) and the electron temperature at the etch spot with a laser power density of the order of  $10^{10}$  W  $\text{cm}^{-2}$  is approximately 29 eV. There exists a temperature gradient along the target normal and the temperature rapidly falls off as the distance is increased. The solid line in Fig.3.17 is a power law fit to the observed data obeying the relation  $T_e \propto z^{-0.33}$  where  $z$  is the distance from the target surface. This is not in complete agreement with the temperature variations given in Ref.17 where it is shown that  $T_e \propto z^{-0.1}$ . The main reason that we find for the discrepancy is the difference in ambient and initial conditions.

### 3.7 Summary

The TOF signals of ablated species are investigated as a function of Argon ambient pressure and distance from the target surface. An anomalous behavior in the temporal profile of silver atoms inside the plasma is observed. Above a pressure of  $4 \times 10^{-4}$  mbar, only one peak in the TOF profile exists while below that pressure a new peak begins



to develop. The newly developed peak gives a maximum velocity for silver atoms which is much lower than that indicated by the first peak. The faster component expands one dimensionally with a constant velocity of  $1.25 \times 10^6 \text{ cm s}^{-1}$  upto a distance  $\approx 0.6 \text{ mm}$ . Thereafter it expands adiabatically with a linear increase in velocity with distance. This velocity at any point does not appear to change with pressure. The temporal peak originated at reduced pressure show the behavior of unsteady adiabatic expansion. The corresponding particles are those which are retro-reflected from the ablation spot. This velocity spread of the slow peak is an indication of the randomness in the velocities of the species. At reduced pressure the Knudsen layer feeds an unsteady adiabatic expansion with more forward peaked angular distribution. Spatio-temporal data at relatively high pressure show that the plasma can be modeled according to the predictions of shock wave theory of plasma expansion. The observed data show that the shock wave has cylindrical symmetry. At reduced pressure the observed data do not fit with the shock wave model, instead show a parabolic increase in  $R$  with time  $t$ .

In the second part the dynamics and TOF profiles of the ionic species were analyzed using a Langmuir probe. The behavior of the ions at the plasma boundary is studied by varying the distance from the target, laser power density and pressure inside the chamber. There is a steepening of the ion front at the plasma boundary which results in the onset of a charged double layer, a region of separated positive and negative charges. This results in the acceleration of the ions at the expense of the electron energy. The observation of the saturation of ion velocity beyond the plume boundary indicates that the ions gain energy from the double layer. Change in pressure and laser power density give rise to the triple peak structure in the ion TOF profile.

The vital parameter characterizing the plasma, viz. the electron temperature ( $T_e$ ) as a function of distance from the target ( $z$ ) has been measured using a Langmuir probe.  $T_e$  drops with distance showing a relationship  $T_e \propto z^{-0.33}$ . This is not in complete agreement with the previously reported behavior. We believe that this is due to

the difference in the ambient conditions as well as the initial conditions which exist at the focal spot.

## References

- <sup>1</sup>D B Geohegan, *Thin Solid Films* **220** (1992) 138.
- <sup>2</sup>Z Andreic, V H Bartolic and H J Kunze *Physica Scripta* **48** (1993) 331.
- <sup>3</sup>U Teubner, T Mirsala, I Uschmann, E Foster, W Theobald and C Wulkern *Appl. Phys. B* **62** (1996) 213.
- <sup>4</sup>W Piestch, B Dubreuil and A Briand *Appl. Phys. B* **61** (1995) 267.
- <sup>5</sup>E G Gamaly, *Lasers and Particle Beams* **12** (1994) 185.
- <sup>6</sup>R W Dreyfuss, *J. Appl. Phys.* **69** (1991) 1721.
- <sup>7</sup>S S Harilal, Riju C Issac, C V Bindhu, V P N Nampoore and C P G Vallabhan, *J. Appl. Phys.* **80** (1996) 3561.
- <sup>8</sup>S S Harilal, Riju C Issac, C V Bindhu, V P N Nampoore and C P G Vallabhan, *J. Appl. Phys.* **81** (1997) 3637
- <sup>9</sup>G Hatem, C Colon and J Campose, *Spectrochimica Acta A* **49** (1993) 509.
- <sup>10</sup>S S Harilal, Riju C Issac, C V Bindhu, Geetha K Varier, V P N Nampoore and C P G Vallabhan, *Pramana - J. Phys.* **46** (1996) 145.
- <sup>11</sup>Geetha K Varier, Riju C Issac, S S Harilal, C V Bindhu, V P N Nampoore and C P G Vallabhan, *Spectrochimica Acta B* (1997).
- <sup>12</sup>R Kelly and M Miotello in *Pulsed laser deposition of thin films* by D B Chrisey & G K Hubler (Eds.) (John Wiley, New York, 1994) p. 55 and references cited therein.
- <sup>13</sup>W Piestch, *J. Appl. Phys.* **79** (1996) 1250.
- <sup>14</sup>S S Harilal, Riju C Issac, C V Bindhu, Geetha K Varier, V P N Nampoore and C P G Vallabhan, *Jap. J. Appl. Phys.* **36** (1997) 134.
- <sup>15</sup>See for example G J Pert, *J. Plasma Physics* **49** (1993) 295.
- <sup>16</sup>W Sesselmann, E E Marinero and T J Chuang, *Appl. Phys. A*, **41** (1986) 209.
- <sup>17</sup>A Ritcher, *Thin Solid Films* **12** (1994) 185.
- <sup>18</sup>Yasuo Lida, *Spectrochimica Acta B* **45** (1990) 1353.
- <sup>19</sup>R K Singh, D W Holland and J Narayan, *J. Appl. Phys.* **68** (1990) 233.
- <sup>20</sup>R K Singh and J Narayan, *Phys. Rev. B* **41** (1990) 8843.
- <sup>21</sup>K Scott, J M Huntley, W A Philips, John Clarke and J E Field, *Appl. Phys. Lett.* **57** (1990) 922.
- <sup>22</sup>P E Dyer, A Issa and P H Key *Appl. Surf. Sci.* **46** (1990) 89.
- <sup>23</sup>D B Geohegan and Puretzky, *Appl. Phys. Lett* **67** (1995) 197.

- <sup>24</sup>R Kelly and R W Dreyfuss, *Surf. Science* **198** (1988) 263.
- <sup>25</sup>R Kelly and D Braren, *Appl. Phys. B* **160** (1991) 169.
- <sup>26</sup>I Noorbach, R R Luichase and Y Zeire, *J. Chem. Phys.* **89** (1988) 5251.
- <sup>27</sup>J R Ho, C P Grigoropolous and J A C Humphry, *J. Appl. Phys.* **79** (1996) 7205.
- <sup>28</sup>R Kelly and R W Dreyfuss, *Nucl. Instr. Meth. Phys. Res. B* **32** (1988) 341.
- <sup>29</sup>J C S Kools *J. Appl. Phys.* **74** (1993) 6401.
- <sup>30</sup>DH Lowndes, DB Geohegan, AA Poretzky, DP Norton and C Rouleau *Science* **273** (1996) 898
- <sup>31</sup>Riju C Issac, K Vasudevan Pillai, S S Harilal, Geetha K Varier, C V Bindhu, Pramod Gopinath, P Radhakrishnan, V P N Nampoore and C P G Vallabhan *Appl. Surf. Sci.* **125** (1998) 227
- <sup>32</sup>Abhilasha, P S R Prasad and K Thareja *Phys. Rev. E* **48** (1993) 2929
- <sup>33</sup>D Baurle *Laser processing and Chemistry*, Springer (1996)
- <sup>34</sup>J C S Kools, T S Baller, S T De Zwart and J Dielman *J. Appl. Phys.* **71** (1992) 4547
- <sup>35</sup>D B Geohegan, *Appl. Phys. Lett.* **60** (1992) 2732
- <sup>36</sup>Ya B Zel'dovich and Yu P Raizer *Physics of Shock waves and High temperature Hydrodynamic phenomena* Vol I Academic, New York, (1966).
- <sup>37</sup>R E Russo *Appl. Spectroscopy* **49** (1996) 14A
- <sup>38</sup>K L Saegner *Proc of Adv. Materials* **2** (1993) 1
- <sup>39</sup>Ronald M Gilgembach and Ventztek *Appl. Phys. Lett.* **58** (1991) 1597
- <sup>40</sup>K L Saegner *Proc of Adv. Materials* **3** (1993) 63
- <sup>41</sup>Riju C Issac, Pramod Gopinath, Geetha K Varier, V P N Nampoore and C P G Vallabhan *Appl. Phys. Lett.* **73** (1998) 167
- <sup>42</sup>A Neogi, A Mishra and R K Thareja *J. Appl. Phys.* **83** (1998) 2831.
- <sup>43</sup>Ch. Sack and H Schammel *Phys. Rep.* **156** (1987) 311.
- <sup>44</sup>E Eliezer and H Hora *Phys. Rep.* **172** (1993) 339
- <sup>45</sup>E Eliezer, H Hora, E Kolka, F Green and H Szichman *Laser and Particle Beams* **13** (1995) 441.
- <sup>46</sup>J F Reedy *Effect of high power laser radiation* Academic Press, Orlando (1971).
- <sup>47</sup>D B Geohegan in *Pulsed laser deposition of thin films* by D B Chrisey & G K Hubler (Eds.) (John Wiley, New York, 1994) p. 115 and references cited therein.

# Prompt electron emission and impact ionization during laser ablation of silver

## **Abstract**

In this chapter the observation of high current, high temperature electron pulses generated during the interaction of infrared radiation from a Nd:YAG laser with silver target is described. There are two peaks in the TOF profile; one caused by the fast prompt electrons which lasts for a few nanoseconds after the laser pulse and the second appearing much later in time having a temporal width of several microseconds. The use of prompt electrons for the excitation and ionization of ambient atoms and molecules is demonstrated.

In the previous chapter we have been describing the dynamics of the atomic and ionic species in a laser-produced plasma from silver. It is well known that in metals, light is primarily absorbed by the conduction electrons present within the skin depth through inverse-bremsstrahlung leading to rapid heating of electrons. The absorbed energy is transferred to the lattice through electron-phonon interactions which usually takes place within a few picoseconds after absorption.<sup>1</sup> The dynamics of hot electrons produced during nanosecond laser interactions and their effect on the ambient gas molecules have not received much attention in the context of the study of laser-matter interactions. Most of the theoretical and observational models on laser ablation describe the formation of the plasma, gas dynamics, laser-plasma interactions etc.

The experimental setup is almost the same as that described in Chapter 2. It consists of a plasma chamber fitted with rotary and diffusion pumps for evacuating the chamber which can then be filled with the required gas at the desired pressure. The

chamber had viewing ports through which the optical emission from the plasma can be monitored. There are provisions made on the chamber through which Langmuir probes can be inserted. The target to probe separation can be controlled from outside the chamber without disturbing vacuum. The 1.06  $\mu\text{m}$  laser beam from the Nd:YAG laser with 10 ns pulse width was focused onto the polished front surface of silver target. For each pulse a luminous plasma appears in front of the target and the plasma plume expands in a direction perpendicular to the target surface. The target was rotated about an axis perpendicular to the surface in order to avoid multiple hits at the same spot. For studies involving Langmuir probes, the target surface was kept at  $45^\circ$  to the laser beam propagation direction. The probe is positively biased through an external power supply and the transient probe current is monitored across a  $50\ \Omega$  load using a digital storage oscilloscope (DS 8651 IWATZU, 200 MHz). The oscilloscope was interfaced with a PC for data acquisition and analysis. For all the measurements described in this chapter, the pressure inside the chamber was kept at 0.22 mbar.

In the case of time-resolved spectral measurements, the plasma plume was imaged onto the entrance slit of the monochromator provided with a thermoelectrically cooled PMT for detection. The spatial resolution is obtained by placing proper slits and apertures to expose various segments of the plasma. Boxcar averager is used for gating and averaging the spectrum during time resolved measurements. The spectra were measured with the input impedance of the boxcar averager kept at  $50\ \Omega$  and the averaged output is fed to a PC for further analysis. The laser was operated at a repetition frequency of 10 Hz, and using the boxcar averager, spectral intensities were averaged out from ten successive pulses. The temporal pulse shapes of optical emission at specific wavelengths were measured directly by feeding the PMT output to the digital storage oscilloscope through a  $50\ \Omega$  load resistance.

## 4.1 Electron temporal profiles

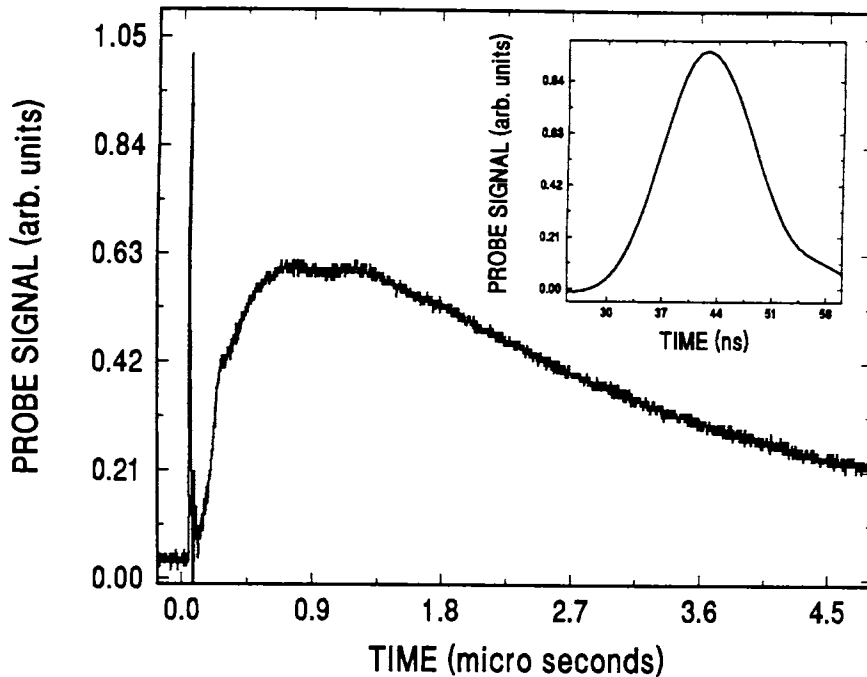


**Figure 4.1** Temporal profile of the electron pulse at a distance 0.5 cm from the target surface and at a laser power density  $1.9 \times 10^{11} \text{ Wcm}^{-2}$ . The profile shows a clear twin peak distribution. The narrow peak appears early in time represents prompt electrons and the broad peak correspond to the plasma electrons which extends over to several microseconds. The enlarged view of the first peak is shown as inset.

The bright luminous plasma generated in front of the target evolves to become an elongated plume of length about 4-5 centimeters when the chamber pressure is much less than the atmospheric pressure. At first sight the plume expansion appears to be 3-dimensional, but, since the velocity distributions are highly anisotropic and forward peaked, usually a unidirectional expansion is assumed for the plume as a first approximation. The atomic and ionic dynamics have been dealt in the previous chapter. To have a better understanding on the process of laser-matter and laser-plasma interactions it is necessary to analyze the temporal behavior of electrons also because the dynamics of electrons greatly influence the evolution of the plume.<sup>2</sup> Fig.4.1 is the

TOF signal of electrons obtained using a positively biased Langmuir probe. There exist two distinct peaks in the current pulse, the initial component comes almost simultaneously with the laser pulse and lasts only for a few nanoseconds. Following this a broad electron current signal is seen which extends over to several microseconds. The second peak comes well after the termination of the laser pulse. An enlarged profile of the fast electron peak alone is shown as an inset to Fig.4.1. The temporal width is only about 10 nanoseconds and it almost follows the laser beam temporal profile. The slope of the plot between the natural logarithm of the probe current and the applied probe voltage is  $e/kT$ ,  $T$  being the electron temperature,  $e$  the electronic charge and  $k$  the Boltzmann constant. Details of the evaluation of the electron temperature using Langmuir probes are given in sections 2.4. The electron temperatures corresponding to both the peaks were evaluated at a distance 0.5 cm from the target surface at a laser power density  $1.9 \times 10^{11} \text{ Wcm}^{-2}$  and it was found that corresponding to the first peak the temperature was as high as  $60 \pm 5 \text{ eV}$  while that of the second peak was only  $2 \pm 0.5 \text{ eV}$ . Thus it is clear that the energy of the first electron peak is considerably higher than the first ionization potentials of the buffer gas molecules used inside the chamber. The first ionization potentials<sup>3</sup> for  $\text{N}_2$ ,  $\text{CO}_2$ , and Ar are given in Table 4.1. Therefore the electrons constituting to the prompt peak had sufficient energy to collisionally ionize the ambient gas molecules or atoms.

Species	Ionization energy (eV)
$\text{N}_2$	15.6
Ar	15.7
$\text{CO}_2$	13.8

**Table 4.1** The first ionization potentials of gases used inside the chamber

The origin of the prompt electrons is related very much to the laser-metal interaction process. The interaction of the laser pulse with a conducting surface leads

to its absorption by the free electrons within the skin depth mostly through inverse-bremsstrahlung. The transformation of the absorbed laser energy involves thermalization within the electrons, energy transfer to the lattice, and energy losses due to electron heat transport into the target. The absorbed energy is transferred to the bulk of the material through electron-phonon interactions and hence the temperature rises abruptly and a high temperature plasma is formed. The heat penetration depth is given by  $l \sim (D\tau)^{1/2}$  where  $D$  is the diffusion coefficient and  $\tau$  the laser pulse width. Therefore, even though the absorption occurs only up to the skin depth, significant ablation occurs within the thermal conduction depth above the threshold laser power density. The energy transport into the metal can be described by the coupled nonlinear differential equations of the two-temperature diffusion model<sup>1,4</sup>

$$C_e(T_e) \frac{dT_e}{dt} = K\nabla^2 T_e - G(T_e - T_l) + P_a(r, t) \quad (4.1)$$

and

$$C_l \frac{dT_l}{dt} = G(T_e - T_l) \quad (4.2)$$

where  $C_e(T_e)$  ( $\text{J m}^{-3} \text{K}^{-1}$ ) is the electronic heat capacity,  $K$  ( $\text{W m}^{-1} \text{K}^{-1}$ ) is the thermal conductivity,  $G$  ( $\text{W m}^{-3} \text{K}^{-1}$ ) is the coefficient of heat transfer between the electrons and lattice,  $P_a(r, t)$  is the absorbed laser power density given by  $(1-R')\alpha I \exp(-\alpha z) f(t)$ ,  $\alpha$  ( $\text{m}^{-1}$ ) is the absorption coefficient,  $R'$  is the reflectivity,  $I$  ( $\text{W m}^{-2}$ ) is the laser power density,  $f(t)$  is the temporal profile of the laser pulse, and  $C_l$  ( $\text{J m}^{-3} \text{K}^{-1}$ ) is the lattice heat capacity. In eqs. (4.1) and (4.2) the thermal conductivity of the lattice phonon component is neglected. Since the electron heat capacity is much less than the lattice heat capacity, electrons can be heated to very high transient temperatures.<sup>5</sup> Numerical evaluation of the temporal variations of  $T_e$  and  $T_l$  in the case of copper showed that electron heating is very fast whereas the lattice temperature rises rather slowly.<sup>1</sup> Eesley<sup>6,7</sup> has observed



non-equilibrium electron heating in copper during picosecond laser interaction due to the initial heating of electrons well above the lattice temperature. The surface electron temperature follows the same temporal profile as the heating laser pulse and energy is transferred to the lattice.<sup>7</sup> In the nanosecond case, since the pulse width is much greater than the lattice heating time, the hot electron cloud and the lattice are in thermal equilibrium and hence  $T_e \approx T_l$ . Therefore the non-equilibrium heating of electrons may not be expected in the nanosecond case. Chichkov<sup>5</sup> et al. give a good comparison of the processes corresponding to femto, pico and nano second laser interaction with metals. A fraction of the hot electrons may escape from the interaction region before the energy is transferred to the lattice through electron-phonon interactions. The first peak in the electron TOF profile shown in Fig.4.1 should then correspond to such electrons escaping from the focal volume. The second peak obviously should be due to the plasma electrons co-existing with the laser-ablated plume which extend over to several microseconds.

The current signals from a negatively biased Langmuir probe (collecting the ions) have two distinct peaks at smaller distances and there were described in section 3.5. The first peak corresponds to the current due to the local population of the ionized ambient molecules as revealed by the time resolved spectral measurements described later in section 4.3 of this chapter. The second peak in the ion TOF profile follows almost the same time scale of the second peak in the electron TOF profile. Thus it can be inferred that the second peak in the electron TOF profile given in Fig. 4.1 corresponds to the electrons contained in the silver plasma plume.

Fig.4.2 shows the dependence of the probe current corresponding to the first electron pulse on the laser peak intensity. The probe current increases linearly with laser intensity up to about  $9.5 \times 10^{10} \text{ W cm}^{-2}$  and thereafter it saturates. While describing the surface and volume photoelectric effects which happens through

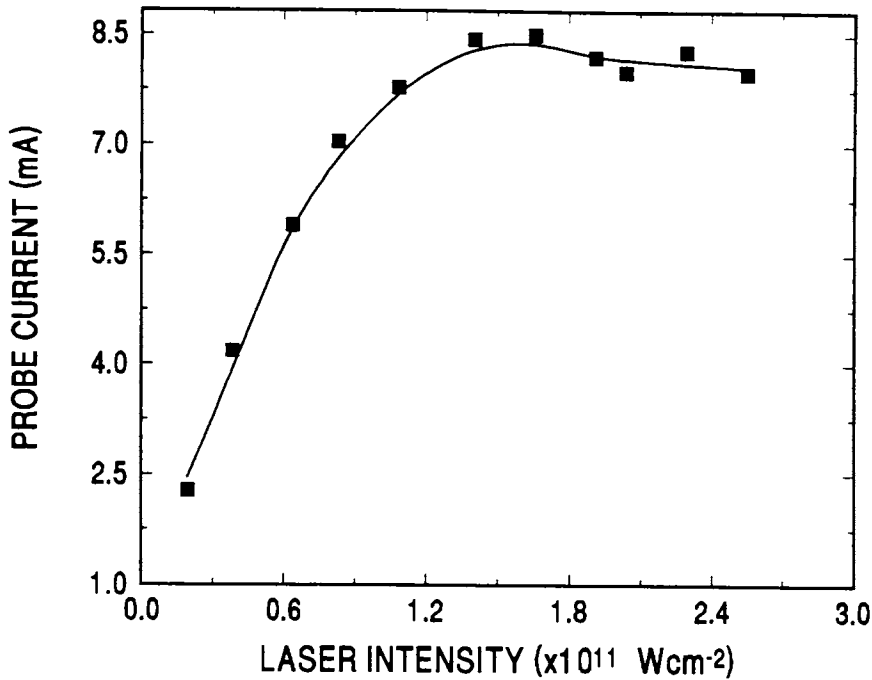


**Figure 4.2** Dependence of probe current on the laser intensity. At low laser intensities, there is a linear increase whereas at higher laser power densities the laser light is shielded off by the plasma

multiphoton excitation of metallic surfaces, many workers have shown<sup>8-10</sup> that the electron current density ( $J$ ) has a power law dependence on the input laser intensity ( $I$ ). That is,  $J \propto I^n$  where  $n$  is an integer such that  $nh\nu$  ( $h$  is the Planck's constant and  $\nu$  the laser light frequency) coincides with or slightly exceeds the work function of the material. In the present case  $n$  lies between 1 and 1.5 [obtained from the slope of the plot between  $\ln(J)$  vs  $\ln(I)$ ] which does not match with the work function of silver *viz.* 4.26 eV. Therefore multiphoton photoemission does not contribute to the prompt electron emission found in the present investigations. The saturation in electron current at higher laser intensities is due to the screening of the laser pulse. The total optical intensity available at the target is thus reduced and hence the electron number density and probe current. Russo<sup>11</sup> describes the shielding of the nanosecond laser pulse during its interaction with the pre-formed plasma as due to absorption by the atoms

and ions as they expand into the gas because of the absence of dense free electrons. But on the other hand, in the case of picosecond laser pulses, the shielding is due to absorption by free electrons. Our observation of the saturation in the prompt electron current at higher laser power densities suggests that during nanosecond laser interactions with metals, absorption by free electrons also contributes to plasma shielding.

The energy of the prompt electrons is much greater than that of laser photons and it is evident that the electrons are heated up by the laser photons by absorbing energies corresponding to several tens of photons. Such a situation is more realistically treated in classical terms by exploiting the concept of the electric field associated with the laser pulse rather than by treating it quantum mechanically. There are various processes by which electrons may be heated up due to laser absorption. The electrons could be heated up due to absorption of laser light by means of above-threshold ionization (ATI), electron oscillations in the laser electric field (ponderomotive acceleration) or could be through inverse-bremsstrahlung absorption. During ATI there should be a number of electron peaks separated by the laser photon energy.<sup>12</sup> In the present case such a behavior is not evident. Electron heating with lasers can also be described classically with the concept of ponderomotive force.<sup>13</sup> The electrons begin to *quiver* in the varying electromagnetic field and electron energy corresponding to the well known ponderomotive acceleration is given by,

$$E_p \sim 18.6 \times I_{14} \lambda_{\mu m}^2 \quad (4.3)$$

where  $I_{14}$  is the laser power density in units of  $10^{14} \text{ Wcm}^{-2}$  and  $\lambda_{\mu m}$  is the laser wavelength in micrometers. This ponderomotive energy is converted into kinetic energy as the electrons leave the light beam and the electrons are accelerated outwards. Simple calculations based on above equation show that ponderomotive forces

can play a major role in electron heating only when the intensities are high *ie.* of the order of at least  $10^{14}$   $\text{Wcm}^{-2}$ . Electron velocities of the order of  $10^9$   $\text{cm s}^{-1}$  have been reported during picosecond laser beam interaction with materials at such high laser power densities.<sup>8</sup> In the present situation, laser power densities are of the order of  $10^{11}$   $\text{Wcm}^{-2}$  and the ponderomotive energy estimated from Eqn. 4.3 is only  $\sim 0.2$  eV which does not match with the measured energy of the prompt electrons. Thus electron heating due to ponderomotive effects may not contribute substantially in the present case. Therefore the most probable heating mechanism is that due to the absorption of the laser radiation through inverse-bremsstrahlung which is described in section 3.5.3. In an experiment with graphite as the target<sup>14</sup> electron kinetic energies in excess of 15 eV were observed and the electron heating was attributed to collisional absorption of laser light by free electrons through inverse-bremsstrahlung.

#### 4.2 Comparison of TOF profiles of different species

All the investigations which led to the observations given in the previous section *de facto* originated from the TOF measurements of various species present in the plasma. Ambient molecules which have only random thermal speed are usually assumed to be stationary compared to the highly directed velocities of ablated species. Also, the main excitation and ionization mechanism for ambient molecules is the collision with electrons and the ablated species. Therefore, when spectral emissions are observed, one should expect a temporal coincidence between the arrival of the ablated species and the excitations of the ambient species. But to our surprise, the emission profiles of the ambient molecules or atoms were very sharp and appeared very early compared to that of silver atoms or ions. It is very clear from the TOF profiles shown in Fig.4.3 that the atomic and molecular emissions from the *ambient gas* are very sharp when compared to that of silver. The temporal emission profiles of ambient gases are well separated from that of silver. The most distinct feature of the temporal emission profile of Argon is that it has a twin peak distribution. The second peak appears during the rising part of the

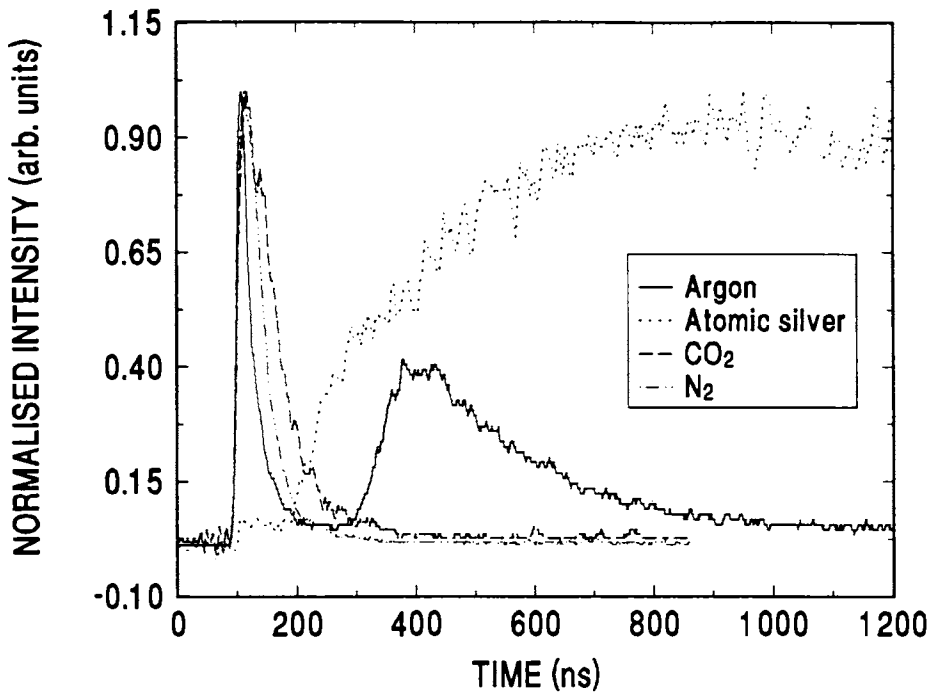


Figure 4.3 The temporal profiles of various species present in the plasma

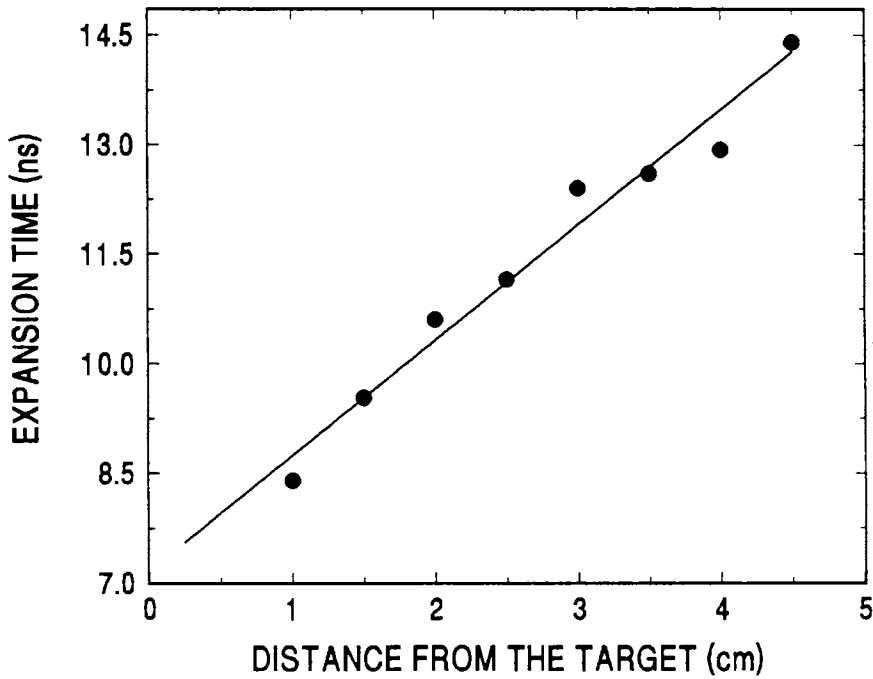


Figure 4.4 Variation of the time-of-flight of electrons with distance from the target. Expansion time increase linearly with distance from the target.

silver TOF profile. In section 3.2 we have shown that the silver plasma actually forms a shock front with cylindrical symmetry at relatively high pressure. Therefore the second TOF peak corresponds to the ionization at the shock front i.e., the propagating boundary between the ambient gas and the plume. The second peak is not apparent in the case of  $N_2^+$  or  $CO_2$  probably due to the difference in the collisional excitation/ionization cross-sections. Also the profiles shown in the figures suggest that with the aid of time-resolved spectroscopy one may in principle separate the spectrum of ambient molecules from that of silver plasma by adjusting the gate widths and delays of a boxcar averager.

Now the question arises as to how the emission from the ambient molecules or atoms appears so much earlier than the silver plasma. This is a puzzling situation and there exist three relevant possibilities *viz.* the ionization by UV absorption from the plasma core, the ionization due the multiphoton absorption of the laser light itself and the collisional ionization of ambient molecules due to prompt electrons. The relative importance of these three possibilities for the excitation of ambient gas molecules is explored in the following sub-sections.

#### 4.2.1 UV absorption from the plasma core

The ambient molecules may be excited and ionized by absorbing the ultraviolet radiation arising from the plasma core. For direct ionization through UV absorption we require photons having energies greater than  $\sim 15$  eV (*i.e.* the ionization potentials of the buffer gases used). With the existing experimental setup which has very poor response in the vacuum UV, we could not observe such photons, but indirectly we tried to establish that UV absorption may not be a likely process for ambient ionization in the present context. Fig.4.4 shows the plot between the distance from the target and the time-of-flight of prompt electrons. The time-of-flight ( $t$ ) for the prompt electrons increases with distance ( $R$ ) from the target even though the variation is not strictly linear. The time-of-flight is related to the distance from the target as  $t \propto R^{0.34}$  which is shown by the solid curve in

Fig.4.4. This eliminates the possibility of ambient ionization and electron production by the absorption of UV radiation since with the typical length scales inside the chamber, such an absorption and the subsequent ionization should be instantaneous. Also it is not likely that the UV radiation for the plasma core to have very sharp temporal profiles. Therefore if there is appreciable amount of electron production through UV absorption, the sharpness in the prompt electron TOF profile cannot be expected.

#### 4.2.2 Direct multiphoton absorption and ionization

Another possibility for the ionization of the ambient gas molecules is through the direct multiphoton absorption of laser light resulting in gas breakdown. Similar to the argument given in section 4.2 in connection with the heating up of prompt electrons, the growth rate of electron number density should be proportional to the  $n^{\text{th}}$  power of laser power density ( $I$ ). After neglecting electron contribution from multiple ionization, it can be assumed that the production of one electron results in an  $\text{N}_2^+$  molecule. Since the emission intensity ( $J$ ) is proportional to the number of emitting molecules, a plot between  $\ln(J)$  and  $\ln(I)$  should give a slope  $n$  in the case of  $n$ -photon absorption.<sup>11,16,17</sup> In the case of Nitrogen ions, the slope  $\sim 1$  which rules out the possibility of multiphoton absorption since at least 12 photons are required for the direct multiphoton ionization of nitrogen present inside the plasma chamber. This fact is partially supported by the measurement of electron density at various distances from the target to be detailed in section 4.3.2 later in this chapter.

#### 4.2.3 Collisional ionization due to prompt electrons

Another possibility for ambient excitation and ionization is that due to the collisions between the ambient species and the prompt electrons. The energy of prompt electron

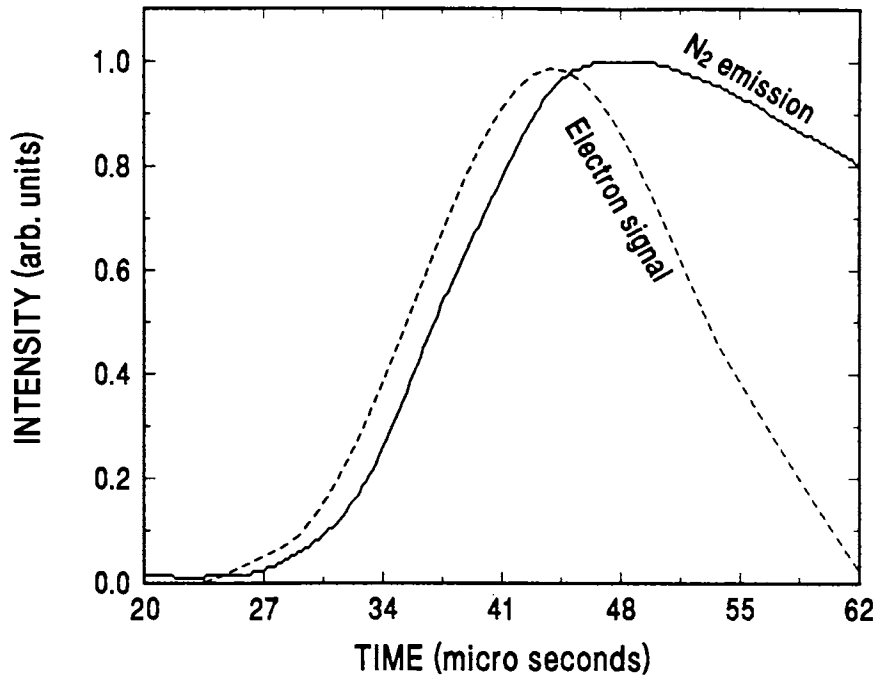


**Figure 4.5** Plot showing the temporal coincidence of the prompt electron pulse and the nitrogen emission from the plasma. The relaxation time for  $N_2$  emission is very much larger than the temporal width of the electron pulse.

pulse is much greater than the first ionization energy of the ambient species and it is very likely that the species become ionized due to collisions. The temporal pulse of  $N_2^+$  emission almost coincides with the occurrence of this first electron current pulse as shown in Fig.4.5. The decay time of the  $N_2^+$  emission profile is found to be considerably larger than that of the width of the exciting electron pulse since various life times of the excited states are involved in the spectral emission process.

### 4.3 Time-resolved spectroscopy

Time-resolved spectroscopy in laser-produced plasmas have been the subject of many research articles.<sup>18-22</sup> The technique has the unique advantage that it presents the individual atomic, ionic and molecular processes in a sequential manner in the time domain. Usually in high density laser plasmas, during short time delays the spectrum is



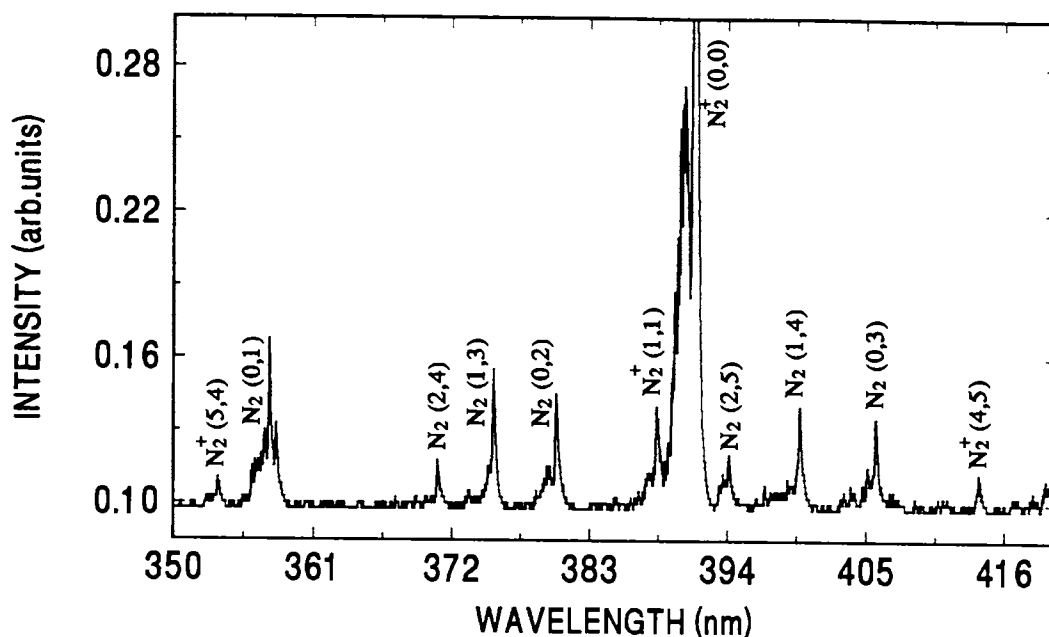


**Figure 4.6** Time resolved spectrum with nitrogen as ambient medium recorded with a boxcar gate delay of 0 ns and gate width 40 ns. The spectrum shows emission from background gas molecules only and characteristic emission from silver is not seen during initial small time delays

dominated by the continuum emission and as the plasma cools down the signatures of atomic and ionic emissions begin to appear.<sup>17</sup> As a part of present investigations, time-resolved spectra were recorded in the visible region with three different ambient gases, viz. nitrogen, argon and carbon dioxide.

#### 4.3.1 Nitrogen as ambient gas

The TOF profiles which has been drawn in Fig.4.3 show that the emission from the ambient gas occurs almost coincident with the laser pulse, *i.e.* very close to the laser pulse. Therefore time-resolved spectrum in the range 350 - 800 nm is recorded with the boxcar gate delay 0 ns and width 40 ns for a nitrogen ambient atmosphere. A representative spectrum in the range 350 nm to 420 nm is shown in Fig.4.6. The most

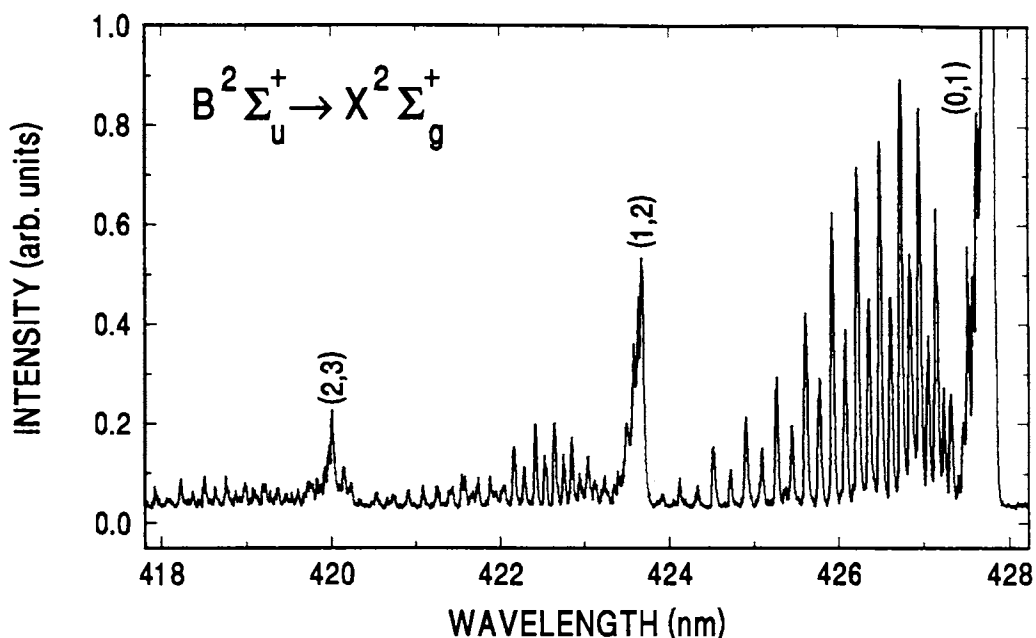


**Figure 4.7** Time resolved spectrum from the silver plasma in nitrogen ambient with gate delay 0 ns and gate width 40 ns. Clearly resolved rotational structure with intensity alternations is seen.

prominent features in the emission spectrum are due to the  $N_2$  and  $N_2^+$  molecular systems. The spectrum shows emission bands corresponding to emissions from  $N_2$  and  $N_2^+$  and does not have any emission which is characteristic of the silver atoms or silver ions coming out of the target. Since the ground state of  $N_2$  is a singlet, the direct excitation to the triplet that give rise to the second positive system is normally forbidden except through the mechanism of energy exchange.<sup>23</sup> A high resolution spectrum giving the rotational fine structure with alternate half intensities of the  $\Delta v = -1$  band of  $N_2^+$  with band head at 427.8 nm is shown in Fig.4.7. Such intensity alternations can be observed for homonuclear molecules due to the difference in statistical weights for even and odd numbered rotational levels. The intensity ratio is given by  $(I+1)/I$  where  $I$  is the nuclear spin quantum number.<sup>24</sup> The nuclear spin of the  $N_2^{14}$  isotope is one and thus the intensity ratio for alternate lines should be 2:1.

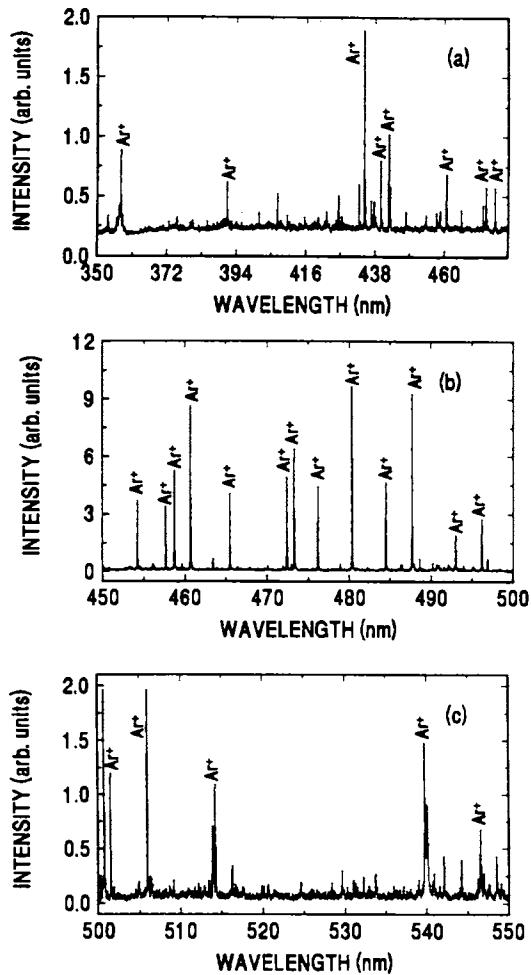


**Figure 4.8** Time resolved spectrum with argon as the ambient gas with gate delay 0 ns and gate width 40 ns. The spectrum shows lines mostly from singly ionized argon

Slight deviations from 2:1 intensity alternations in the recorded spectrum is due to the P and R branch overlap.<sup>25,26</sup>

### 4.3.2 Argon as ambient gas

With an argon ambient, the medium is almost fully ionized and the spectrum is dominated by the singly ionized species as shown in Figs. 4.8(a-c). Therefore it is considered that the laser-plasma is preceded by a partially ionized ambient plasma. The individual emission lines are found to exhibit stark broadening resulting from the electric field due to high electron density. Hence the width of the Stark-broadened profiles can be used for the determination of the density of prompt electrons.<sup>27</sup> Fig.4.9 shows the stark-broadened profile of the  $\text{Ar}^+$  emission line at 480.6 nm. The solid line in Fig.4.9 is a Lorentzian fit to the observed data points with a FWHM of 0.02 nm. The

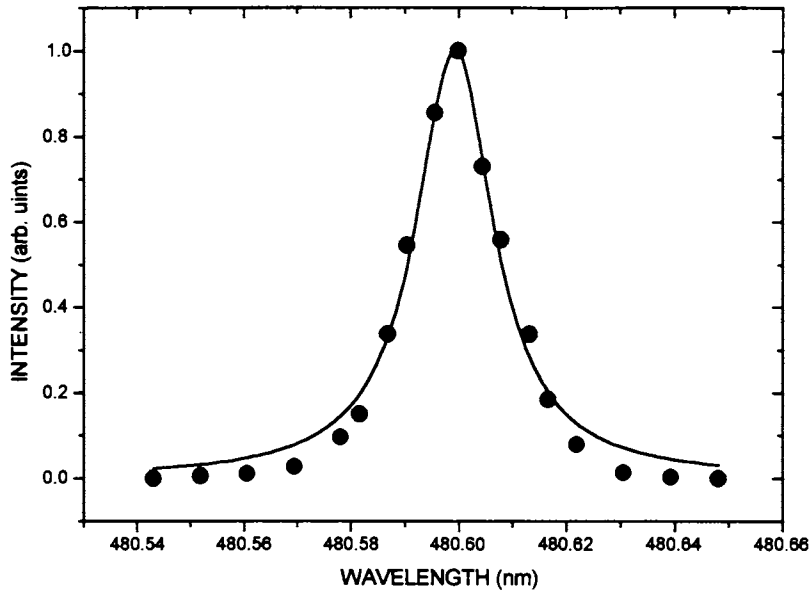


**Figure 4.9** The stark-broadened profile of the line from  $\text{Ar}^+$  line at 480.6 nm. The solid line is a Lorentzian fit to the data points with FWHM .0.02 nm

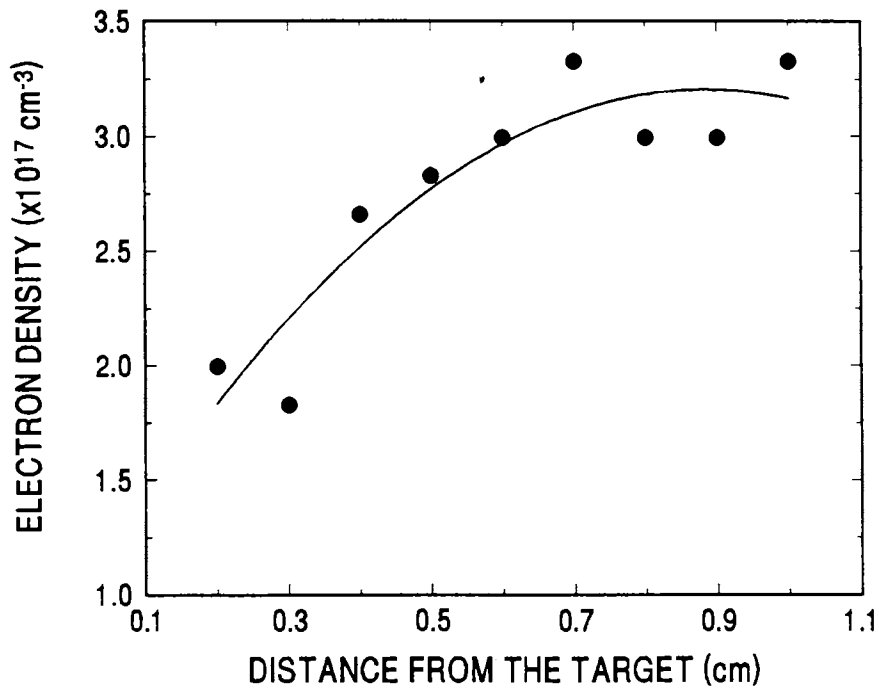


**Figure 4.10** Variation of prompt electron density as a function of distance from the target at a pressure of 0.27 mbar. The density increases with distance from the target indicating electron generation due to collisions

electron number density ( $N_e$ ) is related to the FWHM of *neutral* atoms through the relation,<sup>28</sup>

$$\Delta\lambda_{1/2}(nm) = 2W\left(\frac{N_e}{10^{17}}\right) + 3.5A\left(\frac{N_e}{10^{16}}\right)^{1/4}\left[1 - \frac{3}{4}N_D^{-1/3}\right]W\left(\frac{N_e}{10^{17}}\right) \quad (4.3)$$

where  $W$  is the electron impact parameter,  $A$  is the ion broadening parameter, and  $N_D$  is the number of particles in the Debye sphere given by

$$N_D = \frac{4}{3}\pi NL_D^3 \quad (4.4)$$

Here  $L_D$  is the Debye length. The coefficients  $W$  and  $A$  are independent of density and are slowly varying functions of density. In the case of *singly ionized* species the numerical coefficient  $3/4$  is replaced<sup>28</sup> by 1.2. In eqn.(4.3), the first term gives the contribution from electrons and the second term is the ion correction factor. Neglecting the ion correction, the FWHM is given by,

$$\Delta\lambda_{1/2}(nm) \approx 2W\left(\frac{N_e}{10^{17}}\right) \quad (4.5)$$

The density of the prompt electron pulse as a function of distance from the target is evaluated using the stark-broadened emission line profile of  $\text{Ar}^+$  at 480.6 nm using eqn. (4.5) and it was found that the density increases with distance from the target. The variation of the electron density with distance is shown in Fig.4.10. Near the target, the electron density is  $1.8 \times 10^{17} \text{ cm}^{-3}$  and at 1 cm it is  $3.4 \times 10^{17} \text{ cm}^{-3}$  showing a steady increase in the electron density with distance from the target. Such an increase in electron density with distance is noteworthy as it precludes other causes such as UV absorption and multiphoton processes for the ionization of ambient molecules. Such an increase in electron density is thus expected since the ionization of each argon atom

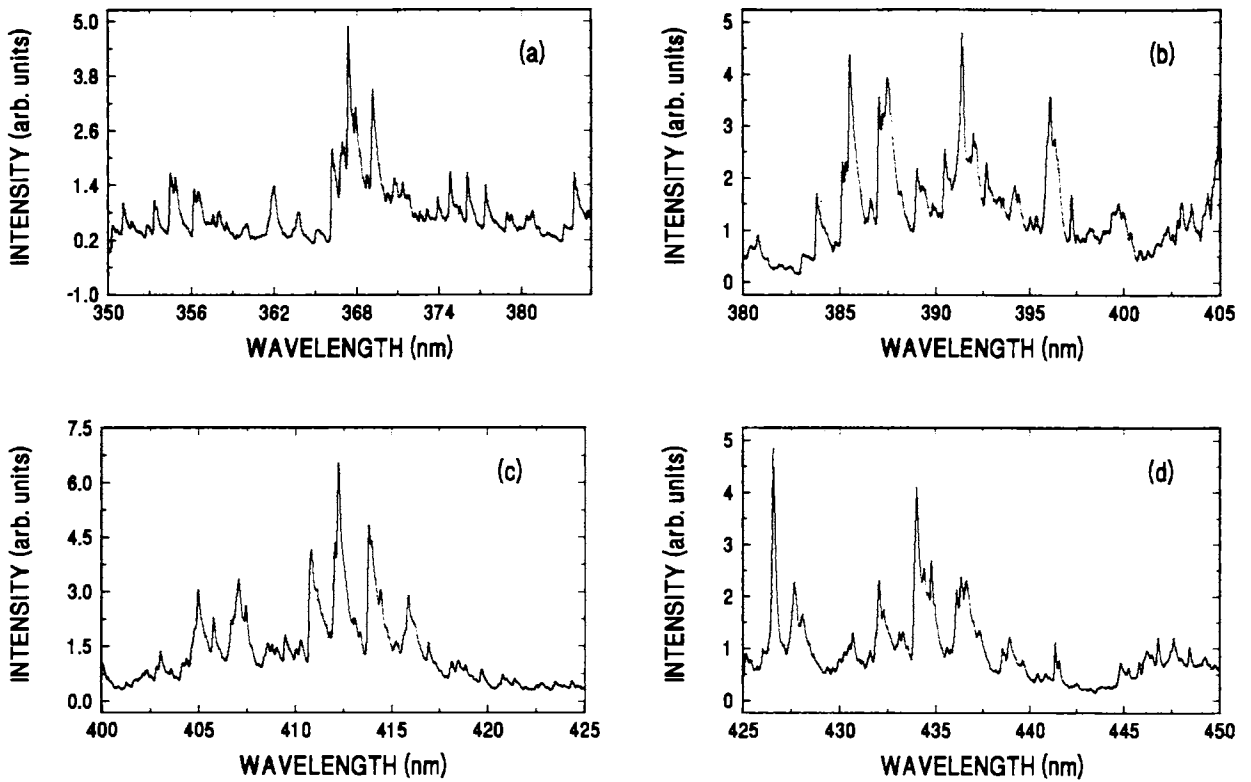


**Figure 4.11** Spectrum of CO<sub>2</sub> at a gate delay of 0 ns and gate width 40 ns. The spectrum shows a large number of bands corresponding to emission from CO<sub>2</sub>

produces an additional electron, ie.  $\text{Ar} + e \rightarrow \text{Ar}^{+*} + 2e$ . The electron density attains a steady state value after about 0.7 cm from the target surface.

### 4.3.3 Carbon dioxide as ambient gas

Pure spectroscopy of the well studied molecules like N<sub>2</sub> or CO<sub>2</sub> was not the prime theme of our investigations. The major aim is to demonstrate how the collisions of prompt electrons with molecules and the resulting excitations can be utilized in collision spectroscopy. We here get spectra only of ambient gas molecules which are well resolved and separated in time from that of the actual laser-plasma. The spectra recorded with CO<sub>2</sub> as the ambient gas is given in Figs. 4.11 (a-d) which cover the region of 350-450 nm. Unlike the case of N<sub>2</sub> or Ar, the spectral emission is primarily from neutral CO<sub>2</sub> molecules. In other words, CO<sub>2</sub> molecules are not ionized or dissociated

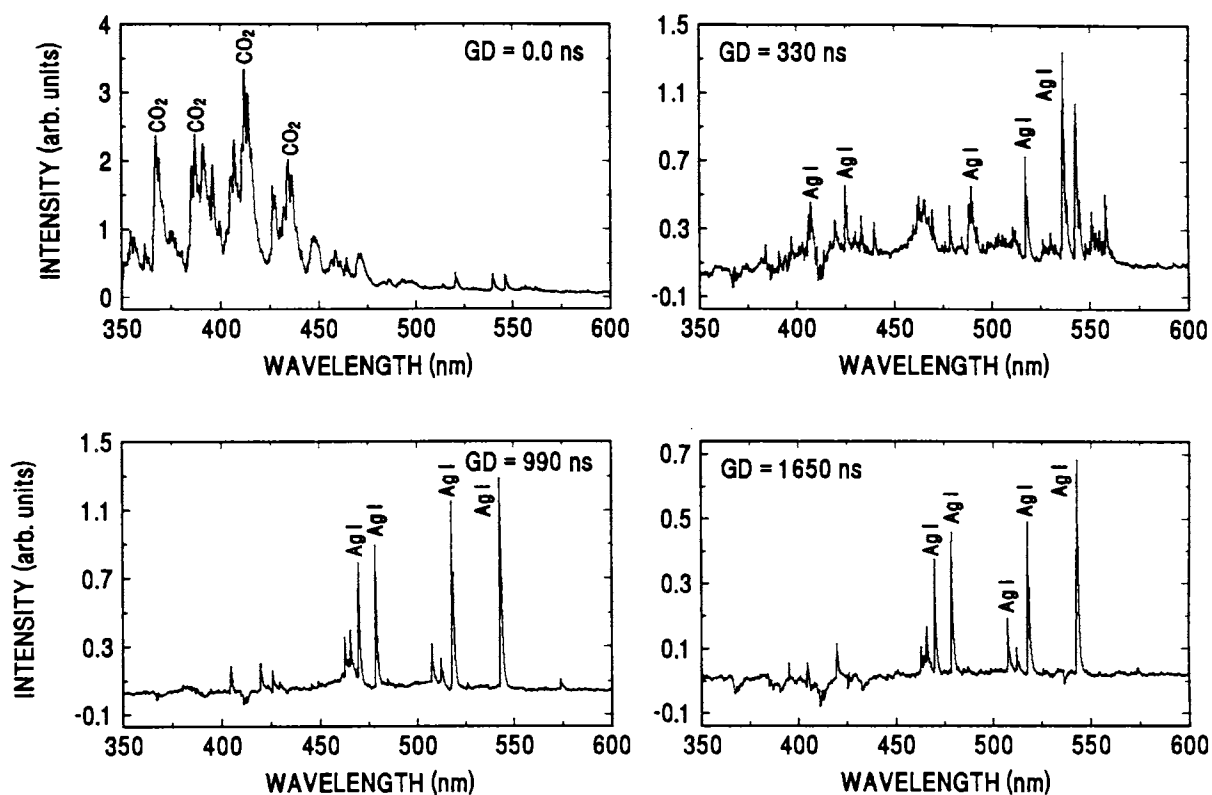


**Figure 4.12** Time resolved spectrum from silver plasma

due to electron impact as evidenced from the spectra. The present studies based on time-resolved spectroscopy show that the prompt electrons can be effectively used as sources of pulsed electron beams which in turn can be used in electron-molecule collisional excitations.

In order to emphasize the importance of time resolved measurements for obtaining well isolated spectra of ambient molecules, emission spectra with higher time delays also were recorded. Fig.4.12 (a-d) shows the spectrum from the silver plasma at four different time delays at a distance 0.5 cm from the target with CO<sub>2</sub> as the ambient gas. At a gate delay of 0 ns, the spectrum is purely that of CO<sub>2</sub> as shown in Fig.4.12(a). As the delay is increased, the spectral emissions from silver atoms and ions begin to appear and the spectrum of CO<sub>2</sub> disappears.

### **4.3 Summary**

In this chapter, measurements related to the production of high energy electron pulses during nanosecond laser interaction with a metal target have been described. The electron pulses thus generated are found to cause ionization and the excitation of atoms and molecules in the ambient gas. To the best of our knowledge laser heated prompt electrons have not yet been used for ambient molecular excitation-relaxation studies in a systematic way. Electron-molecule, electron-atom collisions, ionization and the corresponding energy transfer have acquired considerable interest in recent times. The electron-vibration and electron-rotation energy transfer and the determination of the corresponding rate constants assume particular importance in atmospheric science, astronomy and in high velocity plasma flows.<sup>29</sup> Most of the studies related to the electron-vibration energy transfer is theoretical and there is need for the development of appropriate experimental techniques to study the energy exchanges. The temporal width of the electron pulse assumes prime importance in such measurements. With the laser generated electron pulses as sources of high-energy electron beams such measurements can be extended to a wider domain. The role of free electrons hitherto was considered as appreciable only in picosecond laser interactions. An important application which may arise in this context is in the rotational-vibrational spectroscopy of volatile molecules. The small temporal width of the electron pulses can effectively be used for vibrational relaxation experiments to measure the various rate constants. Also with appropriate electron optics the electron pulses can be shaped into a perfect beam and the energy of electrons can be controlled as desired. Moreover the observation of high-current prompt electron emission sheds more light into its role on plasma shielding during nano-second laser beam interaction with solids. We believe that pico-second laser pulse interaction with metallic surfaces can produce electron beams which has a temporal width of pico-second duration, the realization of which is extremely difficult in conventional techniques of electron beam generation.



## References

- <sup>1</sup>Elsayed – Ali H E, Norris T B, Pessot M A and Mourou G A *Phys. Rev. Lett.* **58** (1987) 1212
- <sup>2</sup>Eliezer S and Hora H *Phys. Rep.* **172** (1989) 339
- <sup>3</sup>Weast R C (Ed.) (1988): *CRC Handbook of Chemistry and Physics* (CRC Press, Florida)
- <sup>4</sup>Fujimoto J F, Liu J M, Ippen E P and Bloembergen N *Phys. Rev. Lett.* **53** (1984) 1837
- <sup>5</sup>Chichkov B N, Momma C, Nolte S, Alvensleben F von, Tünnermann A *Appl. Phys. A* **63** (1996) 109
- <sup>6</sup>Eesley G L *Phys. Rev. Lett.* **51** (1983) 2140
- <sup>7</sup>Eesley G L *Phys. Rev. B* **33** (1986) 2144
- <sup>8</sup>Farkas G and Toth C *Phys. Rev. A* **41** (1990) 4123
- <sup>9</sup>Moustaizis S D, Tatarakis M, Kalpouzios C and Fotakis C *Appl. Phys. Lett.* **60** (1992) 1939
- <sup>10</sup>Hauser Thomas, Werner Scheid and Hora H *Phys. Lett. A* **186** (1994) 189
- <sup>11</sup>Russo R E *Appl. Spectroscopy* **49** (1995) 14A
- <sup>12</sup>Freeman RR, McIlrath TJ, Bucksbaum PJ and Bushkamsky M *Phys.Rev.Lett.* **57** (1986) 3156
- <sup>13</sup>Kibble T W B *Phys. Rev.* **150** (1996) 1060
- <sup>14</sup>Cronberg H, Reichling H, Broberg E, Nielsen H B, Mathias E and Tolk N *Appl. Phys. B* **52** (1991) 155
- <sup>15</sup>Baravian G, Godart J and Sultan G *Phys. Rev. A* **25** (1982) 1483
- <sup>16</sup>Gamaly E G *Laser and Particle Beams* **12** (1994) 185
- <sup>17</sup>Varier Geetha K, Issac Riju C, Harilal S S, Bindhu C V, Nampoore V P N and Vallabhan C P G *Spectrochimica Acta B* **52** (1997) 657
- <sup>18</sup>K L Saegner *J. Appl. Phys* **66** (1992) 4435
- <sup>19</sup>Pappas D L, Saegner K L, Cuomo J J, and Dreyfuss R W *J. Appl Phys.* **72** (1992) 3966
- <sup>20</sup>Lowndes D H, Geohegan D B, Puretzky A A, Norton D P and Roulean C M *Science* **273** (1996) 893
- <sup>21</sup>Kerdja T, Abelelli S, Ghobrini D and Malik S *J. Appl. Phys.* **80** (1996) 5365
- <sup>22</sup>Riju C Issac, Harilal S S, Bindhu C V, Varier Geetha K, Nampoore V P N and Vallabhan C P G *Spectrochimica Acta B* **52** (1997) 1791
- <sup>23</sup>Thomas E W *Excitations in heavy particle collisions* (Wiley Interscience, New York, 1972)
- <sup>24</sup>Herzberg G *Spectra of diatomic molecules* (D van Norstrand Company Inc., New York, 1961) p.209
- <sup>25</sup>Lowe R P and Fergusson H I S *Proc. Phys. Soc. (London)* **85** (1965) 813
- <sup>26</sup>Moore Jr. J H and Doering J P *Phys Rev* **174** (1968) 178
- <sup>27</sup>Griem H R *Plasma Spectroscopy*, (McGraw Hill, New York, 1964)
- <sup>28</sup>Bekefi G (Ed.) (1976): *Principles of laser plasmas*, John Wiley & Sons, New York
- <sup>29</sup>Bourden A and Vervish V *Phys. Rev. E* **55** (1997) 4634

# Angular distribution of ablated species

## **Abstract**

The angular distribution of the ablated species in a laser produced silver plasma is obtained from the measurement of optical density of thin films deposited on to glass substrates kept perpendicular to the plume. There is a sharp variation in the thickness away from the film center due to asymmetries in the plume. The horizontal and vertical distributions have different angular spread when the laser pulse is incident on the target at  $45^\circ$  with the target normal.

Pulsed laser deposition (PLD) of various materials is effectively being used for thin film preparation during the past few decades.<sup>1-10</sup> However the full utilization of laser ablation in single element thin film deposition has not been possible due to various reasons.<sup>3</sup> The successful deposition of stoichiometric thin films by the method of PLD demands the characterization of the ablation plume with temporal, spatial and angular resolutions. The presence of an ambient gas, for example, alters the properties of the plume significantly.<sup>11,12</sup> At high ambient pressure, the plasma plume has a large angular spread due to scattering but in vacuum this scattering is negligible. Geohegan and Purezky<sup>13</sup> describe the broadening of the time-of-flight profile in yttrium plasma at high pressure levels due to collisions with the background gas molecules. In vacuum, they found a narrow velocity profile for ionic species. Their observations have also revealed a fast and a slow component at high ambient pressure while only the fast component persists in vacuum. The slower component emerges due to the slowing down of the plume by ambient gas molecules. Such double peak structure appears only for limited distances and pressures.

Gas phase collisions inside the plasma play a major role in determining the spatial, temporal and angular distribution of ablated species. When the particle densities

are high enough, collisions induce the formation of a thermalization layer called Knudsen layer (KL) within a few mean free paths from the target surface. Investigations on the formation of such a layer in laser produced plasmas have been done by Kelly and others.<sup>14-20</sup> The formation of the KL results in stopped or backward moving material close to the target and strongly forward peaked velocity distributions away from the target. The '*half range*' Maxwellian velocity distribution is changed over to a '*full range*' Maxwellian distribution revealing the presence of backward moving particles. The backward moving particles are either re-condensed or reflected from the target surface.<sup>21</sup> The KL formation is followed by a more forward peaked particle flux with an unsteady adiabatic expansion (UAE) of the plasma. Since the particle flux in a laser produced plasma is highly anisotropic, the proper understanding of the angular distribution assumes vital importance in thin film deposition. This chapter deals with the angular distribution of the ablated particle flux in a laser produced silver plasma.

The experimental configuration adopted is the same as that described in previous chapters. The plasma is produced in an argon ambient using the fundamental output of the Nd:YAG laser with pulse width 10 ns and repetition rate 10 Hz. Laser beam hits the target surface at an angle of  $45^\circ$  for film deposition. The chamber is connected to diffusion and rotary vacuum pumps and an ultimate low pressure of  $10^{-5}$  mbar is obtained in the system.

### 5.1 Angular dependence of ablated species

When a laser plasma is considered under the context of thin film deposition, there exists two different angular distributions which are (i) the source angular distribution and (ii) the film thickness distribution. To have a better understanding of the process, the schematic of the geometry of the deposition process is given in Fig.5.1. A source angular distribution which has a general form  $f(\theta) = \cos^p \theta$  would yield a thin film thickness profile  $D(\theta) = \cos^{p+3} \theta$  when the film is deposited on a planar substrate.<sup>8</sup> Angular

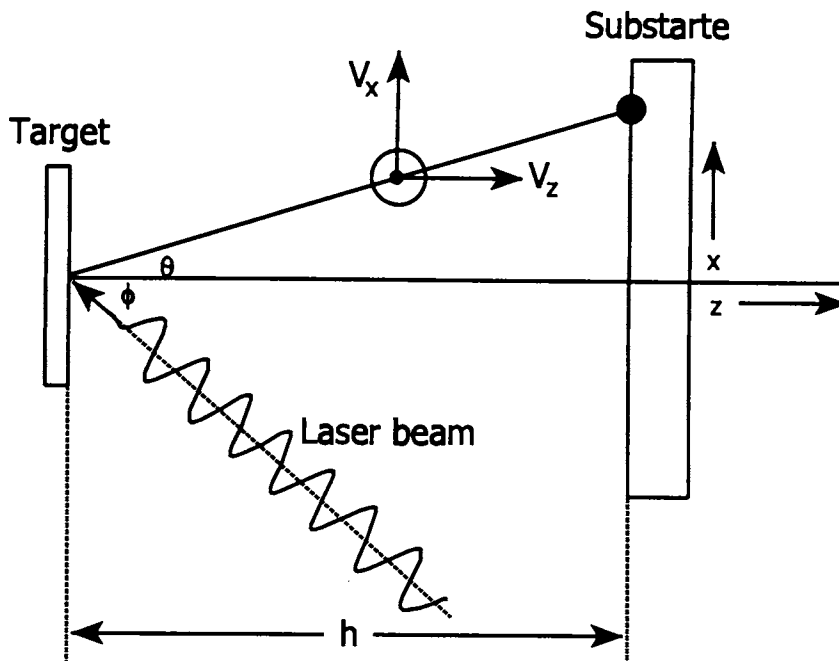


**Figure 5.1** Schematic for pulsed laser deposition. The laser is incident on the target at an angle  $\phi$  with respect to the target surface normal. The vaporized particles travel to the substrate which is separated by a distance  $h$  from the target.  $\theta$  is the effective angle of emission for particles arriving at a position  $p$ . [The figure is reproduced from K L Saegner *Processing of Advanced Materials 2* (1993) 1]

distributions of the ablated species are usually measured either by monitoring the ion flux using electronic probes or from the thickness profile of the deposited film assuming a unity sticking coefficient to the substrate.<sup>8</sup> Film based methods for determining the angular distribution use the substrate as a time integrated flux detector. The two major assumptions which are used in film based methods are (i) the sticking coefficient is unity for all types of species and (ii) there is no resputtering of the film by the energetic particle flux which strikes the substrate. Here we follow the method used by Afonso<sup>22</sup> et al. where instead of measuring the thickness, the optical density is monitored as a function of the distance from the film center. The films are deposited on glass substrates ( $7.5 \times 1.75 \text{ cm}^2$ ) at room temperature and under various pressure conditions. In most cases, the deposited film is partially transparent and electrically nonconducting depending on the target-substrate distance and the ambient pressure conditions. The

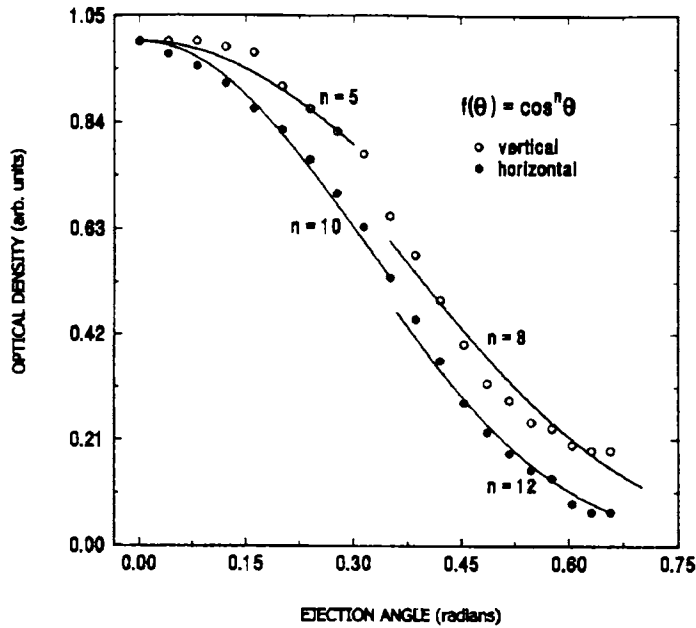


**Figure 5.2** The optical density of the film as a function of ejection angle at a pressure of  $2 \times 10^{-5}$  mbar. The observed data points do not fit exactly into a single  $\cos^n \theta$  curve.

optical density of the film as a function of the distance from the film center is measured using a microdensitometer.

As has been seen from section 1.3 (Chapter 1), particle collisions very much affect the angular distribution of the ablated species. When the minimum number of collisions is greater than at least three per particle, KL is formed in a region within a few mean free paths from the target surface.<sup>16</sup> The exponential part of the velocity distribution change from  $\exp(-mv_x^2/2kT_s)$  to  $\exp[-m(v_x - u_K)^2/2kT_K]$  where  $u_K$  is the positive flow velocity given by<sup>20</sup>  $u_K = (\gamma k T_K / m)^{1/2}$ . Here  $m$  is the mass of the species,  $T_s$  is the surface temperature and  $T_K$ , the temperature of the species which is lower than  $T_s$ . Also the angular distribution is more forward peaked than those in the usual thermal sputtering. At higher pressures compared to vacuum, the collisions among the particles are more frequent and the KL is formed.

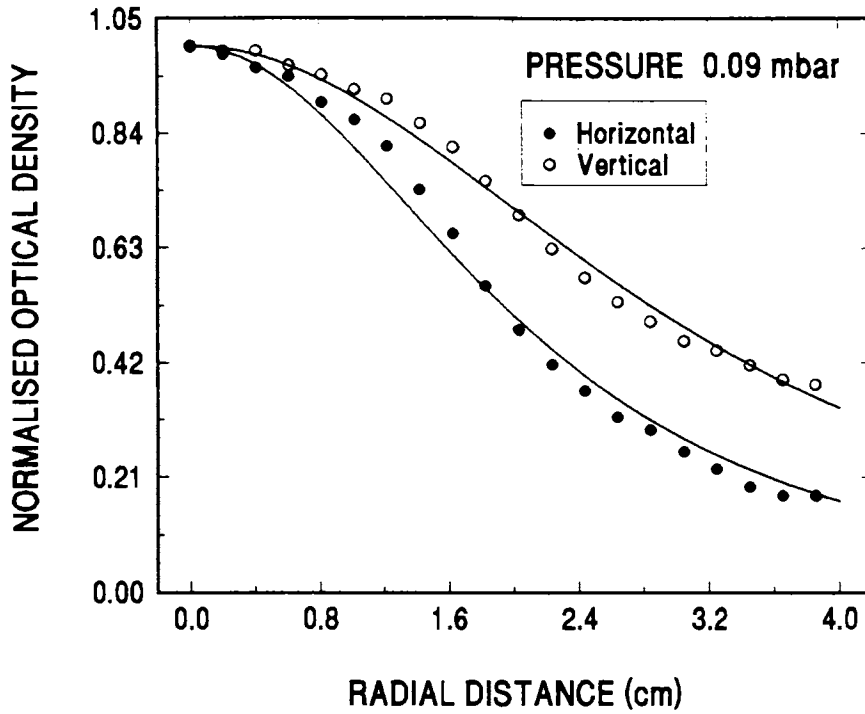
The optical density of the deposited film as a function of the distance from the target and as a function of the ejection angle is plotted. Fig.5.2 shows the optical density as a function of the ejection polar angle at a pressure of  $2 \times 10^{-5}$  mbar. The observed data points do not fit exactly into a single  $\cos^n \theta$  curve which is shown by solid lines in the figure. The horizontal and vertical profiles are different due to the reasons which are illustrated in the following paragraphs. Initially  $n = 5$  in the vertical direction which changes over to  $n = 8$  at an angle  $\sim 0.3$  radians.  $n = 10$  in the vertical direction changes over to  $n = 12$  at an ejection angle of  $\sim 0.37$  radians. The optical density drops as if there exists a sharp boundary.

Fig.5.3 shows the plot of optical density as a function of the distance from film center at a background pressure 0.09 mbar at a distance of 6 cm from the target. The film is nonconducting and weakly transmitting at optical wavelengths. Both the vertical and the horizontal distributions are measured and it is clear from the figure that both are significantly different from each other. The angular distribution is narrow along the horizontal direction and much broader in the vertical direction. Fig.5.4 shows the thickness profile as a function of distance from the film center at reduced pressure, viz.  $2 \times 10^{-5}$  mbar. Here the boundary effect is more predominant. It may be because the conditions are more favorable to adiabatic plasma expansions and the ablative species becomes more forward directed. Also at reduced pressure the scattering of the species while interacting with the ambient gas molecules is less.

An analytic expression for the film thickness distribution is given by<sup>25</sup>

$$D(x,0,L) = \frac{D_0}{\left[ \left( k_x x / L \right)^2 + 1 \right]^{3/2}} \quad (5.1)$$

where  $D_0 = n_0 k_x k_y / 4\pi L^2$ ,  $k_x = V_z / V_x$ ,  $k_y = V_z / V_y$ .  $V_a(a=x,y,z)$  are the velocities in the three different axes,  $z$  being the propagation axis. Here  $n_0$  is the total number of particles in the



**Figure 5.3** Figure showing the plot of optical density as a function of distance from the film center at a background pressure of 0.09 mbar. The solid line gives a theoretical fit to the observed data points.

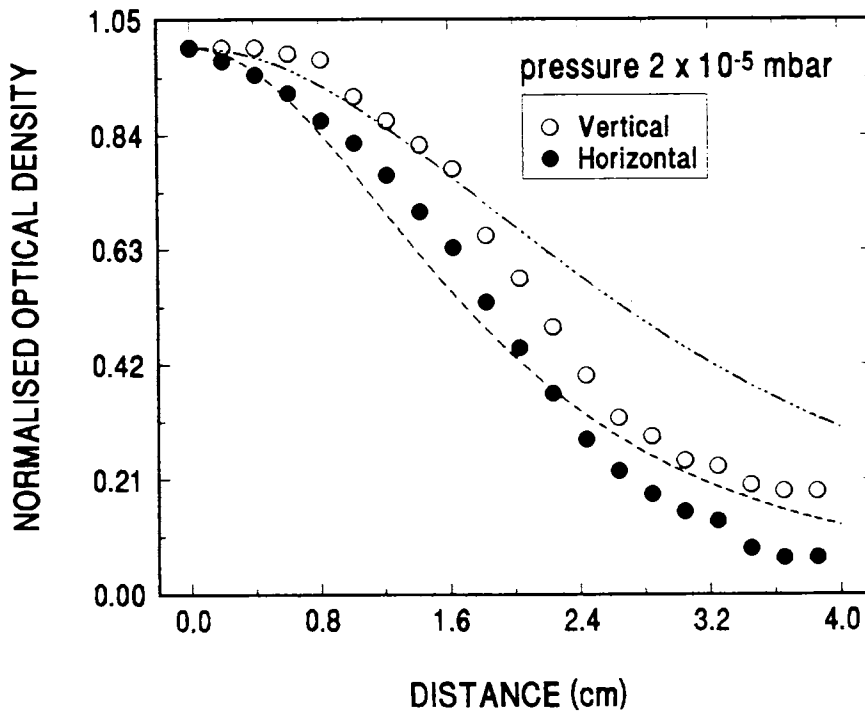


**Figure 5.4** Figure showing the plot of optical density as a function of distance from the film center at a background pressure of  $2 \times 10^{-5}$  mbar. The solid line gives a theoretical fit to the observed data points.

plasma and  $L$  is the target-substrate distance. Similarly in the  $y$ -direction  $x$  and  $k_x$  are replaced by  $y$  and  $k_y$  in the above expression. The dotted lines in Fig.5.3 show the theoretical fit to the data at 0.09 mbar for  $k_x=1.935$  for horizontal direction and  $k_y = 1.315$  for the vertical. The values of  $k_x$  and  $k_y$  show that the vertical velocity is  $\approx 1.46$  times that of the horizontal. For  $45^\circ$  angle of incidence, the major axis is  $\sqrt{2} = 1.414$  times greater than the minor axis and according to the theory of adiabatic plasma expansion, the velocities also should have the same ratio.<sup>24</sup> The ratio  $k_y/k_x \approx 1.46$  which is in close agreement with the value 1.414. In vacuum  $k_x/k_y \approx 1.56$ , deviating from the predicted value. Even though the dotted lines show a nearly close agreement with the data points in the vicinity of the film center as well as at the wings, there exists an abrupt change in the thickness distribution in between. Near the film center the thickness is more uniform than predicted by eqn.5.1 and beyond a certain distance the change is steeper. This means that there exists an emission solid angle inside which the particle flux is high. The outer region is rarer and forms a halo. The deposition rate from the inner region is more than that from the outer halo. This is an indication that the energetic particles are more favorable for thin film growth.

The peak velocities of silver atoms decrease and the velocity spread  $V_s$  increases as the pressure goes down as shown in Fig. 3.1 (Chapter 3). Velocity spread is a clear demonstration of the randomness of particle motion. The ratio  $V_s/V_p = \tan \theta$  gives the mean angle of particle emission.<sup>26</sup> The mean angle of particle emission,  $\theta$ , is determined using the TOF signals at two pressures using the above formula and the values obtained are  $\approx 35^\circ$  at 0.09 mbar and  $\approx 44^\circ$  at  $2 \times 10^{-5}$  mbar. Accordingly the angular spread of the excited silver atoms is more at reduced pressure. Therefore, the angular spread of the ablated species as determined from film based methods significantly differs from the above data. Even though the neutrals in the plasma have an angular spread (FWHM) of  $44^\circ$ , the film based methods show that the spread  $39^\circ$  at  $2 \times 10^{-5}$  mbar. This suggests that excited neutral silver atoms are newly generated at



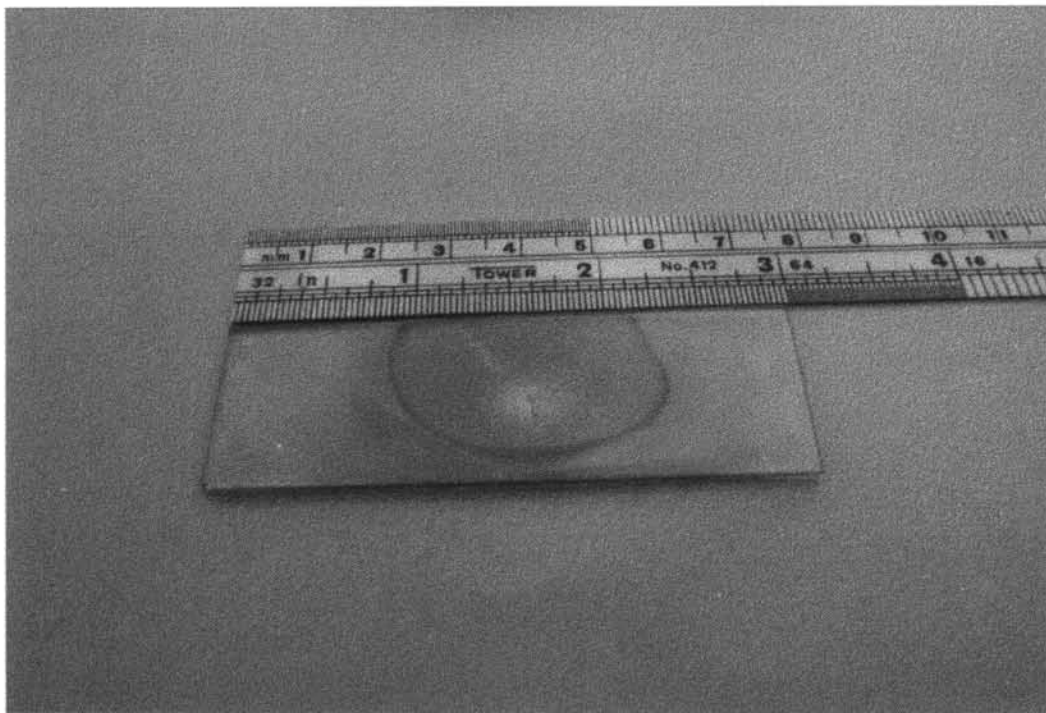


**Figure 5.5** Photograph of the deposited film on glass substrates at a distance 4 cm from the target surface with long side of the glass plate in the vertical direction. The plasma is elongated in the vertical direction.

reduced pressure and this has wide angular spread. One can consider that these are the reflected particles from the etch spot after back scattering from the Knudsen layer.

Fig. 5.5 shows the photograph of a film deposited on to a substrate which was kept parallel to the target surface at a distance 4 cm away from it with long side of the glass plate in the vertical direction. It is evident that the plasma gets elongated in the vertical direction taking an elliptical shape for the deposited film. The transparent central region in the film is metallic while the outer dark region is conducting. The metallic films are obtained at limited target-substrate distances viz. 3.5 to 4.5 cm from the target surface at a pressure of  $2 \times 10^{-5}$  mbar. The optical density along the film is given in Fig.5.6. The central region is having almost uniform transmission and there is a definite boundary between the two regions. Thus it can be seen that the central core of the plasma is more favorable for the deposition of good quality metallic films. The reasons for such a behavior is not very clear. But one can very well state from these observations that the

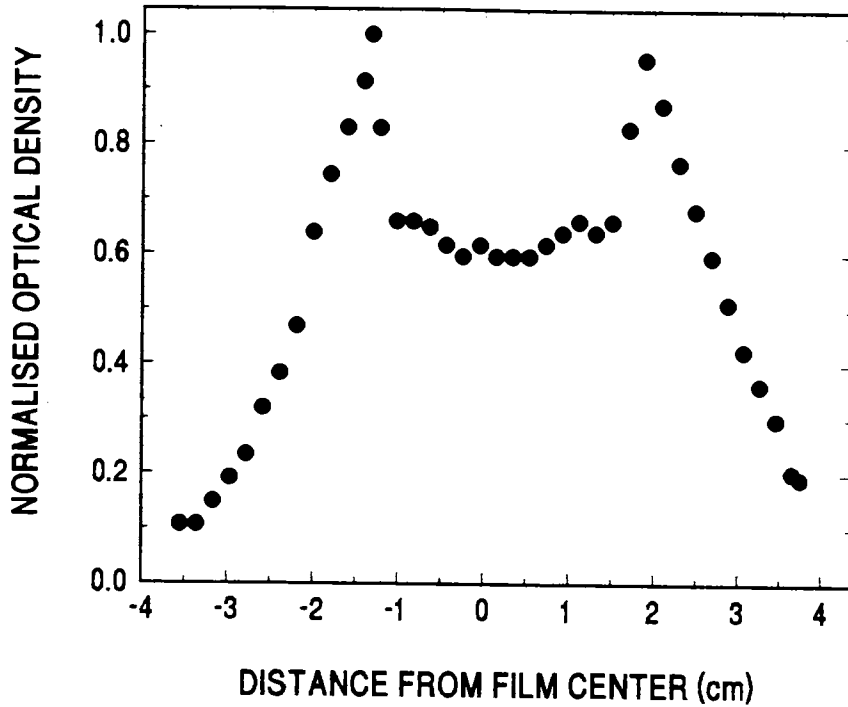


**Figure 5.6** Optical density of the deposited metallic film as a function of distance from the film center at a target-substrate distance of 4 cm. The central region is metallic and shows almost constant value for the optical density because of thickness uniformity.

deposition from the energetic particles favors metallic film growth since the central region of the plasma is more hot and energetic. But the exact reasons will remain obscure until an angle resolved temperature and density measurements are made. On the other hand the definite boundary between the metallic and non-metallic regions in the film implies a sort of discontinuity in the plasma parameters at the periphery of the plasma.

The elliptical isothickness behavior can be explained on the basis of the hydrodynamic model for laser plasmas based on the equations of fluid flow and the velocities are controlled by pressure gradients in the plasma. The mathematical form of the equation which controls the expansion of the plasma into vacuum is given by<sup>23,24</sup>

$$Z(t) \frac{d^2 Z}{dt^2} = \frac{k_B T_0}{M} \left( \frac{V_0}{V(t)} \right)^{\gamma-1}; \quad t > \tau_L \quad (5.1)$$

where  $Z(t)$  is the dimension of the expanding plasma  $T_0$  is the temperature at the focal spot just after the termination of the laser pulse,  $M$  is the particle mass,  $V_0 (= X_0 Y_0 Z_0)$  is the initial volume of the plasma,  $\gamma$  is the ratio of specific heats and  $\tau_L$  is the laser pulse width. The above equation suggests that the acceleration of the plasma species depends upon the temperature, initial dimensions of the plasma and the mass of the species. It is also seen from the above equation that the highest velocities of the species are in the smallest dimensions. This gives rise to the characteristic plasma shape elongated outward from the surface. Therefore if the initial plasma is longer in the  $y$  direction than in the  $x$  direction, it will be accelerated more rapidly in the  $x$  direction. Thus the plasma becomes elongated in the in the shorter dimensions during expansion and retains its profile during the deposition process. In the case of laser pulses incident on the target at  $45^\circ$  the horizontal plasma dimensions are higher than the vertical by a factor of  $\sqrt{2}$ . Then the plasma should be elongated in the vertical direction as it reaches the substrate.

## 5.2 Summary

In conclusion, angular distributions of ablated species are investigated in the laser produced silver plasma. There exists a boundary-like behavior in the thickness of the deposited film which shows the directive nature of the ablated species. This also suggests that deposition rate depends critically on plasma parameters and reveals the effective role of the hot species in metallic film growth inside plasma core. At reduced pressure the KL feeds an unsteady adiabatic expansion with more forward peaked angular distributions.

## References

- <sup>1</sup>D B Chrisey & G K Hubler (Eds.) *Pulsed laser deposition of thin films* (John Wiley & Sons, New York, 1994) and references therein
- <sup>2</sup>J C Miller and D B Geohegan (Eds.) *Laser Ablation: Mechanisms and Applications - II* (American Institute of Physics, New York 1994).
- <sup>3</sup>J C S Kools in Ref.1, p.455.
- <sup>4</sup>R E Russo, R P Reade, J M McMillan and B L Olsen, *J.Appl.Phys.* **68** (1990) 1354.

- <sup>5</sup>D B Geohegan, *Thin Solid Films* **220** (1992) 138.
- <sup>6</sup>J Gonzalo, CN Afonso, F Vega, D Martinez Garcia and J Perriere, *Appl.Surf.Sci.* **86** (1995) 40.
- <sup>7</sup>L Venkatesan, X D Wu, A Inam, Y Jeon, M Croft, E W Chase, C C Chang, J B Watchman, R W Odom, F R di Brozolo and C A Magee, *Appl.Phys.Lett.* **53** (1988) 1431.
- <sup>8</sup>K L Saegner, in Ref.1, p.199.
- <sup>9</sup>I Weaver and C L S Lewis, *J.Appl.Phys.* **79** (1996) 7216.
- <sup>10</sup>P E Dyer, *Appl. Phys. Lett.* **55** (1989) 1630.
- <sup>11</sup>K Scott, J M Huntley, WA Philips, John Clarke and JE Field, *Appl.Phys.Lett.* **57** (1990) 922.
- <sup>12</sup>P E Dyer, A Issa and P H Key *Appl. Surf. Sci.* **46** (1990) 89.
- <sup>13</sup>D B Geohegan and Poretzky, *Appl.Phys.Lett.* **67** (1995) 197.
- <sup>14</sup>R Kelly and R W Dreyfuss, *Surf. Sci.* **198** (1988) 263.
- <sup>15</sup>R Kelly and D Braren, *Appl. Phys. B* **160** (1991) 169.
- <sup>16</sup>I Noorbachta, R R Luichase and Y Zeire, *J. Chem. Phys.* **89** (1988) 5251.
- <sup>17</sup>J R Ho, C P Grigoropolous and J A C Humphry, *J.Appl. Phys.* **79** (1996) 7205.
- <sup>18</sup>R Kelly and R W Dreyfuss, *Nucl. Instr. Meth. Phys. Res.* **B32** (1988) 341.
- <sup>19</sup>J C S Kools *J.Appl.Phys.* **74** (1993) 6401.
- <sup>20</sup>R Kelly, *J. Chem. Phys.* **92** (1990) 5407.
- <sup>21</sup>Riju C Issac, K Vasudevan Pillai, S S Harilal, Geetha K Varier, C V Bindhu, Pramod Gopinath, P Radhakrishnan, V P N Nampoori and C P G Vallabhan, *Appl. Surf. Sci.* **125** (1998) 227.
- <sup>22</sup>C N Afonso, R Serna, F Catalina and D Bermejo, *Appl. Surf. Sci.* **46** (1990) 249.
- <sup>23</sup>R K Singh, D W Holland and J Narayan, *J. Appl. Phys.* **68** (1990) 233.
- <sup>24</sup>R K Singh and J Narayan, *Phys. Rev. B* **41** (1990) 8843.
- <sup>25</sup>F Antoni, C Fuchs and E Fogarassy, *Appl. Surf. Sci.* **96 - 98** (1996) 50.
- <sup>26</sup>W Pietsch, *J. Appl. Phys.* **79** (1996) 1250

# Ionization and collective drift in laser-plasma from $\text{YBa}_2\text{Cu}_3\text{O}_7$

## Abstract

In this chapter, laser absorption and ionization mechanisms in the solid  $\text{YBa}_2\text{Cu}_3\text{O}_7$  target are discussed. Also the diffusion of ions is investigated by time-of-flight profile analysis. It has been found that at high laser power densities, the plasma drifts collectively away from the target due to the formation of charged double layers and the collective behavior of diffusion is similar to the ambipolar diffusion.

As illustrated in the earlier chapters, the study of the transport properties in laser-produced plasmas can shed light into the different mechanisms involved in their formation and evolution in time and space. Also it may be noted that laser-plasmas generated in low ambient gas pressures have a wide range of applications as in material analysis<sup>1</sup> and thin-film deposition of materials like metals, ferroelectrics, semiconductors, and high-Tc superconductors.<sup>2-5</sup> Fabrication of stoichiometric films of high-Tc superconductors in air at atmospheric pressure have been reported recently.<sup>6,7</sup> Plasmas formed at atmospheric pressure have high temperature and density, and the concentrations of the various species may become close to the stoichiometric proportions in the target.

Among the various plasma parameters, the plasma temperature and plasma density (both of electrons and ions) are the major quantities that determine the plasma characteristics. A study of the dependence of these quantities with respect to the laser power density, the ambient pressure and time can be used to characterize various electronic and photonic processes taking place inside the plasma.<sup>8,9</sup> As far as the basic

interaction processes of the laser with various targets are concerned, it is of vital importance to study the absorption mechanisms in the target as well as in the plasma.

Laser-target interaction leads to rapid expansion and the velocities of ejected species generally depend on their mass which vary for atoms, molecules, or clusters. A slight deviation from charge neutrality at the external plume boundary may create large electric fields because of the formation of a charged double layer which results in the acceleration of individual charged particles.<sup>10-12</sup> Double layers are regions of non-neutral plasma and it consist of two adjacent non-neutral layers of opposite charge. A general description of the double layers is given by the pioneering works of Eliezer & Hora (see for example references 10 & 11) and a brief description is given in chapter 1 of this thesis. A double layer in principle can be associated with collisionless shocks, the presence of turbulence, phase space vortices (near the double layer), plasma ionization, ion acoustic fluctuations etc. In high intensity laser-plasma interactions, the double layers are time dependent, *i.e.* the associated charges and electric fields are changing on a time scale smaller than the TOF of particles through the double layer. Such charged double layers can be formed in laser-produced plasmas with electron densities<sup>10</sup> in the range  $10^6 - 10^{21} \text{ cm}^{-3}$ . In this chapter, various ionization mechanisms and the collective drift of ions and electrons in the plasma plume as a whole due to the electric fields created by charged double layers of electrons and ions which has been found experimentally are discussed.

The schematic arrangements of the experimental set up for the emission measurements was almost the same as the one described earlier in chapter 2 except for the fact that the measurements were done at atmospheric pressure. High-power laser radiation from the Q-switched Nd:YAG laser at wavelength  $1.06 \mu\text{m}$  with pulse duration 10 ns is focused on to the target (disc of  $\text{YBa}_2\text{Cu}_3\text{O}_7$ ) to produce the plasma in air at atmospheric pressure. The optical emission from the plasma at various spatial positions away from the target surface was monitored after one-to-one imaging of the plasma segments on to the entrance slit of a monochromator by appropriate collimating

or focusing lenses and by apertures. The spectrometer used was a 1 m SPEX monochromator. A thermoelectrically cooled photomultiplier tube was used for light detection at the exit slit of the monochromator.

The TOF profiles of optical emission at a particular distance from the target was monitored using a 200 MHz digital storage oscilloscope (DS 8621, IWATSU). The spectral recording was done on a chart recorder/personal computer after averaging intensities from 10 successive pulses using a boxcar averager. The laser pulse energy was measured using a calibrated laser energy meter and the power density at the focal spot was calculated only after making reflection corrections from lens surfaces.

### 6.1 Electron density measurements using laser interferometry

Electron density of the plasma is evaluated using a Michelson interferometer (MI) the details of which were already described in Chapter 2. Using the MI, the refractive index of the plasma is measured and from that the electron density is deduced. The ablated material ejected from the target surface consists of ions, atoms and molecules in addition to free electrons. All these species may be expected to contribute to the refractive index of the plasma. The atomic contribution to the refractive index ( $\mu_{at}$ ) is given by<sup>13</sup>

$$\mu_{at} = 1 + \frac{e^2}{8\pi^2 \epsilon_0 m} \sum_i \frac{N_i f_i}{(\nu_i^2 - \nu^2)} \quad (6.1)$$

where  $e$  is the electron charge,  $\epsilon_0$  the permittivity of free space,  $m$  the mass of electron,  $N_i$  the number density of the lower level of a transition,  $f_i$  the oscillator strength,  $\nu_i$  any resonance line frequency and  $\nu$  the frequency of light used to make the measurements. The above equation suggests that the contribution from the atomic/ionic refractivity is appreciable only near the resonance frequencies. All the resonance lines in the present plasma are sufficiently far from the probe wavelength (He-Ne laser, 632.8 nm). Hence only the electron contribution to the refractive index dominates in the present

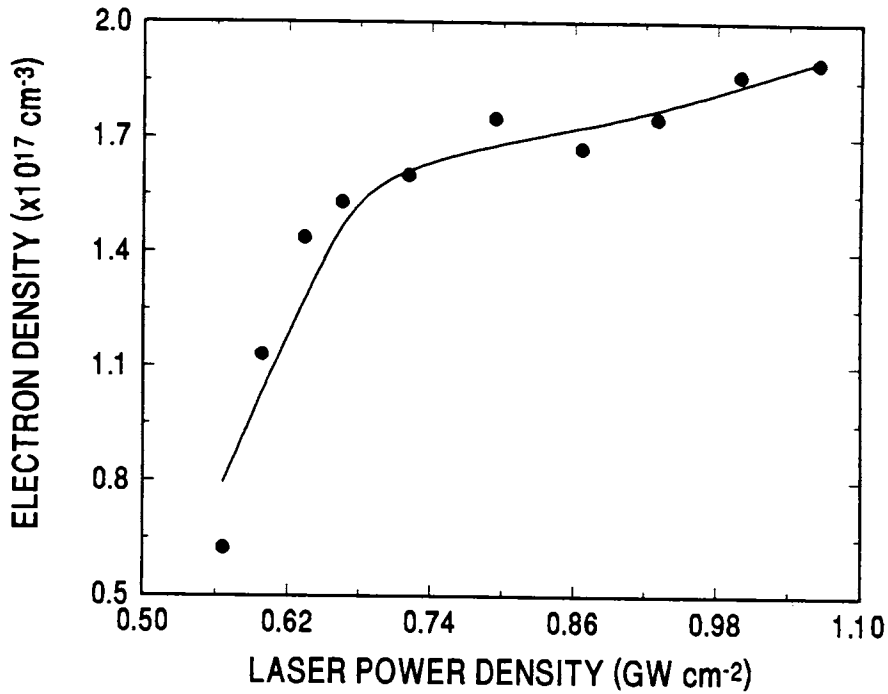


**Figure 6.1** Variation of electron density as a function of laser power density

measurements. The line averaged electron densities were calculated using the equation, (See Eqn. 2.6, Chapter 2)

$$n_e \cong \frac{k\gamma(t)}{\lambda l} \quad (6.2)$$

Here  $k \cong 1.778 \times 10^{12} \text{ cm}^{-1}$ ,  $\gamma(t)$  the phase difference due to the presence of the plasma,  $\lambda$  is the probe beam wavelength and  $l$  the lateral extension of the plasma.

Fig.6.1 represents the variation of the electron density with the laser power density. Even though the electron density is a function of time, the temporal variation of the electron density before or after the termination of the laser pulse is not considered here. Instead, the peak electron density is plotted as a function of laser power



density . The electron density ranges from  $4 \times 10^{16} \text{ cm}^{-3}$  to  $2.4 \times 10^{17} \text{ cm}^{-3}$  in the present power density used and it exhibits a nonlinear relationship with laser power density. The distinct regions of different slopes correspond to different mechanisms for the laser beam interaction with the plasma. Near  $0.55 \text{ GW cm}^{-2}$  rapid ionization causes surface damage of the sample. Above this threshold, there is a marked increase in the plasma electron density for power densities up to  $0.65 \text{ GW cm}^{-2}$ . Beyond this intensity the change in electron density seems to be more gradual up to about  $1 \text{ GW cm}^{-2}$ .

## 6.2 Laser-plasma interaction and ionization

In general, the leading part of the laser pulse produces the plasma while the trailing part interacts with the plasma resulting in intense ionization of its constituents. The two main ionization mechanisms in laser plasmas are the ionization by inelastic collisions of electrons with atoms and the direct multiphoton ionization of atoms due to bound-free transitions of atomic electrons. The ionization rate in the case of collisional ionization  $w_c$  is given by<sup>8</sup>

$$w_c \approx \frac{\nu_{in} \xi_{os}}{I_i} \quad (6.3)$$

where  $\nu_{in}$  is the frequency of inelastic collisions,  $I_i$  is the ionization energy and  $\xi_{os}$  is the electron oscillation energy given by

$$\xi_{os} = 0.093 \lambda^2 I \text{ (eV)} \quad (6.4)$$

Here  $\lambda$  is the wavelength of the laser light and  $I$  is the power density ( $\text{W cm}^{-2}$ ) at the focal spot. But in the case of direct photoionization, the ionization rate is given by

$$w_n \approx w_0 n^3 \left( \frac{\xi_{os}}{I_i} \right)^p \quad (6.5)$$

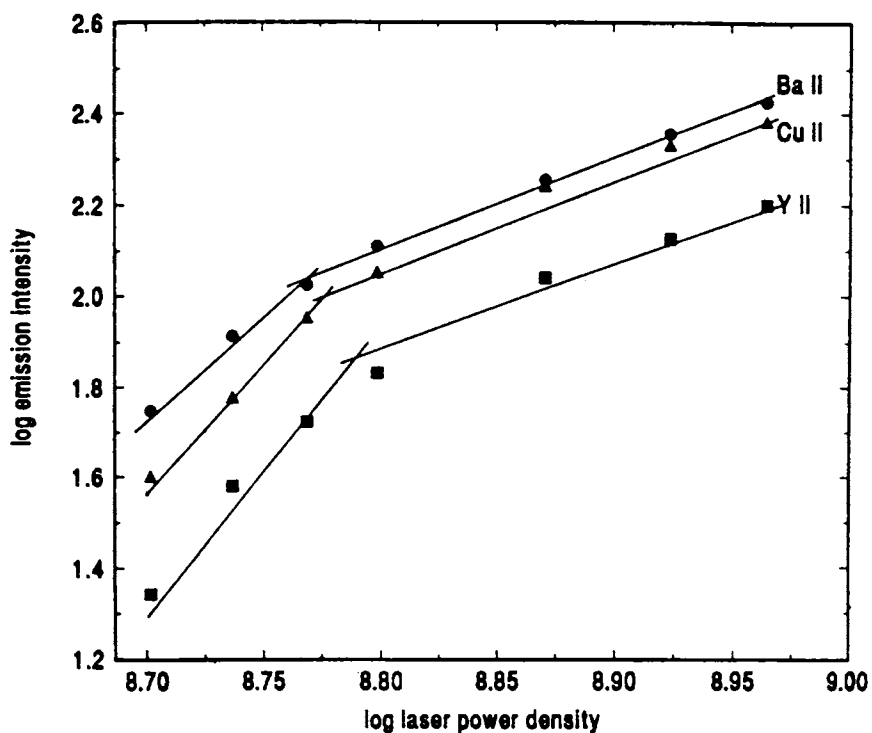


**Figure 6.2** Variation of the logarithm of the ion emission intensity of first ionized lines (■) YII (395.04 nm) (●) BaII (389.18 nm) (▲) CuII (417.18 nm) with log laser power density showing multiphoton ionization at low laser power densities and collision induced ionization at higher power densities.

where  $p = I_i / \hbar\omega$  is the number of absorbed quanta. It is clear from the above equations that the ionization rate is dependent on the laser power density through the electron oscillation energy. While the collisional ionization rate has a weak dependence on the laser power density, the ionization rate due to the multiphoton processes is strongly dependent on the power densities. In the present case  $\hbar\omega = 1.17 \text{ eV}$  for a  $1.06 \mu\text{m}$  radiation which is very much smaller than the ionization potentials of any of the constituent atoms inside the plasma. The first ionization energies for different constituents of the plasma are given in table 6.1. Since the ionization rate is proportional to the electron density in the plasma, the dependence of the emission intensity on the laser power density should be the same as that of the rate of ionization, except for a change in the proportionality constant.<sup>14</sup> The direct photoionization of any of these atoms require more than one photon of  $1.06 \mu\text{m}$  radiation.

Element	First ionization potential (eV)
Yttrium	6.38
Barium	5.21
Copper	7.73
Oxygen	13.62
Nitrogen	15.6

**Table 6.1** The first ionization potentials of various species in the plasma as given in R C Weast *C R C Handbook of Chemistry and Physics*, C R C Press 1988

Fig.6.2 shows the double logarithmic plot of the laser power density vs the emission intensity of single ionic lines from  $Y^+$  (395.04 nm),  $Ba^+$  (389.18nm) and  $Cu^+$  (417.18 nm). One can see that the intensity of these lines grow as  $I^p$  where  $p \sim 6$  for  $Y^+$ , 5 for  $Ba^+$  and 6 for  $Cu^+$  at lower power densities but approximately with  $p$  between 1 and 2 at higher power densities. For both  $Y^+$  and  $Ba^+$  the multiphoton energy slightly exceeds the ionization potential but for  $Cu^+$  it is slightly less than the ionization potential. This effect could be due to the depletion of the neutral atoms inside the plasma as suggested by several other workers.<sup>15,16</sup> But from Fig.6.3 for  $N^+$  (404.13nm) the emission line intensity grows very gradually with  $p$  in the range 1 to 1.5. In this case there is no further saturation of the line intensity at higher power densities indicating that from very low to very high power densities the ionization rate is the same. For oxygen (407.22nm), there exists a change in slope in the log-log plot. But the higher slope in lower range of laser power densities does not match with the ionization potential of oxygen. The simultaneous absorption of at least twelve photons is required for the direct multiphoton photoionization of oxygen, the cross section for which should be very low. There can be a small number of molecules getting multiphoton photoionized but the major contribution is from collisional processes. The results given in Figs.6.2 and 6.3 therefore show that at low laser power densities the elements present inside the target with comparatively low ionization potentials are multiphoton photoionized while ambient nitrogen gets ionized due to collisions throughout the power density range used

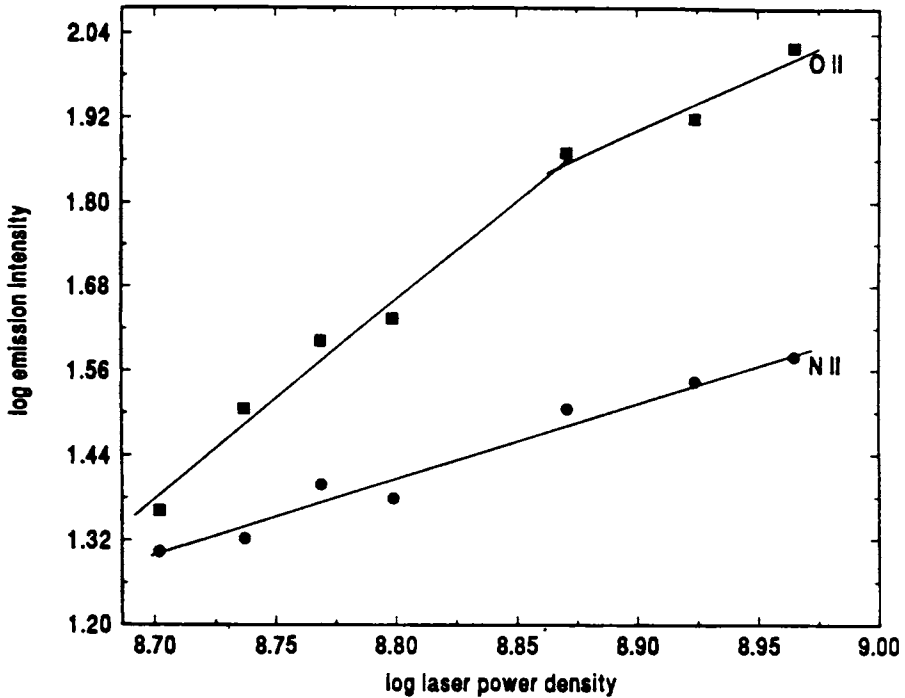


**Figure 6.3** Plot of logarithm of ion emission intensity for (■) OII (407.22 nm) and (●) NII (404.13 nm) indicating the effect of collisional ionization for oxygen and nitrogen during the power densities range.

here. Emission corresponding to oxygen is stronger than that due to nitrogen because of the additional source of oxygen from the target apart from that present in the atmosphere. At high laser power density the ionization is predominantly due to collisions, in the case of species with low ionization potentials (*Y*, *Ba* and *Cu*) also.

For low laser power densities, *i.e.* in the range from about 0.5 to 0.65 GW cm<sup>-2</sup>, the electron density also varies as  $n_e \propto I^p$  where  $p$  has values between 6 and 7 (Fig.6.1). This supports the fact that multiphoton absorption is a dominant ionization process in this range since  $6 \hbar\omega = 7.02 \text{ eV}$  is slightly greater than the ionization potentials of *Y* and *Ba*. But above 0.65 GW cm<sup>-2</sup>, the dependence of the electron density on the laser power density is rather weak and here  $p$  ranges from 1 to 2. In this case the exponent is close to unity and obviously the multiphoton ionization is not likely to be the dominant process. Instead of multiphoton ionization, collision induced ionization which is weakly dependent on the laser power density is dominating. This means that beyond a threshold value for electron number density, the number of

inelastic collisions between the electrons and the atoms get enhanced and the main ionization mechanism becomes the collision induced one. The fact that above  $0.65 \text{ GW cm}^{-2}$  the emission spectrum is rich in singly ionized species with some doubly ionized ones supports the above argument. The higher ionized states should be due to collisions and not due to photoionization because of the very high ionization potentials, whereas in the case of low laser power densities the dominance of neutral and singly ionized species and the absence of higher ionized states show that the collision dominated processes are negligible.

The reason for the saturation effect in the electron density at high laser power densities is the shielding of laser light by the plasma which will reduce the effective laser power density available for the laser-target and laser-plasma interactions. Above the threshold laser power density ( $0.65 \text{ GW cm}^{-2}$ ), the trailing part of the laser pulse does not penetrate sufficiently into the plasma so as to have multiphoton ionization. Before getting expanded, the plasma is confined to a region with characteristic dimension of the etch depth on the target (with typical values of a few microns, see for example references 17 & 18). During this period the trailing part of the laser pulse interacts with the plasma. Above a threshold value of the laser power density, the electron density present within the etch depth may exceed the critical density. Hence the laser light is screened off being absorbed by the plasma.

### **6.3 Radial drift in laser plasmas**

Laser-produced plasmas at atmospheric pressure are dense and confined to small volume due to the inward force exerted by the atmospheric gases. The apparent length of the light emitting zone in the plume was about 5 mm. Interferometric measurements on  $\text{YBa}_2\text{Cu}_3\text{O}_7$  plasma in air described in the previous section show that plasma electron density was of the order of  $10^{16}$ - $10^{17} \text{ cm}^{-3}$ . It was also found that at high laser power densities, the main ionization mechanism in the plasma is collision dominated whereas at relatively moderate laser power densities, multiphoton processes dominate. In

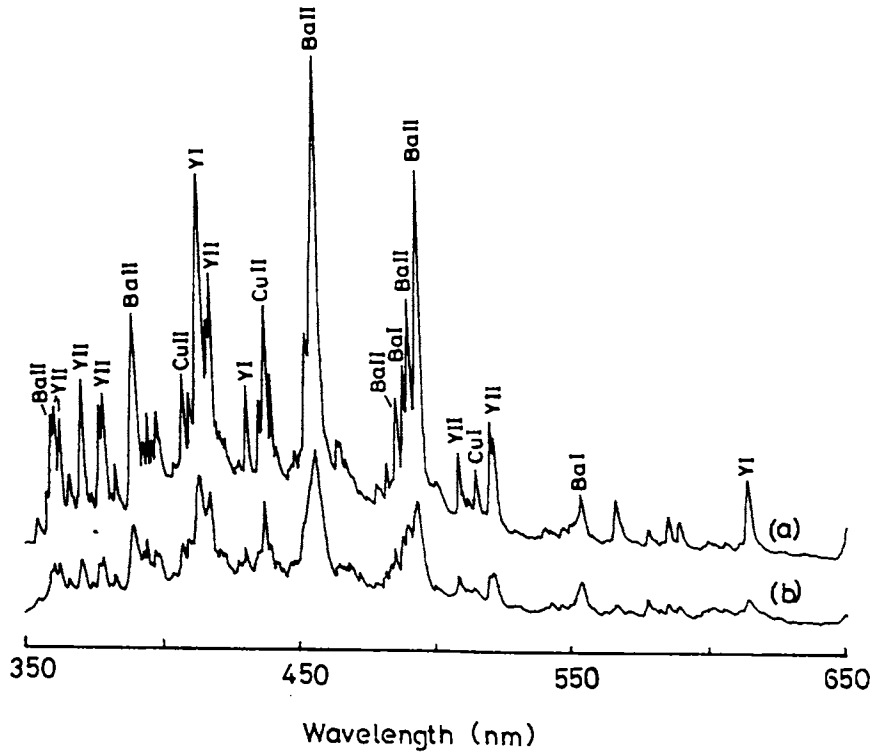


**Figure 6.4** The emission spectrum at two different laser irradiances at a distance 0.5 mm from the target; (a)  $1.9 \times 10^{11} \text{ W cm}^{-2}$  (b)  $3 \times 10^{11} \text{ W cm}^{-2}$ . The curves are identical except for a three fold decrease in intensity at higher laser irradiance. The intensities are peak values of the time dependent signal recorded after averaging intensities from ten pulses and maximum error in intensity measurements is 5 %.

this section, the diffusion characteristics is analyzed as a function of laser power density. The drift of the plasma away from the target surface is found to vary significantly with laser power density on the target. Plasma emission very close to the target is monitored and the optical emission spectrum at a laser power density of  $1.9 \times 10^{11} \text{ W cm}^{-2}$  is recorded in the region 350 nm to 650 nm [Fig. 6.4(a)]. The spectrum shows mostly ionic emission lines from different constituents within the plasma together with a few atomic lines. Less intense lines from singly and doubly ionized nitrogen present in air also are observed in spectra measured with higher resolution. Fig.6.4(b) represents the spectrum at  $3 \times 10^{11}$

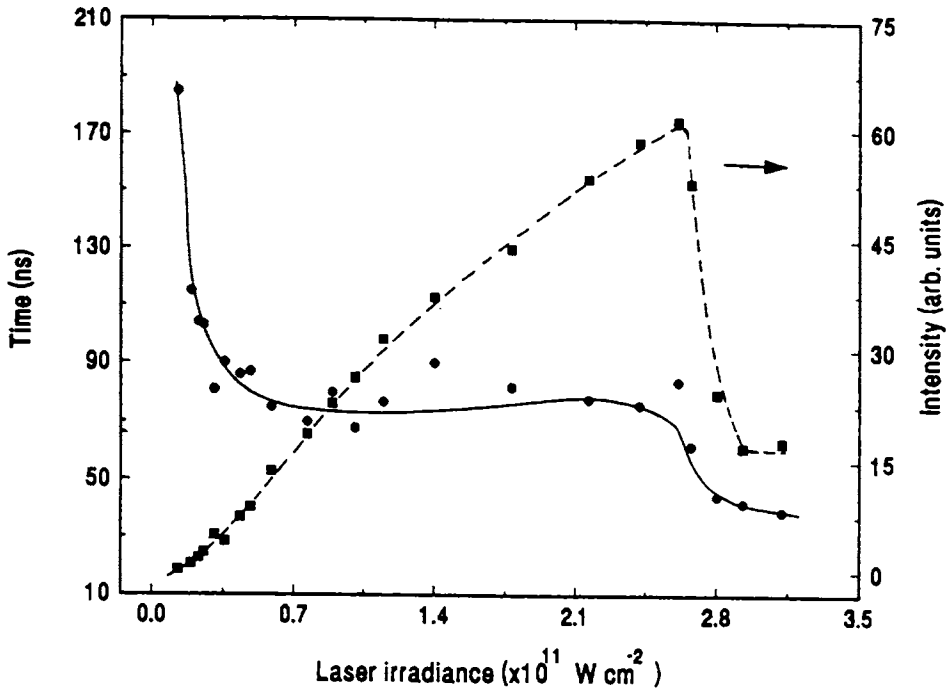


**Figure 6.5** Variation of plasma expansion time (●) as well as continuum intensity (■) as a function of laser power density. At a laser irradiance of  $\approx 2.6 \times 10^{11} \text{ W cm}^{-2}$ , the expansion time decreases to about half the initial value. Exactly at this point the continuum emission intensity also decreases sharply. Measurement conditions are same as those for Figure 6.4

$\text{W cm}^{-2}$  which shows a three fold decrease in emission intensity for all the lines. This apparently anomalous behavior at higher laser power density is explained in a later section. In order to estimate the plasma expansion time, the monochromator was set at 500 nm where there is only continuum emission with no line emissions from any of the species and the expansion time and emission intensity were measured from the oscilloscope display. The main reason for selecting plasma continuum for this study is that the positive ions and electrons are responsible for the blackbody continuum since plasma continuum essentially originates from the bremsstrahlung radiation and radiative recombination.<sup>19</sup>

Measurements on the plasma expansion time at various laser power densities were carried out. Fig.6.5 shows a plot of the laser power density vs the plasma

expansion time at a distance 0.5 mm from the target surface. At very low laser power densities, there is a sudden decrease in the plasma expansion time as the laser power density is slowly increased. On further increasing the laser power density, the expansion time remains at a steady value of about 83 ns. This initial sharp increase in the velocity at low power densities is due to the plasma expansion resulting from the very high internal pressure developed at the ablation spot where the ejected material acts as a piston which drives a spherical blast wave into the ambient gas. But this pressure reaches a steady state value and consequently the expansion velocity assumes a constant magnitude of  $6.02 \times 10^5 \text{ cm s}^{-1}$ . This happens when the laser light is screened in the sense of not being absorbed by the target due to reflection by the high density plasma at the critical density surface. But when the laser power density is increased further, to  $\approx 2.6 \times 10^{11} \text{ W cm}^{-2}$ , the expansion time suddenly decreases to approximately half the initial value, namely, 40 ns with a four fold increase in the kinetic energy. This means that the expansion velocity of the plasma has suddenly doubled at this laser power density to a typical value of  $1.25 \times 10^6 \text{ cm s}^{-1}$ . It is also apparent from Fig.6.5 that the intensity of plasma continuum emission near the target falls steeply at this laser power density. Ionic and atomic line emissions also suffer reduction in intensity as can be seen from Fig.6.4(b) which is the optical emission spectrum from the plasma at a laser power density of  $3 \times 10^{11} \text{ W cm}^{-2}$ . The spectrum is almost similar to that obtained at  $1.9 \times 10^{11} \text{ W cm}^{-2}$  [Fig.6.4(a)] but with reduction in emission intensity for all the lines. This is due to a reduction in particle density integrated along the line of sight near the target surface, *i.e.* the plasma as a whole drifts away from the target thereby producing a rarefaction near the target. Thus at higher laser power densities two distinct types of plasma motion occur, the radial expansion as well as the sudden drift of the plasma as a whole normal to the target. The radial expansion becomes dominant only after the plasma has drifted to a certain distance away from the target surface which in turn depends on the value of laser power density.



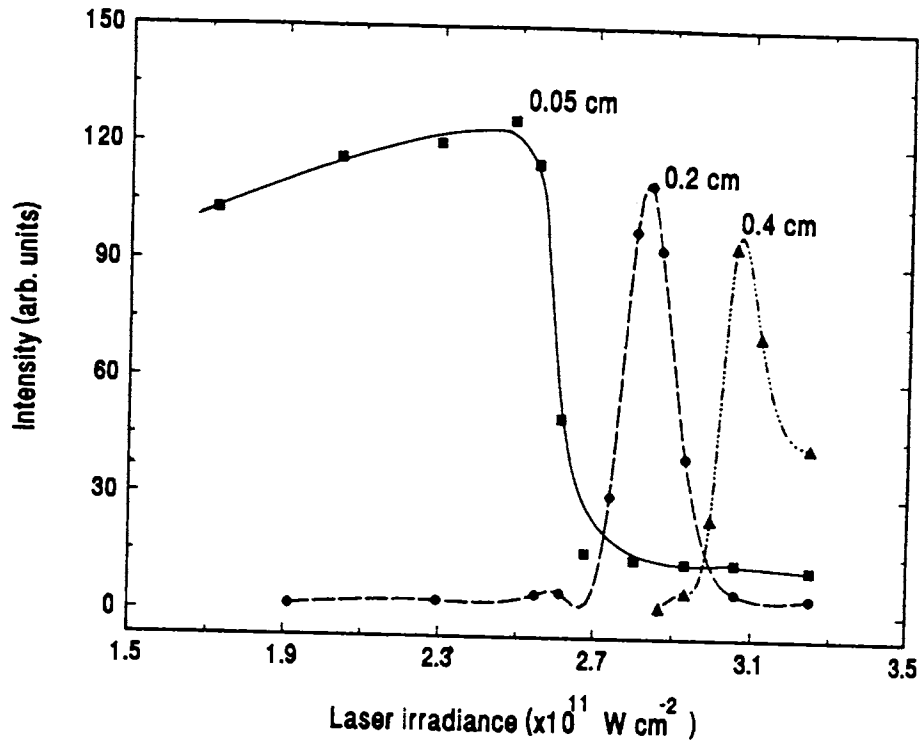


**Figure 6.6** Variation of continuum emission intensity at 500 nm at three different distances from the target. Measurement conditions are same as those for Figure 6.4

As mentioned in the previous paragraph, Fig.6.4(a) shows the spectrum at a laser power density of  $1.9 \times 10^{11} \text{ W cm}^{-2}$  which exhibits emission lines from all atomic and ionic species when only hydrodynamic radial expansion is predominant. However in Fig.6.4(b) the intensities of all these lines have gone down by a factor of nearly three even though the spectrum is recorded at a higher laser intensity ( $3 \times 10^{11} \text{ W cm}^{-2}$ ). This means that the number densities of almost all the species with different ionization states integrated along the line of sight are low near the surface for laser power densities above  $2.6 \times 10^{11} \text{ W cm}^{-2}$ , indicating the collective nature of the expansion process. This holds good for a range of laser power densities above the threshold of  $2.6 \times 10^{11} \text{ W cm}^{-2}$ . At these power densities, when observed normal to the plasma expansion direction (expansion direction is always normal to the target surface), the section with maximum intensity of plasma emission is at a region farther away from the

target surface. The spectra recorded at the maximum intensity region is the same as the one close to the target at low laser power density but with slightly reduced line widths.

The continuum emission intensity is maximum near the target surface and decreases with increasing separation from the target at low values of laser intensities. Fig. 6.6 shows a plot of emission intensity vs the laser power density at three different distances from the target surface, namely, 0.05 cm, 0.2 cm and 0.4 cm. At laser power densities greater than  $2.6 \times 10^{11} \text{ W cm}^{-2}$  the plasma continues to move with the same velocity but the plume as a whole is shifted to greater distances. These results show that at a distance 0.2 cm away from the target the emission peaks when the laser power density attains a value of  $2.84 \times 10^{11} \text{ W cm}^{-2}$  while at 0.4 cm the emission maximizes at a laser power density of  $3.05 \times 10^{11} \text{ W cm}^{-2}$ . It is evident from these observations that the plasma plume has drifted to regions farther and farther away from the target as the input laser power density is increased. The above mentioned behavior can be understood by considering the mechanisms described below.

#### 6.4 Discussion on electron heating and formation of charged double layer

The irradiation of a target with very high intensity lasers produce temperatures well above the thermodynamic critical temperature and the main mechanism of ablation is *phase explosion* rather than *vaporization*.<sup>20,21</sup> Radial expansion takes place because of the very high pressure developed following ablation of the target material leading to velocities of the order of  $10^5 \text{ cm s}^{-1}$  for the plume expansion front. There exists a steep density gradient along the radial direction in a laser-produced plasma. The density of electrons has a larger value towards the target surface and at some point nearer to the target the density exceeds the critical density which is defined as

$$n_{ec} = \frac{\omega^2 m_e \epsilon_0}{e^2} \quad (6.6)$$

where  $\omega=2\pi\nu$ ,  $\nu$  is the frequency of laser light,  $m_e$  is the mass of electron,  $e$  is the electron charge and  $\epsilon_0$ , the permittivity of free space. The laser beam penetrates into the plasma only if the electron density is less than the critical density. Basically the laser-ablated plume consists of two regions, the outer corona ( $n_e \leq n_{ec}$ ) and the conduction region ( $n_e \geq n_{ec}$ ). A surface which separates the two is called the critical density surface. A sharp boundary between the conduction region and the outer corona should not be expected and hence the critical density surface may not be thought of as infinitely thin. In the outer corona of the plume where the electron density is less than the critical density, the laser energy is absorbed by the electrons directly. The attenuation of the laser light as it traverses the plume is given by<sup>10</sup>

$$I_a = I_0 \left[ 1 - \exp\left(-\frac{32\nu_c}{15\omega} k_{IB} L\right) \right] \quad (6.7)$$

where  $I_0$  and  $I_a$  are the incident and the absorbed laser intensities for electron density  $n_e$  less than the critical density  $n_{ec}$ ,  $k_{IB}$  is the inverse-bremsstrahlung absorption coefficient,  $\nu_c$  is the collision frequency which goes down with temperature as  $\nu_c \propto T_e^{-3/2}$ . The scale length  $L$  is the distance over which the electron density changes from zero to  $n_{ec}$ . The energy absorbed by the corona electrons is transferred to the conduction region. If the heating rate of the corona electrons is much larger than the losses to the conduction region, the temperature of the corona electrons will rise and a temperature gradient may be formed. Therefore we can write<sup>22</sup>

$$\frac{dT_e}{dx} \geq \frac{T_e}{\lambda_{ee}} \quad (6.8)$$

where  $\lambda_{ee}$  is the mean free path for  $e-e$  collisions. The temperature gradient may be accompanied by an electric field given by

$$E \approx \frac{k}{e} \frac{dT_e}{dx} \quad (6.9)$$

and some of the electrons may be accelerated out of the corona. The loss of hot electrons creates a large potential which limits the total number of electrons that can be thrown off.<sup>23</sup> The electron heating will cease when the laser pulse is terminated. Thus ions inside the plume can be accelerated in the electric field generated by the fast electrons escaping from the plume.

Normally the diffusion coefficients of electrons ( $D_e$ ) and ions ( $D_i$ ) are different with their ratio given by,<sup>24</sup>  $(D_e/D_i) \propto (v_e/v_i) \propto (M/m)^{1/2}$  and it is clear that the relative values obey  $D_e \gg D_i$ . The fast escaping electrons produce a region in which there is a separation between the ion and electron clouds. These positive and negative charge clouds are in most cases separated by a characteristic distance which is of the order of the Debye length.<sup>10</sup> But in such cases of a deviation from charge neutrality the ions are accelerated in the electric field produced by the fast electrons receding from the plume and the plume as a whole begins to propagate with twice the diffusion coefficient of the ions similar to that in a discharge plasma.

Since the ions have a velocity less than that of the electrons, the fast electrons will create a situation in which the positive and negative charges are well separated. The electric field thus generated may be represented in terms of the electron velocity and density given by<sup>12</sup>

$$E = -\frac{m_e v_e^2}{e} \frac{\partial(\ln N_e)}{\partial z} \quad (6.10)$$

where  $m_e$  and  $v_e$  are the electron mass and velocity respectively,  $e$  the electron charge, and  $N_e$  the electron density in the plume. In the present experiment, the propagation direction of the plasma coincides with the  $z$ -axis which is normal to the target. One can make a rough estimate of the electric field by considering the additional velocity of the ions  $v_i$ , to be solely due to the electric field created by the separated electrons and ions after introducing a characteristic ion velocity<sup>12</sup>  $v_i^2 = (2Z_e m_e v_e^2) / M_i$  ( $v_i = 1.2 \times 10^6$  cm s<sup>-1</sup> in the present case), where  $M_i$  is the average

mass of the ions and  $Z_i$  their average charge. Then, with  $Z_i = 1$ , average mass number 45,  $\Delta z \approx 0.05 \mu\text{m}$ , (the typical length over which the field is applicable, *i.e.*, the Debye length for an electron density  $10^{17} \text{ cm}^{-3}$  and electron temperature 5 eV),  $\Delta N_e/N_e = 0.01$ , and  $E \approx 1.4 \times 10^5 \text{ V cm}^{-1}$ . That is, a 1% change in the electron density over a distance of the order of the Debye length produces electric fields of the order of  $10^5 \text{ V cm}^{-1}$ .

The collective nature of the expansion process shows that it is similar to ambipolar diffusion in a discharge plasma. The differential equation which governs the diffusion process becomes<sup>24</sup>

$$\frac{\partial N_i}{\partial t} = 2D_i \Delta N_i \quad (6.11)$$

Here  $N_i$  is the ion number density and  $\Delta N_i$  refers to the change in ion number density over a distance equal to the Debye length. This is the equation governing the diffusion of ions with  $D_i$  replaced by  $2D_i$  resulting from the coupling of diffusion processes of electrons and ions and mutual interaction of the electron and ion clouds. The electrons and ions diffuse together with twice the diffusion coefficient of the ions when there is a deviation from the total charge neutrality. Since the diffusion coefficient is directly proportional to the velocity, the observed increase in the velocity to approximately double the initial velocity supports the argument in favor of ambipolar diffusion. The collective nature of the diffusion process shows that the drift mechanism is similar to ambipolar diffusion.

## 6.5 Summary

Various aspects of laser produced plasma from a multicomponent target  $\text{YBa}_2\text{Cu}_3\text{O}_7$  in air at atmospheric pressure with laser power densities ranging from approximately  $0.5 \text{ GW cm}^{-2}$  to  $1.5 \text{ GW cm}^{-2}$  were investigated using emission spectroscopy and Michelson interferometry. From the results of intensity measurements of various emission lines as a function of laser power density it can be concluded that at low laser power densities the

main ionization mechanism for elements like *Y*, *Ba* and *Cu* which constitute the target is multiphoton induced while the dominant mechanism of ionization mechanism is that due to collisions at higher laser power densities. For *Cu* though it is present in the target itself, the number of quanta absorbed at low laser power densities is slightly less than that required for multiphoton photoionization. As a result of the high ionization potential, the major ionization mechanism in the case of oxygen atoms happens to be collision induced even though it is present in the target as a major constituent. The emission intensities from species like  $N^+$  present outside the bulk target show a linear dependence with the laser power density indicating the existence of collisional ionization processes. Line averaged electron densities were deduced from the interferometric measurements and found to vary from  $10^{16} \text{ cm}^{-3}$  to  $2.4 \times 10^{17} \text{ cm}^{-3}$  as the laser power density is increased from 0.5 to 1.1  $\text{GW cm}^{-2}$ .

Some relevant aspects on the diffusion process of laser-produced plasma from the multielement  $\text{YBa}_2\text{Cu}_3\text{O}_7$  target are also described using time-resolved spectroscopy at laser power density levels ranging from  $2.5 \times 10^9 \text{ W cm}^{-2}$  to  $3.5 \times 10^{11} \text{ W cm}^{-2}$ . It has been observed that at low laser power densities only radial expansion occurs while beyond a threshold of  $2.6 \times 10^{11} \text{ W cm}^{-2}$ , the plasma as a whole drifts collectively away from the target surface in the electric field produced by the formation of a charged double layer at the outer plume boundary. A rough estimate shows that an electric field of the order of  $10^5 \text{ V cm}^{-1}$  is generated at the plume expansion front. The collective nature of the diffusion is similar to ambipolar diffusion in a discharge plasma and it ensures that the stoichiometry of the various atoms and ions in the plume near the target surface is preserved at a farther distance from the target. As the input laser power density is increased, the plume propagates to farther distances in air within nanosecond time scale. In short, the various ionization mechanisms and the conditions pertaining to the formation of charged double layers in laser-plasmas at atmospheric pressure has been described in this chapter.

## References

- <sup>1</sup>Ganzalea A, Ortiz M and Campose J *Appl. Spectroscopy* **49** (1995) 1632.
- <sup>2</sup>Chrisey D B and Hubler G K (Ed.) *Pulsed laser deposition of thin films* (John Wiley & Sons New York, 1994)
- <sup>3</sup>Singh R K and Narayan J *Phys. Rev. B* **41** (1990) 8843.
- <sup>4</sup>Misra D S and Palmer S B *J. Appl. Phys.* **68** (1990) 1403.
- <sup>5</sup>Venkatesan T, Wu X D, Dutta B, Inam A, Hegde M S, Hwang D M, Chang C, Nazar L and Wilkens B *Appl. Phys. Lett.* **54** (1989) 581.
- <sup>6</sup>Wild J, Engst P, Civis S and Pochyly J *Appl. Phys. Lett.* **60** (1992) 1747.
- <sup>7</sup>Wild J, Bohacek P, Macl J, Engst P, Pracharova J and Pochyly J *Physica C* **209** (1993) 486.
- <sup>8</sup>Gamaly E G *Laser and Particle Beams* **12** (1994) 185.
- <sup>9</sup>Stwalley W C and Bahns J T *Laser and Particle Beams* **11** (1993) 185.
- <sup>10</sup>Eliezer S and Hora H *Phys. Rep.* **172** (1989) 339.
- <sup>11</sup>Eliezer S, Hora H, Kolka E, Green F and Szichman H *Laser and Particle Beams* **13** (1995) 441.
- <sup>12</sup>Gamaly E G *Phys. Fluids B* **5** (1993) 944.
- <sup>13</sup>Thorne A P *Spectrophysics*, (Chapman & Hall 1974) p.386.
- <sup>14</sup>Russo R E *Appl. Spectroscopy* **49** (1995) 14A
- <sup>15</sup>Chin S L, Isenor N R and Young M *Phys. Rev.* **188** (1969) 7.
- <sup>16</sup>Park C O, Lee H W, Lee T D and Kim J K *Appl. Phys. Lett.* **52** (1988) 368.
- <sup>17</sup>Neifeld R A, Potenziana E, Sinclair W R, Hill III W T, Turner B and Rinkas A *J. Appl. Phys.* **69** (1991) 1107.
- <sup>18</sup>Burns F C and Cain S R *J. Phys D: Appl. Phys.* **29** (1996) 1349.
- <sup>19</sup>Griem H R *Plasma Spectroscopy* (Mc Graw Hill Inc. New York, 1964)
- <sup>20</sup>Kelly R and Miotello M *Appl. Surf. Sci.* **96-98** (1996) 205.
- <sup>21</sup>Kelly R and Miotello M *Nucl. Instr. Meth. Phys. Res. B* **122** (1997) 374.
- <sup>22</sup>Hughes T P *Plasmas and Laser Light* (Adam Hilger, Bristol 1975) p.329
- <sup>23</sup>Brooks R D, Benzer R G and Pietrzyk Z A in *Laser interaction and related plasma phenomena* Vol.6, H Hora and G H Miley (Eds.) (Plenum, New York 1984) p.479
- <sup>24</sup>Lifshitz E M and Pitaevskii L P *Physical Kinetics* (Pergamon 1981) p.108

# Time-resolved study of spectral emissions and anomalous line profiles in laser generated plasma from $\text{YBa}_2\text{Cu}_3\text{O}_7$

## Abstract

Laser produced plasma from the multielement solid target  $\text{YBa}_2\text{Cu}_3\text{O}_7$  is analyzed at atmospheric pressure. A time resolved analysis of the spectral emission from the plume at various laser power densities has been carried out. It is also observed that at laser power densities equal to or exceeding  $1.6 \times 10^{11} \text{ W cm}^{-2}$ , a central peak begins to develop at the center of the self-reversed profile and this has been interpreted as due to the anisotropic resonance scattering (fluorescence) of radiation.

Experiments on laser ablation are generally done under low pressure ambient gas. But plasmas formed at atmospheric pressure may be considered to be in local thermodynamic equilibrium due to its high density and collision rate.<sup>1,2</sup> In this case also emission spectroscopy can effectively and accurately be used for the plume diagnostics. Also laser plasmas can be used as spectral sources for evaluating parameters like oscillator strengths and transition probabilities of atoms and ions.<sup>2</sup> These transient fireballs are very useful in studying the basic plasma processes such as the ionization mechanisms, effect of collisions, gas phase reactions etc.<sup>4-7</sup>

Laser plasmas are very rich sources for atomic and ionic emission lines and also continuum radiation. Line shape analysis can be used in the measurements of plasma parameters in several ways. Close interactions between an excited atom and an identical ground state atom can cause substantial broadening of the emission lines since the atoms and ions in the ground state absorb the emitted radiation resonantly.<sup>1</sup> Several studies on such resonance scattering of radiation in various types of plasmas have



proven to be effective in the determination of the number densities of various emitting species and other parameters like the optical depth and plasma absorption.<sup>8-11</sup> Knowledge of self-absorption and the optical thickness are essential for the spectroscopic diagnostics of the plume.<sup>12</sup> Since the absorption is stronger at the line center than at the wings, the emission at the central wavelength can get severely absorbed with the interesting result that, in the presence of temperature gradients, the self-reversal of the spectral line will occur.<sup>1</sup> Owing to very high densities of atomic and ionic species in laser produced plasmas, self-absorption is severe, particularly at high enough ambient pressure. There exist a few reports related to self-reversal of spectral lines from laser produced plasmas.<sup>12-15</sup> The detailed line profile depends critically on the particle density as well as its transport properties in the plasma. The widths of the resonant lines are as high as a few tens of angstroms and are directly proportional to the density of the emitting species and the absorption oscillator strength.<sup>10</sup> Therefore, the line width is a direct measure of the emitter number density inside the plasma.

In this chapter the time-resolved emission characteristics of laser produced plasma from  $\text{YBa}_2\text{Cu}_3\text{O}_7$  and aluminum in the spectral range 350-650 nm are presented. It has been observed that emission line profiles of resonance lines are broadened predominantly by self-absorption and the dominant broadening in non-resonance lines are due to Stark effect. Emission line profile of the resonant transition from Ba II at 455.403 nm, its evolution in time and its dependence on the laser power density are analyzed. Another target which is used for spectral measurements is aluminum, being simple in composition. The plasma continuum emission, electron density and opacity from  $\text{YBa}_2\text{Cu}_3\text{O}_7$  and aluminum plasma plumes are subjected to detailed investigations in the following sections.

## 7.1 Time resolved emission from $\text{YBa}_2\text{Cu}_3\text{O}_7$ plasma at atmospheric pressure

The pulsed laser evaporation process can in general be classified into three separate regimes<sup>16</sup>: the interaction of the laser beam with the target material resulting in the evaporation of the surface layers, interaction of the evaporated material with the incident laser beam causing rapid ionization and plasma formation and finally the rapid cooling of the plasma. The plasma evolution after the interaction of the high power laser beam with the target consists of two distinct domains in time. Initially there is a sudden increase in the emission intensity and after attaining a peak value, the intensity decreases rapidly. We have carried out time resolved spectral measurements in these two time domains with a view to decipher the different heating, ionization, and cooling processes taking place inside the plasma. The time resolved emission spectra are given in Figures 7.1 and 7.2, respectively, which clearly distinguish the different emission processes occurring inside the plasma. At the initial stages of the plasma formation which extend from 0 to about 55 ns, there is an increase in the overall emission intensity. It should be noted that 55 ns time is significantly longer than the pulse duration. In this time span (0 to 55 ns), as seen from Figure 7.2, the emission spectrum consists of the plasma black body radiation, without much of line emissions. In general, the main source of the plasma continuum is the bremsstrahlung radiation and radiative recombination.<sup>1</sup>

Bremsstrahlung process is basically a free-free (ff) transition where the binding energy of free electron is considered as negative.<sup>1</sup> The emission coefficient for bremsstrahlung process is given by,<sup>2</sup>

$$\varepsilon_{ff}(\omega) = 8.67 \times 10^{-53} N_e N_i Z^2 T^{-1/2} e^{-h\omega/kT} G_{ff} \quad (7.1)$$

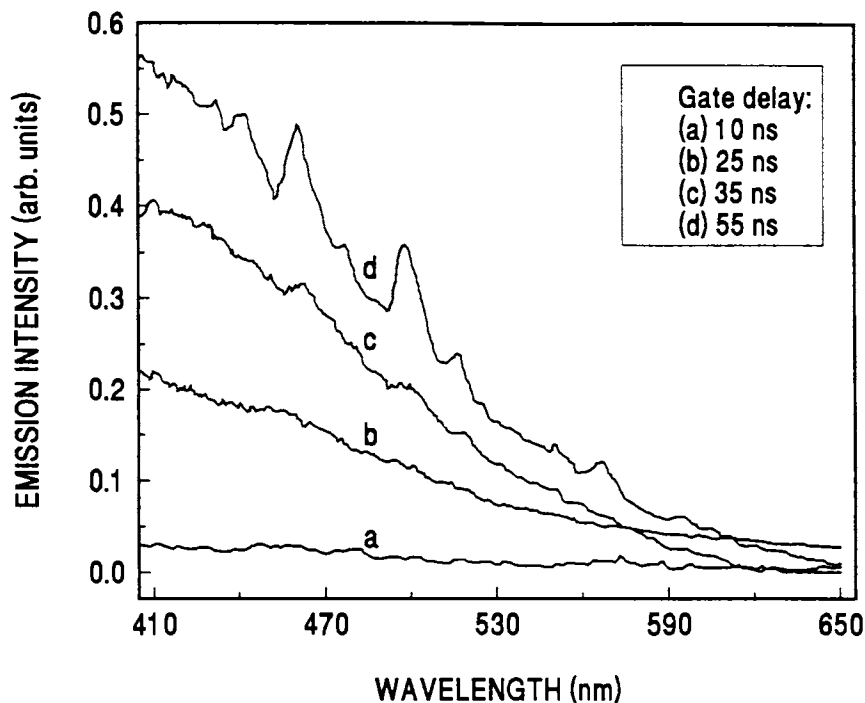


**Figure 7.1** Time resolved plasma emission spectrum in the wavelength range 400-650 nm at different time delays and at typical laser power density  $0.8 \text{ GW cm}^{-2}$ ; (a) 10 ns, (b) 25 ns (c) 35 ns and (d) 55 ns.

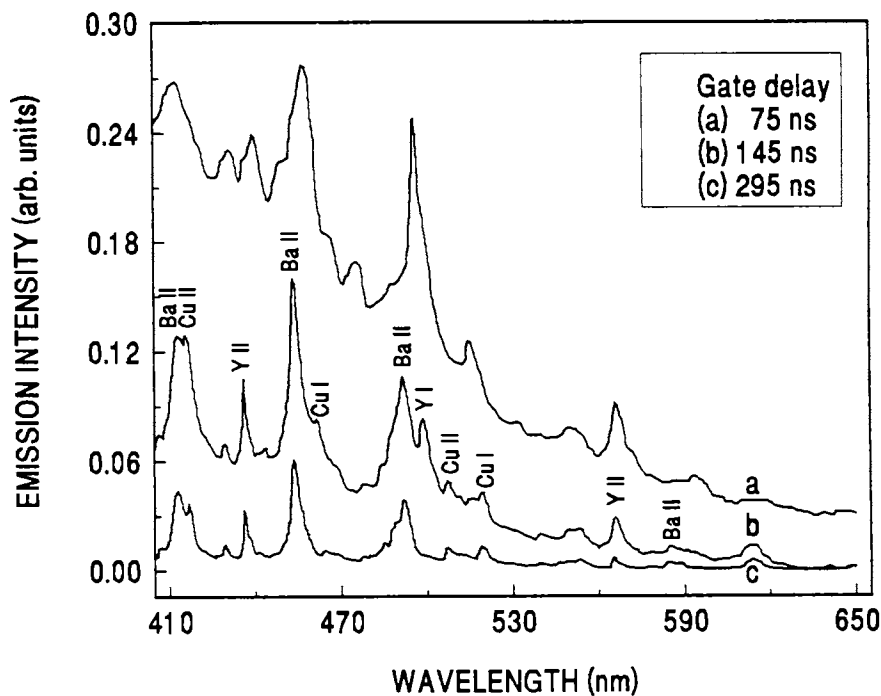


**Figure 7.2** Plasma emission spectrum in the wavelength range 400-650 nm at different time delays at a laser power density  $0.8 \text{ GW cm}^{-2}$ ; (a) 75 ns, (b) 145 ns and (c) 295 ns.

where  $\varepsilon_{ff}(\omega)$  is the energy emitted per unit time, volume, solid angle and angular frequency interval.  $Z$  is the atomic number,  $T$  is the temperature and  $G_{ff}$  is the so called Gaunt factor; a dimensionless quantity ranging in value from about 1 to 10 which allows for appropriate cut-offs in the impact parameter and for quantum mechanical corrections of the classical electron trajectory.

Radiative recombination process is basically a free-bound (fb) transition in which the electrons combine with an ion in a certain bound state and the excess energy is radiated as a photon. The emissivity (power emitted in watts per cubic meter of plasma per unit solid angle, per radiation frequency interval  $d\omega$ ) from recombination into the  $n^{\text{th}}$  shell of a hydrogenic ion of charge  $z$  is<sup>2</sup>

$$\varepsilon_{fb} = 7.4 \times 10^{-50} N_e N_{z+1} T^{-3/2} E_i^2(z, n) \left( \frac{\zeta_n}{n} \right) e^{(E_i - \hbar\omega)/kT} G_{fb} \quad (7.2)$$

where  $N_{z+1}$  is the density of ions of charge  $z+1$  in  $\text{m}^{-3}$ ,  $E_i$  is the ionization potential from the final state in eV,  $\zeta_n$  is the number of places in the  $n^{\text{th}}$  shell that can be occupied by the captured electron and  $G_{fb}$  is the Gaunt factor for free-bound transitions. Therefore the radiative recombination rate is proportional to the electron number density and the density of ions.

The total continuum emission intensity is the sum of the contributions from both bremsstrahlung and radiative recombination. But for temperatures very much higher than the ionization potentials of radiating atoms, bremsstrahlung predominated over radiative recombination. During the initial stages of plasma formation, the temperatures must be well above the ionization potentials so that, the bremsstrahlung process dominates at small time delays. The recombination and the subsequent de-excitation start only after a delay from the laser pulse. Therefore, it can be inferred that in the present case, bremsstrahlung process contributes predominantly to the continuum emission.

Beyond 55 ns, as shown in Figure 7.2 the line to continuum intensity ratio increases and finally, after about 150 ns, the spectrum consists mainly of emission lines corresponding to atomic and ionic species. It has also been observed that the emission lines are highly Stark broadened during the initial stages of the plasma owing to very high plasma electron densities. The emission spectra obtained at different laser power densities are recorded and it is seen that at relatively low power densities the spectrum represents mostly neutral and singly ionized species while at higher laser power densities it contains lines corresponding to neutral, singly and doubly ionized species. Lines corresponding to Ba(I), Ba(II), Y(I), Y(II), Cu(I), Cu(II), N(I), N(II), O(I) and O(II) as well as some less intense lines from Ba(III), Y(III), Cu(III) and O(III) have been identified. It may be mentioned here that the light emission from the plume lasts for a few micro seconds.

## **7.2 Self-reversal and anomalous profile of Ba<sup>+</sup> resonance line in YBa<sub>2</sub>Cu<sub>3</sub>O<sub>7</sub> plume**

Laser ablated plasma from YBa<sub>2</sub>Cu<sub>3</sub>O<sub>7</sub> in air at atmospheric pressure has been studied and it was found that the spectral emission as well as the ionization mechanism vary with laser power density.<sup>7</sup> Interferometric measurements on the electron density show that it varies in the range  $10^{16}$ - $10^{17}$  cm<sup>-3</sup> depending on the laser power density.<sup>7</sup> The width of the resonance lines are found to be enhanced due to self absorption. Figures 7.3 to 7.5 show the optical emission spectra in the wavelength range 453.2-457.7 nm at laser power densities ranging from  $5.4 \times 10^{10}$  W cm<sup>-2</sup> to  $2.7 \times 10^{11}$  W cm<sup>-2</sup> at a distance ~ 0.5 mm from the target. These spectra were recorded with zero time delay after the laser pulse. The spectra show the emission profile of the resonant line from singly ionized barium at 455.403 nm corresponding to the transition  $6p^2P_{3/2} \rightarrow 6s^2S_{1/2}$ . The center of the line is self-reversed due to the absorption of radiation by the ions in the ground state. Figure 7.3 very clearly demonstrates the way in which the line shape develops with

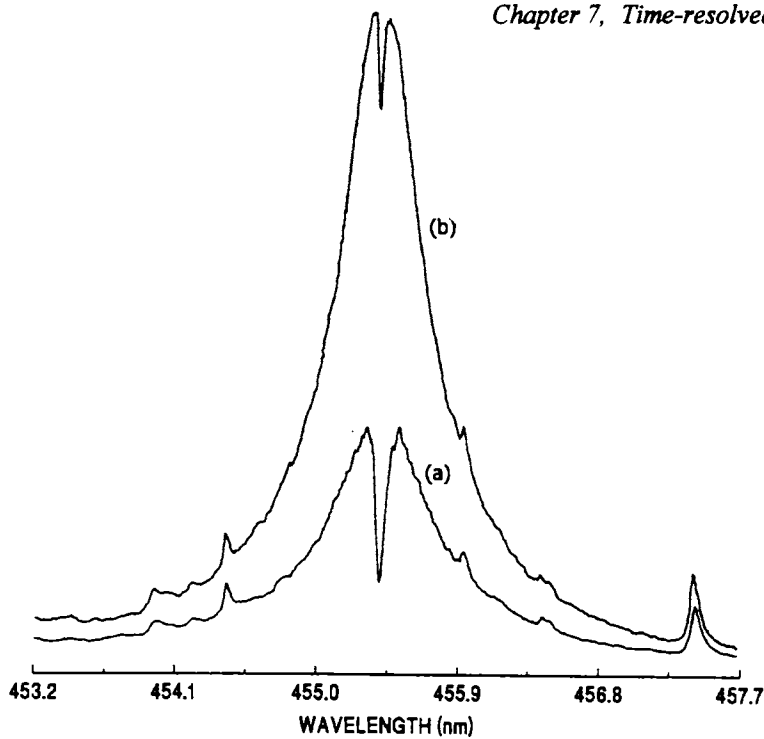


**Figure 7.3** The resonance broadened and self-reversed profile of the Ba II line of wavelength 455.403 nm at two laser power densities (a)  $5.4 \times 10^{10} \text{ W cm}^{-2}$  and (b)  $1.2 \times 10^{11} \text{ W cm}^{-2}$ . The radiation intensity at the center of the line increases as the laser power density is increased.

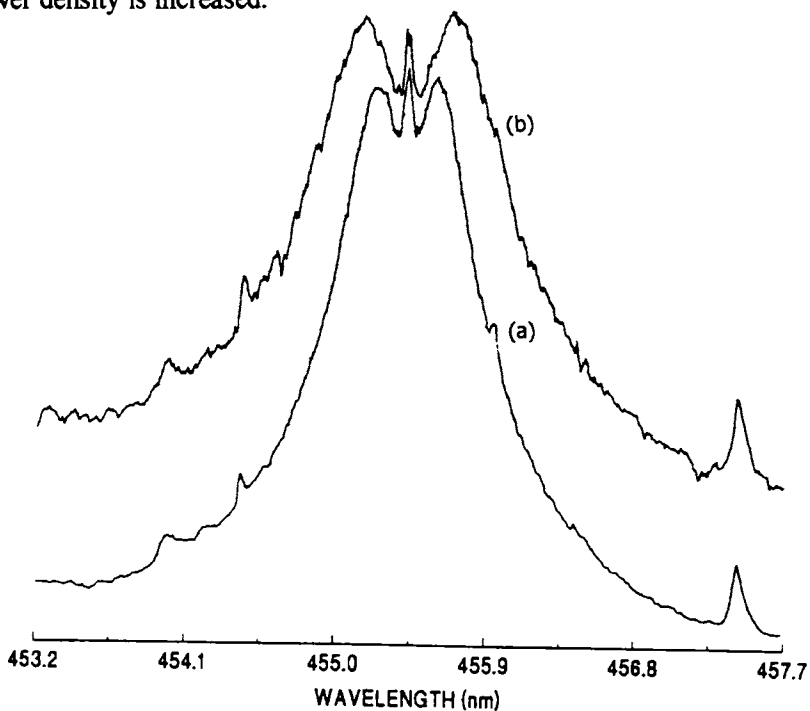


**Figure 7.4** The profile of the line at 455.403 nm at laser power densities (a)  $1.6 \times 10^{11} \text{ W cm}^{-2}$  and (b)  $2.4 \times 10^{11} \text{ W cm}^{-2}$ . A third peak at the center of the line is seen at these power densities.

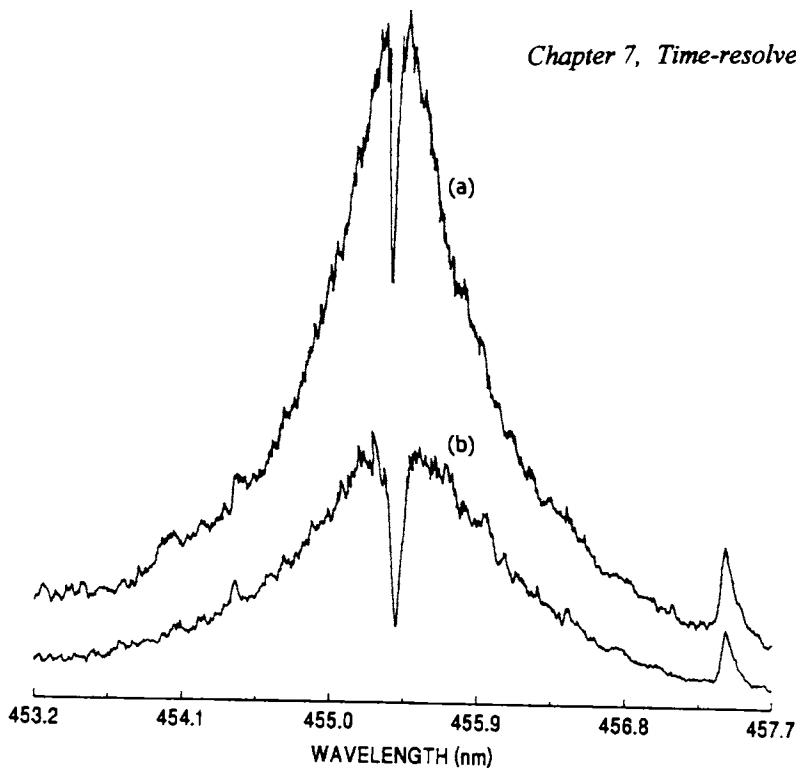


**Figure 7.5** The 455.403 nm line profile at laser power densities (a)  $2.6 \times 10^{11} \text{ W cm}^{-2}$  and (b)  $2.7 \times 10^{11} \text{ W cm}^{-2}$ . The profile is similar to that in Fig. 2. Here the plasma as a whole diffuses away from the target surface and the plasma length along the line of sight decreases.

respect to the power density. As the laser power density is increased, the intensity at the line center and the overall width of the spectral line are increased. When the laser power density reached about  $1.6 \times 10^{11} \text{ W cm}^{-2}$ , a central peak begins to develop exactly at the resonance frequency. Figure 7.4 shows the line profile at power densities  $1.6 \times 10^{11} \text{ W cm}^{-2}$  and  $2.4 \times 10^{11} \text{ W cm}^{-2}$ . At these power densities the line width increases as the laser power density increases but the peak intensity is reduced. That is, the photons from the peak of the line are redistributed into the wings. But when the power density reaches a value  $2.6 \times 10^{11} \text{ W cm}^{-2}$  the plasma as a whole drifts away from the target surface due to the collective diffusion thereby reducing the particle density as well as the plasma length near the target. Then the central peak vanishes and a self-reversed profile reappears. Figure 7.5 represents such a situation at  $2.6 \times 10^{11} \text{ W cm}^{-2}$  and at  $2.7 \times 10^{11} \text{ W cm}^{-2}$ . This happens because the plasma as a whole collectively drifts away from the target surface thereby reducing the length of the plasma at the observation point. This

phenomenon is characterized by a threshold power density and as the power density is increased still further the plasma drifts more and more away from the target and the intensity of emission goes on decreasing as shown in the figure. Under these circumstances the emission intensity maxima is shifted to a distance away from the target surface. Similar effects have been discussed in several other reports and this has been attributed to laser plasma interactions at high laser power densities.<sup>17</sup> In a dense plasma at atmospheric pressure (the one we describe here), the laser plasma interaction depth is limited to the skin depth in the plasma and electrons are heated up by inverse bremsstrahlung. The hot electrons escaping from the plasma can form a charged double layer at the plasma boundary and a part of the kinetic energy of the electrons is transferred to ions through electrostatic attraction.<sup>18,19</sup> This phenomenon is similar to the ambipolar diffusion in plasmas. Ambipolar diffusion is characterized by the collective nature and the diffusion coefficient and hence the velocity of the ions become twice that of the initial value.<sup>20</sup> This phenomenon is discussed in chapter 6 of this thesis.

### 7.2.1 Discussions on self-reversal of Ba<sup>+</sup> emission

Self-reversal of spectral line is said to occur when the radiation flux from the system is smaller at the line center than for the adjacent wavelengths at the wings of the line. The gas temperature inside the core is higher than that near its boundary and there exists a steep gradient in particle density as well as in temperature along the line of sight. For an optically thick plasma with spatially uniform absorption coefficient and assuming a Lorentzian line shape for the spectral line, the radiation flux at an angular frequency  $\omega$  is given by the equation,<sup>21</sup>

$$I_{\omega} = I_{\omega}^{(0)} \left( 1 - \frac{e^{-\tau}}{\tau} + \frac{a}{\tau} \right) \quad (7.3)$$



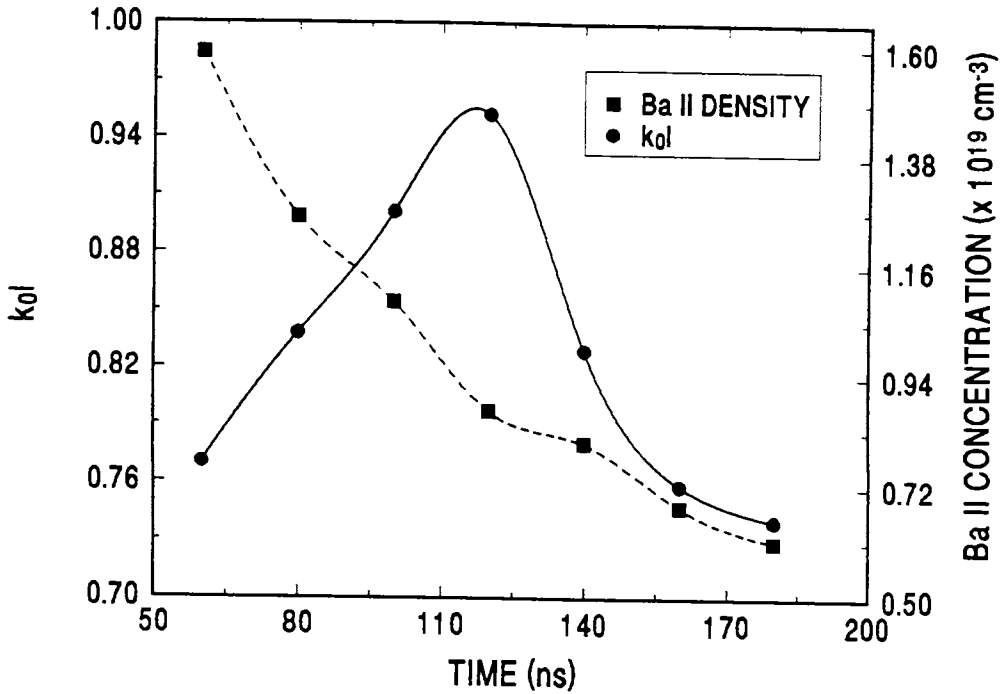


**Figure 7.6** Variation of the ion number density (■) as well as plasma absorption (●) as a function of time delay after the laser pulse. Number density is maximum at short time delays but plasma absorption peaks about 120 ns after the laser pulse. The data is taken at a laser power density of  $1.2 \times 10^{11} \text{ W cm}^{-2}$ .

where  $I_{\omega}^{(0)}$  is the blackbody radiation flux at the line center given by  $I_{\omega}^{(0)} = (\omega^2 / 4\pi^2 c^2) [\exp(\hbar\omega / kT) - 1]^{-1}$ ,  $\tau$  is the frequency dependent optical depth given by the relation  $\tau = k_0 l \nu^2 / [\nu^2 + (\omega_0 - \omega)^2]$ ,  $T$  (K) is the temperature of the ions,  $k_0$  ( $\text{cm}^{-1}$ ) is the absorption coefficient in the plasma,  $l$  (cm) is the length of the plasma,  $\nu$  (Hz) is the full width at half maximum of the emitted line  $\omega_0$  (Hz) is the resonance angular frequency and  $a$  is a temperature dependent quantity given by

$$a = \frac{2}{3} \frac{dT}{dx} l \frac{\hbar\omega}{T^2} (e^{\hbar\omega/T} - 1)^{-1} \quad (7.4)$$

If  $a \gg e^{-\tau_0}$ ,  $I_{\omega} \gg I_{\omega}^{(0)}$  (optically thick) and if  $a \ll e^{-\tau_0}$ ,  $I_{\omega} \ll I_{\omega}^{(0)}$  (optically thin). That is, when  $a \gg e^{-\tau_0}$ , the radiation flux in the vicinity of the line center increases while at the

center it is a minimum and the line is self-reversed. The maximum radiation intensity  $I_{\omega_1}$  corresponds to a frequency ( $\omega_1$ ) for which the optical thickness satisfies the condition  $(\tau + 1)e^{-\tau} = a$ . Therefore from eqn.(7.3),

$$I_{\omega_1} = I_{\omega}^{(0)}(1 + e^{\tau}) \quad (7.5)$$

From Eqn.(7.5) and using the expression for  $\tau$ , the value of  $k_0 l$  is estimated from the observed line profiles at various time delays after the laser pulse and its value is found to vary between 0.7 and 0.95 as shown in Figure 7.6.

The number densities of the species is directly proportional to the full width at half maximum of the resonant line through the relation<sup>10</sup>

$$\Delta \nu_{res} = \frac{c r_e}{8} k_{jj'} f_{res} \lambda_{res} N \quad (7.6)$$

where  $r_e$  (cm) is the classical electron radius,  $c$  (cm/sec) is the speed of light in vacuum,  $\lambda_{res}$  (cm) is the wavelength of the resonant transition,  $f_{res}$  the resonant oscillator strength,  $N$  ( $\text{cm}^{-3}$ ) the species number density and  $k_{jj'}$  is a constant determined by the ground and resonance levels. For noble gases<sup>10</sup> with  $j = 0$  and  $j' = 1$ ,  $k_{jj'} = 1.53$ . In order to estimate the plasma absorption and the ion number density, the profile of the line at 455.403 nm is recorded with a boxcar gate width 10 ns for different time delays after the laser pulse. Using Eqn. 7.6 and taking  $k_{jj'} = 1$ , the number density of Ba II is calculated at various time delays for a typical laser power density of  $6.2 \times 10^{10} \text{ W cm}^{-2}$ . Figure 7.6 shows the plot of  $k_0 l$  vs time delay as well as that between number density and time delay of the barium ions. The ion number density decreases very rapidly at shorter time delays as compared to the decay at later times. However, the value of  $k_0 l$  peaks at around 120 ns after the laser pulse. The low value of  $k_0 l$  at small time delays is expected since during that period the plasma is in a highly dense and ionized state with a large

number of collisions with the result that the majority of the ions are in the excited state. The small value of  $k_0 l$  at higher time delays is due to the decrease in the overall ion density in the plasma by electron-ion recombination. This outcome is clear from the low values of the ion number density shown in the figure.

### 7.2.2 Discussion on profile of Ba<sup>+</sup> resonance line at high laser intensities

In general, the radiative transfer of energy from the plasma depends on the effective absorption cross section of the transition, the spontaneous decay rate and the resonance scattering of radiation. Resonance scattering (fluorescence) can occur either with the frequency distribution of the scattered photons to be the same as that emitted spontaneously [*i.e.*, a Lorentzian function,  $L(\omega, x)$ ] or with a modified distribution characterized by a redistribution function. The frequency redistribution tries to enhance the intensity of the emitted light near the line center, contrary to the case when the scattered photons have the same frequency distribution as the absorption coefficient<sup>1</sup>. When the spontaneously emitted frequency distribution is not largely modified due to various interactions in the plasma, the ratio of the excitation rate ( $R_c$ ) to the effective radiative decay rate ( $R_r$ ) is given by<sup>1</sup>

$$\frac{R_r}{R_c} = 2.3 \times 10^{16} \frac{1}{N_e} \left( \frac{\hbar\omega}{E_H} \right)^3 \left( \frac{kT}{E_H} \right)^{1/2} \quad (7.7)$$

where  $N_e$  (cm<sup>-3</sup>) is the electron density,  $E_H$  (eV) the ionization potential of hydrogen,  $kT$  (eV) the temperature of ions in the plume and other symbols have usual meaning. Eqn.(7.7) shows that the ratio  $R_r/R_c$  is inversely proportional to the electron density in the plasma. In the present case, with  $N_e = 10^{16}$  cm<sup>-3</sup> and  $T \sim 13$  eV (corresponding to a velocity  $3.5 \times 10^5$  cm s<sup>-1</sup>),  $(R_r/R_c) = 0.036$ . For small values of  $R_r/R_c$  the ratio of the population of the upper level to that of the lower level is reduced from its local

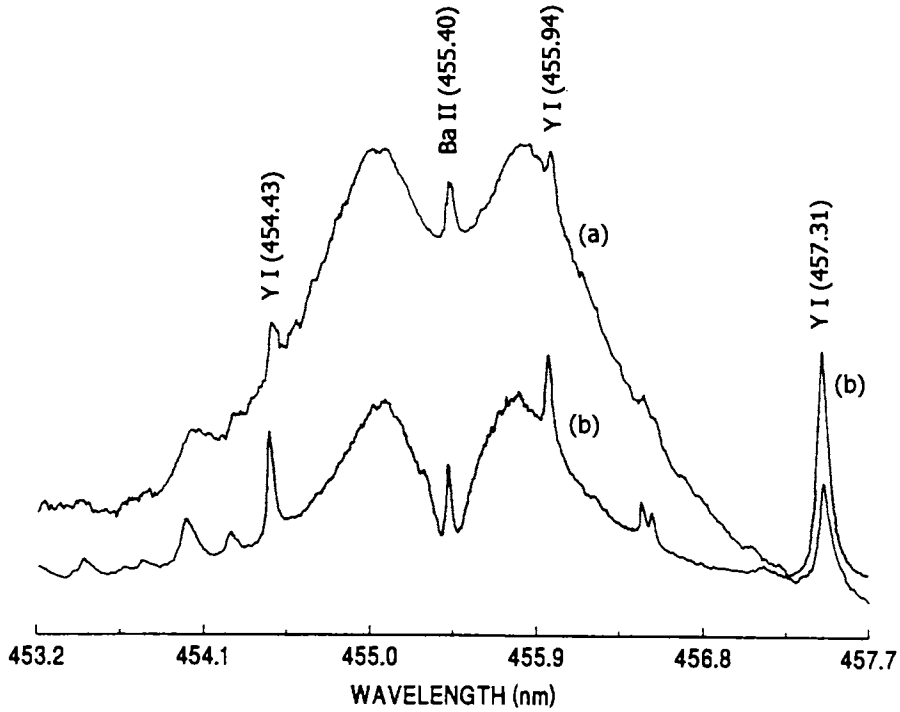


**Figure 7.7** Line profile at two different time delays after the laser pulse; (a) 30 ns (b) 700 ns at a laser irradiance of  $2.4 \times 10^{11} \text{ W cm}^{-2}$ . The width of the line is substantially reduced at longer time delays, but the central peak become more prominent.

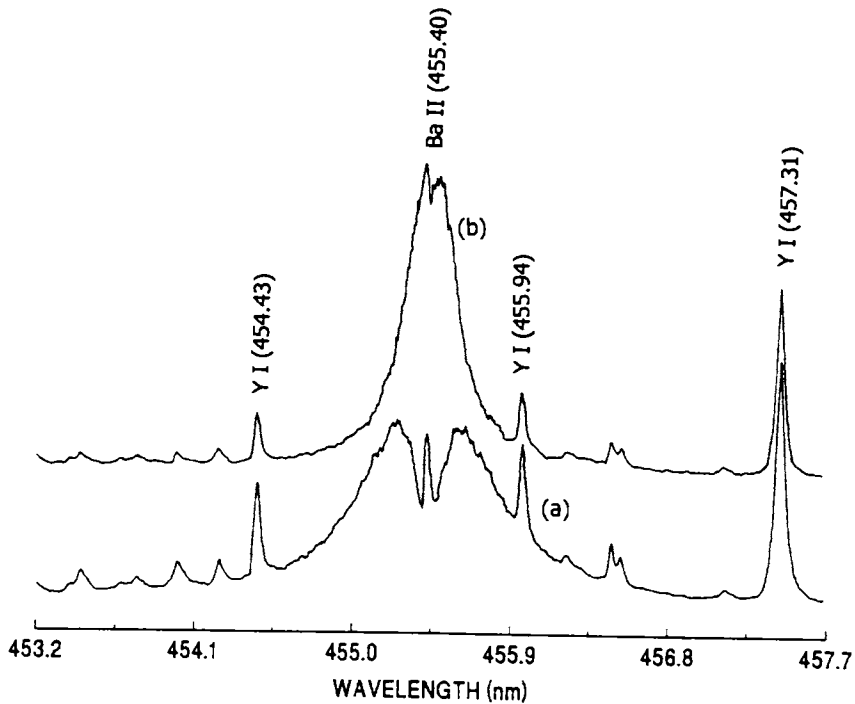


**Figure 7.8** Line profile at (a) 1.4  $\mu\text{s}$  and (b) 4  $\mu\text{s}$  after the laser pulse. The width of the line is reduced considerably and the peak at the center vanishes

thermodynamic equilibrium value by a factor  $1 - (R_r / R_c)$  near the line center frequency.<sup>1</sup> herefore, the intensity at the line center is less than that corresponding to frequencies away from the line center. This explains the self reversal of the lines shown in the Figures 7.3 and 7.5.

The observation of the central peak in the self-reversed line can be accounted for by the resonant scattering of photons by ions in the ground state with a frequency redistribution. When the scattered photons have a modified frequency distribution (because of anisotropic resonance scattering), different from that emitted by the ions, the situation is not similar to that described above. The outgoing photons do not have the same frequency distribution as the absorption coefficient and the shape of the line changes considerably. When the resonantly scattered photons have a modified frequency distribution different from that emitted by the ions, the line shape changes considerably. Then the emission intensity has to be averaged over all possible directions and the source function becomes<sup>1</sup>

$$S(\omega, \tau) \approx \frac{\hbar \omega^3 g_n N_m(\tau)}{4\pi^3 c^2 g_m N_n(\tau)} \left( 1 + \frac{1}{6} q \left( 1 - \frac{1}{\pi} \right) + \dots \right) \quad (7.8)$$

for  $\exp(\hbar\omega / kT) \gg 1$ . Here  $g_m$  and  $g_n$  are the statistical weights of the upper and lower levels and  $q$  the relative probability for resonance scattering. The above equation suggests that scattering tries to enhance the intensity of the resonance line. For frequencies slightly off the line center,  $\Theta = -\Theta$  ( $\Theta$  is the scattering angle) direction contributes significantly and the coefficient  $q$  in Eqn. (7.8) is smaller by a factor of  $(\pi-2)/(\pi-1) \sim 0.5$ . Therefore the intensity enhancement is prominent at the line center and this results in the third peak.

Figures 7.7 and 7.8 show the time dependence of the line profile of radiation from Ba II at 455.403 nm . The spectrum was recorded at a laser power density of  $2.4 \times 10^{11} \text{ W cm}^{-2}$  and averaged for about 4  $\mu\text{s}$ . The intensity of the third peak at the line center increases as the delay time is increased. Also the overall width of the line decreases as time goes on. The full width at half maximum of the third peak is a fraction of a nm (*viz.* 0.026 nm, 700 ns after the laser pulse) and is free from self-absorption broadening. After about 4  $\mu\text{s}$  the width of the entire line is reduced considerably and there is only a very small dip at the line center since the plasma is becoming optically thin. Some of the emission lines from Y I are also seen which are not so broad and intense and less susceptible to self absorption.

### 7.3 Summary

In this chapter, the time resolved analysis of optical emission from laser produced plasmas in air at atmospheric pressure has been carried out. During very small time delays, the spectrum consists of broad continuum whereas for larger time delays, atomic and ionic line emissions begin to appear. The sources of plasma continuum are bremsstrahlung radiation and radiative recombination. The emission lines are broadened with widths of several nanometers. The main broadening mechanism for resonance lines are self-absorption whereas for non-resonance lines the broadening is due to Stark effect.

The spectral profile of the intense, resonant line emission from  $\text{Ba}^+$  at 455.403 nm occurring in a laser produced plasma from  $\text{YBa}_2\text{Cu}_3\text{O}_7$  is also analyzed. This line is broadened by self-absorption with a full width at half maximum of several angstroms. The profile becomes self-reversed when sufficient ground state ions exist along the line of sight, because the line has a maximum absorption coefficient at the line center. Calculations on the Ba II density and the absorption along the line of sight show that the ion density is maximum during the initial stages of plasma evolution while the resonant absorption peaks after a time delay of about 120 ns. This shows that during the initial

stages of plasma evolution, most of the ions are in the excited state. The absorption peaks around 120 ns indicating the abundance of ground state ions at later times. Thereafter the decrease in the particle density inside the plume makes the plasma optically thin and the plasma absorption decreases. As the input laser power density is increased, the resonance scattering in the plasma becomes more anisotropic giving rise to a third peak at the center of the self-reversed line, whose width is only a fraction of a nanometer.

## References

- <sup>1</sup>H R Griem *Plasma Spectroscopy* (Mc Graw Hill New York, 1964)
- <sup>2</sup>G Bekefi (Ed.) *Principles of Laser Plasmas* (John Wiley & Sons, New York, 1976) p.597
- <sup>3</sup>F Blanco, B Botho and J Campose, *Physica Scripta* **52** (1995) 628.
- <sup>4</sup>W Pietsch, *J. Appl. Phys.* **79** (1996) 1250.
- <sup>5</sup>R Kelly, *Phys. Rev. A* **46** (1992) 860.
- <sup>6</sup>S S Harilal, Riju C Issac, C V Bindhu, Geetha K Varier, V P N Nampoore and C P G Vallabhan, *Pramana - J. of Phys.* **46** (1996) 145.
- <sup>7</sup>Geetha K Varier, Riju C Issac, S S Harilal, C V Bindhu, V P N Nampoore and C P G Vallabhan, *Spectrochimica Acta Part B* **52** (1997) 657
- <sup>8</sup>J M Vaughan, *Phys. Rev. A* **166** (1968) 13.
- <sup>9</sup>A R Malvern, J L Nicol and D N Stacey, *J. Phys. B* **7** (1974) L518.
- <sup>10</sup>J Cedolin, R K Hanson and M A Capelli, *Phys. Rev. A* **54** (1996) 335.
- <sup>11</sup>M R Winchester and R K Marcus, *Spectrochimica Acta Part B* **51** (1996) 839.
- <sup>12</sup>Y Leng, J Goldhar, H R Griem and R W Lee, *Phys. Rev. E* **52** (1995) 4328.
- <sup>13</sup>M Autin, A Briand, P Manchien and J M Mermet, *Spectrochimica Acta Part B* **48** (1993) 851.
- <sup>14</sup>D B Chrisey and G K Hubler, (Eds.) *Pulsed laser deposition of thin films* (John Wiley & Sons Inc., New York, 1994)
- <sup>15</sup>J F Kielkopf, *Phys. Rev. E* **52** (1995) 2013.

<sup>16</sup>Rajiv K Singh and J Narayan, *Phys. Rev. B* **41** (1990) 8843.

<sup>17</sup>Dieter Baurle *Laser Processing and Chemistry*, (Springer 1996) p.184

<sup>18</sup>S Eliezer and H Hora, *Phys. Reports* **172** (1989) 339

<sup>19</sup>E G Gamaly, *Laser and Particle Beams* **12** (1994) 185.

<sup>20</sup>E M Lifshitz and L P Pitaevskii *Physical Kinetics*, (Pergamon, 1981) p. 108.

<sup>21</sup>B M Smirnov *Physics of weakly ionized plasmas*, (Mir Publishers, Moscow, 1981)



# Summary and Conclusions

The overwhelming interest in the field of high power laser interaction with solids compelled many researchers around the world to take up detailed the studies of such processes. The study of laser matter interaction has assumed many new dimensions among which the phenomena of laser ablation has a major role both in fundamental studies and in technological applications. The various electronic and photonic phenomena that occur during intense field interactions with solids are extremely complex. So it is highly difficult to integrate each and every aspect of these interactions into a single theoretical framework. Most often the finer aspects of laser ablation can be worked out in detail only with proper experimental support. The explosive laser matter interaction such as laser ablation has to be generally described under different headlines such as laser absorption, energy transfer to the lattice, plasma formation and evolution, gas phase collisions, deposition of the ablative products on to suitable substrates etc. A large amount of careful experimentation is required for a realistic understanding of the laser generated plasma as a whole.

As a part of the world wide efforts on the unraveling of the complexity of the laser ablation process, in India, a few laboratories are involved in the generation and characterization of laser produced plasmas. The major among them are Center for Advanced Technology Indore, Tata Institute of Fundamental Research Mumbai, Indian Institute of Technology Kanpur and Cochin University of Science & Technology (CUSAT). At the laser laboratory of CUSAT, we have been making modest attempts to decipher the various processes in the plasma generated by nanosecond laser pulses incident on solids. These studies include cluster formation, electron heating, charged double layer formation, boundary effects, shock wave generation, evolution of electrons

atoms and ions and gas dynamics. Emission spectroscopy, Langmuir probes and interferometry are usually used as the plasma diagnostic tools in studying these processes. The preceding chapters of this thesis give the results of some of the laser ablation experiments carried out by the author during the past four years at CUSAT.

The thesis deals with the various processes that occur during the interaction of the high power nanosecond laser with solid targets like silver and superconducting Yttrium Barium Copper Oxide ( $\text{YBa}_2\text{Cu}_3\text{O}_7$ ). The experiments on silver were done under vacuum conditions and  $\text{YBa}_2\text{Cu}_3\text{O}_7$  has been examined under atmospheric pressure conditions. All the aspects observed during these studies are not dealt with in detail, but the only processes which appear to be interesting and novel only are included in this thesis.

### **8.1 Laser generated plasma from silver targets**

Laser produced plasma from silver is obtained by focusing the 1064 nm radiation from a Q-switched Nd:YAG laser onto silver targets. The dynamics of atoms, ions and electrons were analyzed separately. Electrons are the primary objects which directly absorb the laser radiation in metallic solids. Even in nonmetallic solids, there are a number of free electrons at a finite temperature which can absorb the laser radiation and seed the ablation process. The electrons usually come to a state of thermal equilibrium due to collisions. The absorbed energy is transferred to the lattice within picoseconds leading to the heating of the lattice to a temperature which is very close to the thermodynamic critical temperature thereby causing phase explosion and ablation. But a fraction of electrons may be escaped from the focal volume before the energy is being transferred to the lattice through electron-phonon interactions. We have observed a very narrow pulse of electrons in the temporal profile (observed using positively biased Langmuir probes) which appears very early in time with pulse duration close to that of the laser pulse. These are obviously photoelectrons, but not the conventional ones which obeys the Einstein photoelectric equation. These are the electrons which escape from the focal volume during electron

heating with the laser pulse. We have also shown that these electrons cause collisional excitation and ionization of ambient molecules and atoms within the plasma chamber. With proper electron collimating and focusing optics, these electron pulses can be made into a beam with nanosecond pulse duration which can be used for several electron collision experiments. We hope that with picosecond laser beams, these electron pulse widths can be further reduced leading to ultrashort electron pulses, the realization of which needs further experiments using picosecond lasers.

Silver atom has good emissions in the visible regions where the present experimental setup has fairly good sensitivity. Therefore optical emission spectroscopy is utilized for the study of the dynamics of atomic species. Mostly, the time of flight profiles of atoms are analyzed as a function of distance from the target and pressure inside the chamber. The pressure is varied from  $2 \times 10^{-5}$  mbar to 0.5 mbar. An anomalous twin peak distribution in the time of flight profile is observed at low pressure. A collection of slower species emerge at reduced pressure below  $4 \times 10^{-3}$  mbar and these species has a velocity spread which is greater than that at higher pressures. This phenomenon is shown to be the result of gas phase collisions and the formation of the so-called *Knudsen layer* within a few mean free paths from the target. The *half range* Maxwellian distribution is changed over to a *full range* Maxwellian velocity distribution at the *Knudsen layer* boundary. A collection of backward moving particles emerge at the *Knudsen layer* which will either be recondensed or reflected from the target. The slower species are those reflected from the target surface. At high pressure, the plasma expansion follows the shock wave model with cylindrical symmetry whereas at reduced pressure it follows unsteady adiabatic expansion. During unsteady adiabatic expansion, the species show a parabolic increase in expansion time with radial distance whereas during shock wave expansion, the exponent is less than one. Thus optical emission spectroscopy is effectively utilized for the study of the dynamics of the atoms in laser generated silver plasma.

Since positive ions do not emit substantially in the visible region, the ion dynamics has to be studied using Langmuir probes instead of optical emission spectroscopy. We have carried out space resolved measurements on the positive ions which shows that there exists clear boundary between the plasma and the ambient gas. There exists an ion density steepening at the plasma boundary which is characteristic of the charged double layer formation. Also, the ions gain much more energy at the boundary showing an increase in velocity of ions. That is, at the boundary the ions gain energy from the electrons which moves ahead of the ions. Hence our observations on the dynamics of electrons, ions and atoms reveal much more information regarding laser-matter interaction processes and plasma dynamics. Especially these studies shed more light into the electron temporal profiles, gas phase collisional effects and on the processes which occur at the boundary of the plasma.

## **8.2 Laser produced plasma from $\text{YBa}_2\text{Cu}_3\text{O}_7$**

Laser ablated plasma from the superconducting  $\text{YBa}_2\text{Cu}_3\text{O}_7$  is analyzed at atmospheric pressure. In these experiments also, the main aim was to study the basic nature of laser matter interaction process.  $\text{YBa}_2\text{Cu}_3\text{O}_7$  pellets have higher absorptivity than silver and the ablation rates and hence plasma density are larger in the case of  $\text{YBa}_2\text{Cu}_3\text{O}_7$ . Also at atmospheric pressure, the plasma is confined to very small volumes compared to that in vacuum and therefore the density is higher than that in the case of vacuum. At those higher densities we observe interesting processes such as collective drift due to ambipolar fields and modified line shapes for resonance lines. In addition to that, the various ionization mechanisms of the constituents of the plasma also are analyzed. Another interesting aspect that has been studied is the time resolved emission spectrum from the plasma. During initial time intervals (within  $\sim 50$  ns), the spectrum is dominated by plasma continuum and only after larger time delays ( $>100$  ns) the ionic and atomic emission occur which in turn is due to electronic transitions as a result of plasma cooling. Thus our observations on laser ablated plasma from  $\text{YBa}_2\text{Cu}_3\text{O}_7$  reveal the various

ionization, emission and diffusion processes that take place in laser produced plasmas of high density and temperature.

A very interesting observation that was made during these measurements is the peculiar line shape of the self-reversed resonance lines of  $\text{Ba}^+$  at 455.4 nm. At higher laser power density there originates a peak at the line center of the self-reversed resonance line. This has been explained as due to anisotropic resonance scattering of radiation.

### **8.3 Future trends**

The nanosecond laser produced plasmas have been widely used for the deposition of high quality thin films especially that of high  $T_c$  superconducting materials which require reactive environments for stoichiometric deposition. Apart from the film deposition laser ablation has been widely used for elemental analysis, measurement of spectroscopic constants such as transition probabilities, in laser induced breakdown spectroscopy, for the construction of plasma recombination laser etc. The power densities that can be attained using nanosecond laser pulses is upto  $10^{12} \text{ Wcm}^{-2}$  and beyond that one should use pico or femtosecond laser pulses. Power densities as high as  $10^{17} - 10^{18} \text{ Wcm}^{-2}$  are obtained with powerful femtosecond laser pulses. At the National Ignition Facility at Lawrence Livermore National Laboratory, the maximum power density attained is of the order of  $10^{21} \text{ Wcm}^{-2}$  by using which scientist expect to perturb the nucleus of light elements leading to inertial confinement fusion. At such high intensities, the idea of photons give way to the concept of intense electric fields and the phenomena are explained in terms of classical electric field associated with the laser beam. Therefore, the ultimate aim is to attain electric fields that are comparable to nuclear fields so that nuclear fusion is achieved leading to the production of useful energy. The plasma generated using the currently available pico and femto second laser pulses produce considerable gain in the X-ray region which can lead to the fabrication of table top X-ray lasers.